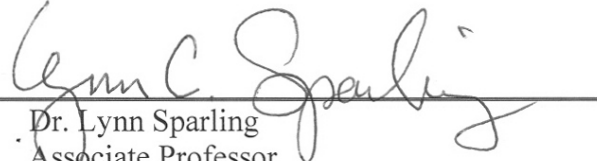


APPROVAL SHEET

Title of Thesis: Multi-Scale Analysis of Observations of Tropical Cyclones with
Applications to High-Resolution Hurricane Modeling

Name of Candidate: Samuel Gerard Trahan
Doctor of Philosophy in Atmospheric Physics, 2011

Thesis and Abstract Approved:

A handwritten signature in black ink, reading "Lynn C. Sparling", is written over a horizontal line.

Dr. Lynn Sparling
Associate Professor
UMBC Physics Department

Date Approved: August 4, 2011

Curriculum Vitae

Academic Degrees

2003 BS in Computer Science, University of Maryland, Baltimore County (UMBC)

2005 MS in Applied Physics, UMBC

2007 MS in Atmospheric Physics, UMBC

2011 Ph.D. in Atmospheric Physics, UMBC

Employment History

1998–2004 Research Assistant at the *National Institute of Standards and Technology*
(NIST)

Evaluated the skill of various commercial and governmental face, gait and fingerprint recognition algorithms. Improved algorithm skill through matrix renormalization techniques, created a lossless gait video compression algorithm and developed various efficient mass data processing techniques.

2003–2009 Research Assistant *UMBC*

Research and teaching assistant for upper-level classical and quantum mechanics courses. Created a trajectory model to determine the source and destination of passive tracers, ported and ran WRF and HWRF on various clusters. Installed and maintained unix server and desktop machines. Was awarded the Goddard Earth Sciences and Technology Fellowship. Worked with UMBC to create its first campus-wide scientific computing cluster.

2009–Present *University Corporation for Atmospheric Research* (UCAR) Visiting
Scientist at the *Environmental Modeling Center* (EMC)

Worked on hurricane model development, forecast validation and automation of various mass data processing tasks. Developed a high-resolution version of the HWRF hurricane forecasting model. Created the HHS automation suite, now used by EMC to automate tests of thousands of HWRF simulations per year.

Publications and Grants

Bao, S., et al., 2010: The community hurricane weather research and forecast (HWRF): System description, forecast skill and developmental testbed center support. *29th Conference on Hurricanes and Tropical Meteorology*.

Sparling, L. and S. Trahan, 2008: Impact of small-scale inner core dynamics on tropical cyclone intensity. National Science Foundation, Teragrid allocation (super-computer access grant) TG-ATM080003N.

Trahan, S., , L. C. Sparling, V. Tallapragada, S. A. Braun, and J. Halverson, 2010a: Statistical comparison of scales and spatial distributions of convection in observational data and simulated hurricanes. *29th Conference on Hurricanes and Tropical Meteorology*.

Trahan, S. and L. Sparling, 2011: An analysis of NCEP tropical cyclone vitals and potential effects on forecasting models, in review, accepted with minor changes, *Weather and Forecasting*.

Trahan, S., L. Sparling, and J. Halverson, 2008: Scale analysis of spatial variability in observations of tropical cyclones. *28th Conference on Hurricanes and Tropical Meteorology*.

Trahan, S., V. Tallapragada, Z. Zhang, J. Oconnor, L. C. Sparling, and B. Lapenta, 2010b: A high resolution version of operational hwrf: forecast ability and computational challenges presented by an operational environment. *29th Conference on Hurricanes and Tropical Meteorology*.

Yang, K., et al., 2010: Direct retrieval of sulfur dioxide amount and altitude from spaceborne hyperspectral UV measurements: theory and application. *Journal of Geophysical Research*, **115**.

Coursework

Physics and Atmospheric	Computational
Electromagnetic Waves and Radiation	<i>Graduate Level:</i>
Statistical Mechanics	Computer Graphics
Computational Physics	Advanced Operating Systems
Quantum Mechanics II	Advanced Computer Architecture
Mathematical Physics	Quantum Computation
Classical Mechanics	<i>Undergraduate:</i>
Advanced Electromagnetic Theory	Database Management Systems
Atmospheric Dynamics	Data and Network Security
Atmospheric Radiation	Compiler Design Principles
Atmospheric Physics I & II	Computer Algorithms
Computational Fluid Dynamics	Computer Architecture
Data Assimilation	Automata Theory and Formal Lan-
	guages
(Plus 38 credits of undergraduate	(Plus 21 credits of additional CS
physics.)	coursework.)

ABSTRACT

Title of dissertation: MULTI-SCALE ANALYSIS OF
OBSERVATIONS OF TROPICAL
CYCLONES WITH APPLICATIONS
TO HIGH-RESOLUTION
HURRICANE MODELING

Samuel G Trahan, Doctor of Philosophy, 2011

Dissertation directed by: Dr. Lynn Sparling
Department of Physics

Tropical cyclone numerical models, a critical tool to forecasters, have been run at resolutions of around 9–30 km in operational centers until recently. It is currently possible to run in the range of 1–4 km resolution, which may allow a model to resolve small-scale dynamical processes critical to tropical cyclone intensity. A 3km version of the NCEP HWRF model is developed for that purpose and its competitive track and intensity forecasting abilities are demonstrated.

To determine if the small scales are resolved correctly, a statistical framework for comparison to observations of small-scales is developed. The standard definition of a model's forecast intensity is examined, and found to have a systematic, resolution-dependent bias. A database of TRMM overpasses of over eight hundred tropical cyclones is produced and used to show a relationship between storm-scale cloud top temperature and storm wind intensity. However, all storms, regardless of strength, produce near-tropopause cloud tops, and storms undergoing rapid inten-

sification (RI) tend to have higher cloud tops than non-RI storms. In an analysis of in-situ wind data, vertical wind is shown to be scale-invariant, with no correlation beyond, nominally, 2 km scales.

This new framework for comparison is used to show that model's cloud tops have the right relationships with intensity and intensification, but that downdrafts are weak and rare. Model "spin-up" issues are seen: in the first six hours, some storms rapidly gain fine-scale 3 km resolution wind maxima that hurt the forecast and others weaken uniformly at all resolutions. In addition, a model bug is found in this and operational HWRF: all microphysics type fractions are discarded when the nest moves.

Overall, the research presented in this demonstrates the value of statistical diagnostics for high-resolution models. In addition, this research presents a framework for a deeper investigation of tropical cyclone small-scale dynamics.

Multi-Scale Analysis of Observations of
Tropical Cyclones with Applications to
High-Resolution Hurricane Modeling

by

Samuel Gerard Trahan

Dissertation submitted to the Faculty of the Graduate School of the
University of Maryland Baltimore County in partial fulfillment
of the requirements for the degree of
Doctor of Philosophy
2011

Advisory Committee:
Professor Lynn Sparling, Chair
Professor Kevin McCann
Professor Jeffrey Halverson
Dr. Scott Braun
Dr. Vijay Tallapragada

© Copyright by
Samuel G Trahan
2011

Acknowledgments

Completion of this doctoral degree has been a long and difficult journey for me due to hardships outside of graduate school. Without the help and support of my friends and family, I likely would not have made it to this day. To them, I owe my eternal gratitude.

I would also like to thank the National Science Foundation Teragrid Project, Goddard Earth Sciences and Technology Center, University of Maryland Baltimore County and National Oceanic and Atmospheric Administration for funding and computational resources to support this research.

Last, but not least, I would like to thank my thesis adviser Lynn Sparling for her help and advice, and especially for her near-infinite patience. No matter how many mistakes I make, no matter how stupid I prove to be, and no matter how many times I flood the physics building, she has been there to support me.

Table of Contents

List of Tables	vii
List of Figures	viii
List of Abbreviations	xiii
1 Introduction	1
1.1 Organization of this Thesis	4
2 The Anatomy of a Tropical Cyclone	7
2.1 Tropical Cyclones: The Basics	7
2.2 The Environmental Flow	10
2.3 Moisture: The Sea, Wake and Rainbands	14
2.4 Terrain Effects	18
2.5 Inner-Core Structure	21
2.6 Additional Effects	26
2.7 Superintense Storms and Rapid Intensification	28
2.8 Summary and Approach to Model Diagnostics	32
3 Scale Analysis of Near-Convective Scale Dynamical Processes	34
3.1 Scale invariance and universality	36
3.2 Statistical concepts and methodology	39
3.2.1 Challenges in the application of statistical methods to obser- vations of Tropical Cyclones	39
3.2.2 One point and two-point statistics	41
3.2.2.1 Increments	42
3.2.2.2 Structure Function	43
3.2.3 Advantages of Two-Point Statistics	44
3.2.4 Structure Function and Autocorrelation	47
3.2.5 Correlation Length	49
3.3 NOAA WP-3D Orion In-Situ Data	50
3.4 Structure Functions	52
3.4.1 Vertical Wind Structure Function	56
3.4.2 Horizontal Wind Results	62
3.4.3 Saturated Regions	64
3.4.4 Unsaturated Regions	68
3.4.5 Other Conditioning	70
3.5 Structure Function Slopes	71
3.6 Vertical Wind PDF and Normalized Increment PDF	73
3.7 Volumetric Vertical Flux	80
3.8 Conclusions	83

4	Wind Bias in the Utopian Model	86
4.1	Background	87
4.2	Methodology	92
4.3	Results and Discussion	94
4.4	Conclusions	97
5	TRMM Satellite Overpass Database	99
5.1	TRMM Instruments	101
5.2	TRMM Data Examples	103
5.3	Finding TRMM Tropical Cyclone Overpasses	106
5.3.1	NOAA and JTWC Best Track Databases	107
5.3.2	TRMM Ephemeris Data	109
5.3.3	Finding TRMM Crossovers	110
5.4	A First Look at the Database: Discussion	112
5.5	Conclusions	116
6	TRMM Statistical Analysis	117
6.1	Methodology	118
6.2	Results	120
6.3	Discussion	125
7	High-Resolution HWRF: Design, Rationale and Bugs	129
7.1	Designing a High-Resolution Hurricane Model	130
7.2	High-Resolution HWRF	134
7.3	High Resolution HWRF Forecasting Ability	136
7.4	Ice-Water Forgetfulness Bug	142
7.5	Fixing the Bug	146
7.6	Conclusions	146
8	Model Diagnostics: In-Situ Data	148
8.1	Simulated Aircraft Measurements	150
8.1.1	Vertical Wind PDF	152
8.1.2	Structure Functions	155
8.1.2.1	Vertical Wind Structure Function	155
8.1.2.2	Tangential Wind Structure Function	157
8.1.2.3	Radial Wind Structure Function	159
8.2	Maximum Wind Dropoff with Resolution	161
8.3	Possible Reasons for Missing Downdrafts	169
8.4	Conclusions	171
9	Model Diagnostics: Cloud Tops	173
9.1	Cloud Top Definition	174
9.2	Cloud Tops: Bulk Outflow and Intensity	175
9.3	Cloud Tops: Peak Convection and Intensity	178
9.4	Cloud Tops: Rapid Intensification	178

9.5	Results and Discussion	180
10	Conclusions and Future Work	183
10.1	Summary and Conclusions	183
10.2	Future Directions	187
A	Numerical Prediction of Hurricanes	189
A.1	The Global Forecasting System	190
A.2	Hurricane Weather Research and Forecasting System	192
A.2.1	HWRF Framework	195
A.2.2	HWRF Dynamical Core	196
A.2.2.1	WRF-NMM Solver	198
A.2.2.2	Non-Hydrostatic Solver	199
A.2.3	HWRF Parameterizations	208
A.2.3.1	Microphysics: Ferrier Scheme	208
A.2.3.2	Convection: Simplified Arakawa Schubert	209
A.2.3.3	Surface Layer: Modified GFDL Surface Layer	210
A.2.3.4	Turbulent Mixing: GFS Planetary Boundary Layer Scheme	211
A.2.3.5	Radiation Schemes	212
A.2.3.6	Land Surface Model: GFDL Slab Model	212
A.3	Initialization: GSI, Vortex Relocation and Bogussing	213
B	Observation of Tropical Cyclones	215
B.1	TRMM VIRS Imager	215
B.2	Radar Reflectivity Factor and dbZ	216
B.3	Breakdown of Z Assumptions	219
B.4	Specific Radars Used	221
C	Adventures in High-Resolution Modeling	223
C.1	HHS: A Test Suite	223
C.2	New Built-In Model Vortex Tracker	225
C.3	Initialization: Vortex Relocation with Three Domains	227
C.4	Track and Intensity Information	228

List of Tables

7.1	Description of models shown in figures 7.2, 7.3 and 7.4	138
-----	---	-----

List of Figures

2.1	Hurricane Fay (2008) on August 22 at 11:10 UTC, heading northwest towards a hyperbolic point in the flow created by several high and low pressure systems.	11
2.2	The Galveston Hurricane of 1900. Left: surface pressure field analysis courtesy of NOAA, showing the hurricane making landfall. Right: wreckage of broken houses washed out to sea by the storm surge. . . .	17
2.3	Hurricane Mitch (1998). Top left: satellite image of Mitch near its peak intensity as a Category 5 Hurricane. Top right: track of Hurricane Mitch. Bottom: mudslides on the Casita Volcano. Images courtesy of NOAA.	20
2.4	Hurricane Isabel (2003) eye and eyewall, as seen from the International Space Station. In the bottom right, convection is seen detraining, and generating gravity waves. Inside the eye, several mesovortices are seen. Near the back in the eye, a hot tower is present. Thin cirrus clouds cover portions of the eye. Spiral clouds are seen climbing up the eyewall to the right.	22
3.1	Structure functions of all data from all radial passes on a log-log plot.	53
3.2	Structure functions of all data from all radial passes on a linear plot.	55
3.3	Structure functions of vertical wind for all radial passes in Hurricane Ivan (2004) at left, and Bonnie (1998) at right.	56
3.4	Example line fits to vertical wind structure functions.	58
3.5	Top (3.5a): transition scales from vertical wind structure functions, obtained using the described double line fitting routine. Bottom (3.5b): correlation length, calculated from the power law exponent and transition scale, as derived in Section 3.2.5. Numbers in parentheses are the number of samples.	59
3.6	Top left (3.6a): PDF of vertical wind correlation length, conditioned on pressure; top right (3.6b): on storm wind intensity; bottom left: on intensification of 30 knots within 24 hrs or less (3.6c); bottom right (3.6d): on intensification of 30 knots within 36 hrs or less. In parentheses are the number of samples.	61
3.7	Structure functions of radial wind in saturated regions for all radial passes in Hurricane Ivan (2004) and Bonnie (1998).	64

3.8	Correlation lengths derived from vertical wind and radial wind structure functions, obtained using the previously described double line fitting method and correction factor to the transition scale.	65
3.9	Structure functions of tangential wind in saturated regions for all radial passes in Hurricane Ivan (2004) at left and Bonnie (1998) at right.	67
3.10	Top left and right: structure functions of radial wind in unsaturated regions of Ivan (2004) and Bonnie (1998). Bottom left and right: structure functions of tangential wind in unsaturated regions of Ivan (2004) and Bonnie (1998).	69
3.11	PDF of the slopes of radial wind structure functions, with and without conditioning on saturation, and with various (or no) detrending. . . .	72
3.12	Example PDFs of vertical wind values from several storms and a model. Colored PDFs are observations and black is the model.	73
3.13	Example normalized increment PDFs. Left (3.13a): one with a Gaussian-like core and Weibull-like distribution in the tails. Right (3.13b): one that is Gaussian-like throughout. Note the logarithmic Y axes. . . .	77
3.14	Example of a Weibull fit. Left (3.14a): a “Weibull plot”, where axes are chosen such that a Weibull distribution will be linear on that plot. Right (3.14b): the resulting fit to a CDF.	78
3.15	Weibull k exponents for normalized w increment PDFs from two different conditionings (saturated and unsaturated) and for the positive and negative half of the PDF.	79
3.16	Top left (3.16a): histogram of upward volumetric flux concentration in fourteen North Atlantic tropical cyclones. Top right (3.16b): downward flux. Bottom (3.16c): upward flux conditioned on pressure: circles are $P < 700mbar$ and plusses are $P > 700mbar$	82
4.1	The Utopian Forecasting Model is a model that produces a perfect forecast 100% of the time, represented in a finite element or finite difference grid, or in a spectral model. An inherent averaging and subsampling (or spectral truncation) is inherent in that, leading to a drop in maxima.	88
4.2	Diagram of P3 sampling used to emulate the Utopian Model.	92
4.3	Dropoff of the maximum wind of various resolution Utopian Models as compared to the “truth” wind speed from a 300 m averaging. . . .	95

4.4	Percent dropoff of the maximum wind predicted by Utopian Models of various resolutions, for a storm of “truth” maximum wind of 85 knots.	96
5.1	Hurricane Bonnie (1998) satellite images from GOES-8, TRMM-VIRS and TRMM-PR with circles plotted at 1 and 2 RMW. Top (a): VIRS 10.8 μm channel and GOES-8 10.8 μm channel. Bottom left (b): TRMM 18dbZ echo top height and NOAA P3 Orion in-situ wind measurements (red airplane shows the P3 location during TRMM overpass). Bottom right (c): TRMM 2.5km radar reflectivity (dbZ) with the same P3 wind.	105
5.2	TRMM PR 18 dbZ echo top height from Typhoon Usagi (2007) on July 30, 2007 at 17:33:12 UTC. The X marks are 6 hourly JTWC Best Track storm center positions and the square is those positions interpolated to the time of overpass. The circle is the JTWC 2 RMW circle.	114
5.3	TRMM VIRS channel 4, 10.8 μm brightness temperatures from Typhoon Usagi (2007) on July 30, 2007 at 17:33:12 UTC. The X marks are 6 hourly JTWC Best Track storm center positions and the square is those positions interpolated to the time of overpass. The circle is the JTWC 2 RMW circle.	115
6.1	PDF of median TRMM VIRS 10.8 μm channel brightness temperature and 18dbZ echo top height, conditioned on tropical storm intensity. Intensity categories are the Saffir-Simpson scale.	121
6.2	PDF of 1st percentile TRMM VIRS 10.8 μm channel brightness temperature and 99th percentile TRMM PR 18dbZ echo top height, conditioned on tropical storm intensity. Intensity categories are the Saffir-Simpson scale.	122
6.3	PDF of 1st percentile TRMM VIRS 10.8 μm channel brightness temperature and 99th percentile TRMM PR 18 dbZ echo top height, conditioned on RI vs. non-RI cases.	124
6.4	Example TRMM precipitation radar cross-section. Note that the reflectivity tops are cut off at 18 dbZ.	125
6.5	Example ER-2 EDOP radar cross-section. Note that the reflectivities for higher convection go far beyond 18 dbZ.	126

6.6	Example CloudSat radar cross-section. Note that the reflectivities for higher convection go far beyond 18 dbZ. Gaps at mid- and low-levels are because reflectivities with values greater than around 20 dbZ are not visible to CloudSat due to its different frequency.	127
7.1	Radius of Outermost Closed Isobar (ROCI) and Radius of Maximum Wind (RWM) from a large number of tropical cyclones worldwide, taken from the real-time TCVitals database.	132
7.2	Wind intensity error: mean absolute difference between model predicted gridscale 10 meter wind and observed one minute sustained ten meter wind over a large number of simulations. See Table 7.1 for a larger legend.	137
7.3	Wind intensity bias: mean difference between model predicted grid-scale 10 meter wind and observed one minute sustained ten meter wind over a large number of simulations. See Table 7.1 for a larger legend.	139
7.4	Track error: mean distance between model predicted storm center location and observed storm center location, averaged over a large number of simulations. See table 7.1 for a larger legend.	140
7.5	Ferrier Scheme ice fraction (fraction of condensate in ice form). Top left: 3 minutes before the nest moves. Top right: at the time of nest move. Notice that all ice fraction has been set to 0, indicating rain. Rain fraction and riming factor (not shown) have been modified to change the rain to small cloud droplets. Bottom left: small cloud droplets start to freeze. Bottom right: a half hour after nest moves, the atmosphere has recovered.	145
8.1	Diagram of the “fake P3 campaign” whereby model data is linearly interpolated in space and time to the location of an imaginary P3 flying through the moving storm.	151
8.2	Distribution of vertical wind in four storms (colored) and two high-resolution HWRF simulations (black). Crosses are data from a Karl (2010) simulation with the microphysics bug discussed in Chapter 6, and circles are data from a Karl (2010) simulation with the bug corrected.	153
8.3	Structure functions of vertical wind in saturated regions in two Karl simulations and in all observed storms combined.	156

8.4	Structure functions of tangential wind in two Karl simulations, in observed Karl and in all observed storms combined. Left (8.4a): log-log plot, right (8.4b): linear plot.	158
8.5	Structure functions of radial wind in two Karl simulations. Left (8.5a): saturated regions, on a log-log plot. Right (8.5b): all regions, on a linear plot.	160
8.6	Top: fractional dropoff of the 9 km resolution wind maximum relative to the 3 km maximum, as a function of the 3 km maximum, at the analysis time. Bottom: same, but for the 6 hr forecast.	165
8.7	Top: fractional dropoff of the 27 km resolution wind maximum relative to the 3 km maximum, as a function of the 3 km maximum at the analysis time. Bottom: same, but for the 6 hr forecast.	166
8.8	Change in the fractional dropoff \mathcal{F} and 3 km maximum wind between the analysis time and 6 hr forecast.	167
8.9	Vorticity field at 700 mbar from a Karl (2010) simulation, showing high-resolution features in the 3 km domain.	167
8.10	Change in the fractional dropoff \mathcal{F} and 3 km maximum wind between the analysis time and 6 hr forecast.	168
9.1	Median cloud top temperature from 2010 North Atlantic basin simulations of the high-resolution HWRF model, conditioned on Saffir-Simpson category. Top left (9.1a): 24 hr forecast, top right (9.1b): 48 hr, bottom (9.1c): 72 hr.	177
9.2	Peak (1st percentile) cloud top temperature from 2010 North Atlantic basin simulations of the high-resolution HWRF model, conditioned on Saffir-Simpson category at 24 hr forecast.	179
9.3	Peak (1st percentile) cloud top temperature from 2010 North Atlantic basin simulations of the high-resolution HWRF model, conditioned on RI versus non-RI at 24 hr forecast.	180
A.1	Left: an example of the rotated latitude-longitude grid. Right: the same grid, zoomed in on the Carribean. H (mass) grid points are in red and V (velocity) grid points are in blue.	193

List of Abbreviations

\mathcal{A}	autocorrelation
c	speed of light
c_s	speed of sound
f_v	wind dropoff fraction relative to truth value
k_B	Boltzmann's constant
L	transition scale
\mathcal{L}	correlation length
\mathbf{p}	hydrostatic pressure
p	pressure (including non-hydrostatic component)
\mathcal{I}	increment
q or q_v	water vapor mixing ratio
\vec{r}	location
S_n	n th order structure function
T	temperature
T_b	brightness temperature
T_d	dewpoint temperature
\vec{v}	velocity
v_{max}	storm maximum one minute sustained (averaged) ten meter wind
λ	longitude
ϕ	latitude
θ	potential temperature
θ_e	equivalent potential temperature
$X =_d Y$	RV X has the same distribution as RV Y
AOML	NOAA Atlantic Oceanographic and Meteorological Laboratory
ARW	Advanced Research WRF
CDF	Cumulative Distribution Function
dbZ	Decibels of Z
DTC	Developmental Testbed Center
EMC	NCEP Environmental Modeling Center
GFDL	Geophysical Fluid Dynamics Laboratory
GFS	Global Forecasting System
GRIB	Gridded Binary file format
GSI	Gridpoint Statistical Interpolation

HHS	HWRF History Sequence automation system
HRD	AOML Hurricane Research Division
HWRF	Hurricane WRF
HyCOM	Hybrid Isopycnal-Sigma-Pressure (generalized) Coordinate Ocean Model
IBM	International Business Machines
JTWC	Joint Typhoon Warning Center
kn	knot
LES	Large Eddy Simulation
LSM	Land Surface Model
MPI	Maximum Potential Intensity or Message Passing Interface
NCEP	NOAA National Centers for Environmental Pre- diction
NHC	NCEP National Hurricane Center
NMM	Nonhydrostatic Mesoscale Model
NOAA	National Oceanographic and Atmospheric Admin- istration
NORAD	North American Aerospace Defense Command
PBL	Planetary Boundary Layer
PDF	Probability Distribution Function
POM	Princeton Ocean Model
PR	TRMM Precipitation Radar
P3	Lockheed WP-3D Orion Aircraft
RI	Rapid Intensification or Rapidly Intensifying
RV	Random Variable
RMW	Radius of Maximum Wind
SAS	Simplified Arakawa-Schubert
SF	Structure Function
SS	Saffir-Simpson
SST	Sea Surface Temperature
TC	Tropical Cyclone
TCVitals	Synthetic Tropical Cyclone Vitals Database
TRMM	Tropical Rainfall Measurement Mission
UMBC	University of Maryland Baltimore County
UTC	Coordinated Universal Time
VHT	Vortical Hot Tower
VIRS	TRMM Visible and Infrared Scanner
WISHE	Wind-Induced Surface Heat Exchange
WMO	World Meteorological Organization
WRF	Weather Research and Forecasting Model
3DVAR	Three-Dimensional Variational Data Assimilation

Chapter 1

Introduction

Historically weather simulations have used grid scales and time scales much larger than the convective scale out of simple computational necessity. As computer technology advances with time, finer grid scales become possible, and the features one does and does not resolve change (Lynch, 2008; Leslie and Dietachmayer, 1992). Simulations much larger than the convective scale allow convective and diffusive effects to be modeled using parameterizations (e.g., see Narita and Ohmori, 2007; Moorthi and Suarez, 1992; Lord, 1982). That is, rather than explicitly resolving convection cells, horizontal waves or eddies, one predicts how unresolved processes would modify the resolved quantities, based on resolved quantities. Now it is feasible to use grid scales around 1–4 km in real-time systems (Zhang et al., 2010; Davis et al., 2008). That range of scales raises a difficulty in tropical cyclone dynamics because of critical dynamical processes in tropical cyclones around that scale.

One example of this trouble is convection cells, which are often the order of 1–4 km in size, as will be discussed in this thesis. Neither usual approach to modeling convection works. Statistical assumptions of many convection cells per grid cell break down when only a handful of convection cells are present. Similarly, the fine-scale structure of a convection cell cannot be resolved with only a few gridcells (Bryan et al., 2003). Perhaps more importantly, rearranging the entire vertical

column of the atmosphere in one timestep (a few seconds), as some convection parameterizations do (e.g. Narita and Ohmori, 2007; Lord, 1982), risks destroying whatever features near that scale the model was explicitly resolving, including any waves or eddies.

However, one could hope that when disabling the convection parameterization, even though the fine-scale structure of the convection cells will remain unresolved, their effects will still be resolved. To determine whether this is the case, a comparison of convection-scale model features to the real world observations is needed to determine if convection is being represented correctly, or to determine in what ways it deviates from reality. Convection is only one example of a small-scale process in tropical cyclones; other small-scale processes exist around that scale. In all cases, some form of model diagnostics are required to determine how the model's small scales differ from reality. Fortunately, tropical cyclone observations do exist at these scales, and so a comparison can be done.

The typical approach used in tropical cyclone model diagnostics is, “does the storm have the right intensity, structure and size?” While that approach may be a good one for storm-scale diagnostics, it is not appropriate for diagnosing smaller, convective-scale features. Such features are chaotic and dependent on threshold processes. It not feasible to expect a model to place individual convection towers in the exact same location at the exact same time as in the real world. The same goes for rainbands, shear instabilities and the mesovortices they spawn, and other features near the 1–4 km scales of interest to this thesis.

In addition, a model diagnostic for the small scales is a very poor one if it

requires the storm scale (track, intensity, etc.) of every forecast to be the same as the real storm. The model storm is rarely the same as the real-world storm. Even in the best of real-time simulations, by the 72 hr forecast, the storm will be 50 km or farther from the storm fix position, and 15 knots or more apart from the right intensity. A 50 km difference can mean the difference between landfall over an island, or continuing over warm water; it can mean the difference between taking the north or west fork at a hyperbolic point. The effects on the storm one day later can be gigantic.

Researchers performing research simulations can redo their simulation over and over until they have a storm with the right track, intensity and structure, on which to perform their diagnostics. In real-time forecasts, that is not an option; you get one chance to do a simulation in every forecast cycle and have a very limited amount of resources in which to even run that simulation. Some of the forecasts are bad forecasts, and those are the forecasts that need diagnostics the most.

There is a solution to this: if there are characteristics of the smaller scales that are independent of the storm, then this provides us with a way to do small-scale model diagnostics even on bad forecasts. To achieve that goal, the observational analysis in this thesis is based primarily on two types of statistics:

- universal statistics — statistical patterns that are seen in small-scale statistics in every storm, regardless of storm-scale conditions. An example of this is convection cells having a typical size, regardless of storm-scale structure.
- bulk statistics — statistical patterns that are seen when many storms are

combined. An example of this is rapidly intensifying storms having higher 1st percentile cloud tops than other storms.

The same statistical analysis is then performed on the model, and compared to the results found in the real world. A physical understanding of the dynamical processes behind these statistics then reveals problems in the model.

1.1 Organization of this Thesis

This thesis is organized as follows:

Chapter 2: *The Anatomy of a Tropical Cyclone* — A review of tropical cyclone structure and dynamics, from the environmental scale down to the convection scale.

Chapter 3: *Scale Analysis of Near-Convective Scale Dynamical Processes* — Begins the observational data analysis with a multi-scale analysis of in-situ wind data from the NOAA WP-3D Orion aircraft. Explains the benefits of two-point statistics in tropical cyclone data analysis.

Chapter 4: *Wind Bias in the Utopian Model* — Introduces the theoretical construct called the *Utopian Model*: a perfect finite difference model; one whose forecasts are the real world, contained in a finite difference grid. Estimates are made for the drop in maximum one minute sustained (averaged) 10 meter winds as the resolution of that grid is decreased. This gives an estimate of the lower bound of the error in intensity that is due solely to model resolution.

Chapter 5: *TRMM Satellite Overpass Database* — Explains how a database of 2081 TRMM satellite overpasses of 827 tropical cyclones was developed.

Chapter 6: *TRMM Statistical Analysis* — Performs a bulk statistical analysis of the TRMM database, analyzing cloud tops and their relationship with intensity or intensity change.

Chapter 7: *High-Resolution HWRF: Design, Rationale and Bugs* — describes the experimental high-resolution version of the NCEP HWRF model, which is planned to be the 2012 version of HWRF subject to resource requirements. Discusses the decisions that one must make in creating a high-resolution model, and explains the choices made when designing high-resolution HWRF. Also discusses a bug found in the model, and the large improvement seen in the forecast when that bug is corrected.

Chapter 8: *Model Diagnostics: In-Situ Data* — performs model diagnostics comparing model fields to in-situ data.

Chapter 9: *Model Diagnostics: Cloud Tops* — statistically compares model cloud tops from many simulations to observed cloud tops.

Chapter 10: *Conclusions and Future Work* — summarizes and discusses results from all chapters, and discusses future directions for this research.

Three appendices provide additional details:

Appendix A: *Numerical Prediction of Hurricanes* — explains, in detail, the HWRF model, and briefly explains some aspects of its parent global model GFS.

Appendix B: *Observations of Tropical Cyclones* — discusses some remote sensing methods that are used in this thesis.

Appendix C: *Adventures in High-Resolution Modeling* — contains stories about other modeling issues that had to be confronted during the design of the high-resolution HWRF.

Chapter 2

The Anatomy of a Tropical Cyclone

This chapter is a brief review of the structure and dynamics of tropical cyclones over a range of spatial scales.

2.1 Tropical Cyclones: The Basics

A tropical cyclone is a rapidly spinning vortex that forms in the warm tropical oceans and seas. The strong azimuthal flow (the *primary circulation*) is coupled to a secondary in-up-out circulation (the *secondary circulation*) that brings warm, moist air into the eyewall where it rises and releases latent heat that provides energy for the storm (Simpson et al., 2002). There is lateral outflow at the top of the storm, with some of the air descending and warming in the eye (Emanuel, 1997; Schubert et al., 2007; Kuo, 1959; Malkus, 1958).

To lowest order, the primary circulation in a tropical cyclone is in hydrostatic and gradient wind balance, where the radial pressure gradient, Coriolis force and centrifugal force are balanced (Malkus and Riehl, 1960; Willoughby, 1990). Analytical works often assume cyclostrophic wind balance near the radius of maximum wind, a simplifying assumption that some believe to be reasonable (Emanuel, 1997). The system is a warm core low; the central surface pressure is low and the core of the storm is much warmer than the environment. The thermal wind relation, which

relates the radial gradient of temperature to the vertical shear of the azimuthal wind, can be used to show that the strongest winds are close to the surface. (Wang and Wu, 2004; Simpson et al., 2002)

The secondary circulation arises from a combination of friction (i.e. momentum transfer to the surface layer and ocean), which allows a radially inward flow that would otherwise be discouraged by the Coriolis force. However, this would drive a shallow circulation due to vertical stability. Latent heat release at midlevels drives the deep in-up-out circulation with rising motion in the eyewall and outward flow at the top (10km or higher). (Eliassen, 1951; Shapiro and Willoughby, 1982). The warm temperature of the eye is thought to be maintained by subsidence warming of the air descending in the eye, but the origin of the subsidence is a topic of debate (Willoughby, 1998; Emanuel, 1997).

The thermal structure of the eye consists of a mid- to upper-level warm perturbation that extends into the eyewall. The bottom of the perturbation creates an inversion that acts as a fairly effective barrier to transport. Despite this, air is transported into the eye under the inversion where it spends a while picking up extra moisture from the storm. Since the air cannot rise upward through the inversion (typically), it enters the eyewall and can act as an additional source of energy for the storm. (Cram et al., 2007; Montgomery et al., 2006)

In addition to this large-scale structure, observations of tropical cyclones show that their inner core region of often contains smaller scale flow structures in the eye and eyewall, including elliptical or polygonal eyewalls (Wang and Wu, 2004; Montgomery et al., 2006) and small, intense vortices, some smaller than 1km in

diameter (Aberson et al., 2006). These flow structures can sometimes be seen in cloud patterns or other observations (Lewis and Hawkins, 1982). They have been demonstrated in idealized numerical simulations (Möller and Montgomery, 1999; Chen and Yau, 2001) and full physical simulations (Wang, 2002a; Corbosiero, 2008). Small-scale features are of interest because they are thought to play a role in tropical cyclone intensity change by facilitating transport of energy and angular momentum between the outer storm, eye and eyewall (Montgomery and Kallenbach, 1997). In addition, they can cause extreme, localized damage due to local increases in wind (Montgomery and Kallenbach, 1997).

A tropical cyclone forms a heat engine, driven by latent heat release. It brings in warm, moist air from the synoptic environment at low altitudes, further warming it and moistening it as it is pumped in along the ocean surface. It then forces the air up to high altitudes through convective processes, and then expels it at high altitudes into the cooler synoptic environment through tropical cyclone outflow bands. There are a number of factors that can increase or decrease this heat engine's efficiency, at the synoptic scale, the storm scale and the convective scale.

Of course, the anatomy of a tropical cyclone isn't quite as simple as described above. There are numerous complications brought on due to interactions with the synoptic-scale environment, the underlying ocean, the tropopause, and various small-scale features. The vast majority of those features and interactions are unrelated to this thesis, which focuses on small-scale inner-core atmospheric dynamics. However, essential aspects of tropical cyclones will be reviewed.

2.2 The Environmental Flow

Tropical cyclones are not stand-alone phenomena — they interact strongly with the synoptic-scale atmospheric flow in which they are embedded. The cyclone’s track is determined primarily from the synoptic-scale winds, and the intensity can be significantly impacted as well. In analyzing these impacts, it is useful to divide the atmospheric fields into an “environmental flow” component and a “vortex flow” component:

$$X(\phi, \lambda, z) = X_c(\phi, \lambda, z) + X_e(\phi, \lambda, z) \quad (2.1)$$

where X can be any scalar or vector quantity, and e and c subscripts indicate the environmental and vortex (“c” for “cyclone” or “anticyclone”) components, respectively. Temperature is T , velocity is \vec{v} , pressure is P , q is the water vapor mixing ratio, λ is longitude and ϕ is latitude. That notation will be used throughout the rest of this thesis.

Tropical cyclones tend to largely follow the environmental winds. In other words, to a “zeroth-order” approximation, the tropical cyclone acts as a vortex that is stationary relative to the environmental flow. The environmental flow is impacted by a multitude of different synoptic-scale phenomena, including the inter-tropical convergence zone (ITCZ), subtropical jet, various ridges and troughs, and any other nearby tropical cyclones. Despite the scale of these influencing systems, they can still lead to difficult to predict situations. See Figure 2.1 for an example: Hurricane Fay (2008) is heading north-west towards a hyperbolic point in the flow created by several nearby high and low pressure systems. The hurricane may go north or west,

Brightness Temperature (K), ~6.5 μ m Water Vapor Band
GOES-12 Ch. 3 2008-08-22 11:10:00

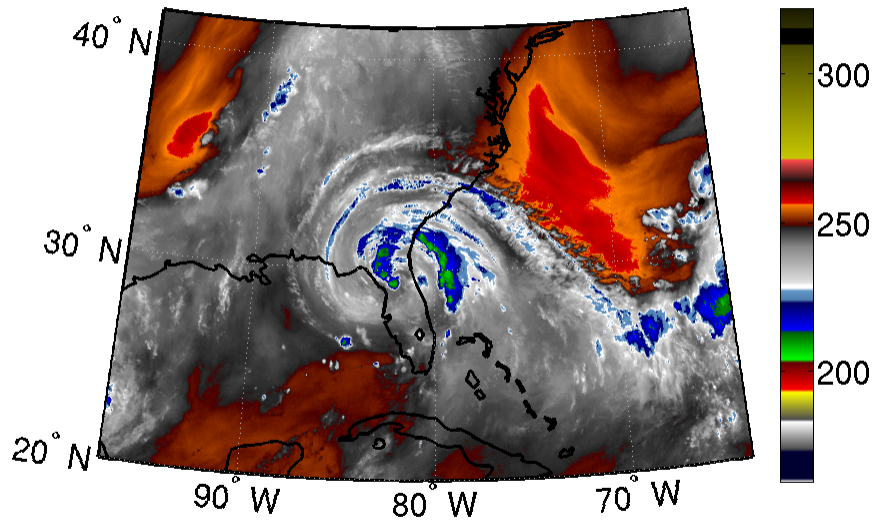


Figure 2.1: Hurricane Fay (2008) on August 22 at 11:10 UTC, heading northwest towards a hyperbolic point in the flow created by several high and low pressure systems.

but it is hard to forecast which one because even small changes in the synoptic scale can change the outcome.

The cyclone itself can have an impact on all of those nearby systems, due to its powerful lower-level inflow, and upper-level outflow. The more powerful the cyclone, the larger of an impact it will have. Very strong cyclones can sometimes overpower synoptic-scale systems, while weaker ones will be dissipated. Despite this, the synoptic-scale environment is the dominant force in determining the cyclone's track. (Kasahara and Platzman, 1963; Simpson et al., 2002; Merrill, 1988; Frank and Ritchie, 1998; Emanuel, 2007; Landsea et al., 1998).

This leads to one common forecasting tool: the 500mbar geopotential heights. One can get a track for the storm by advecting a passive tracer with a constant pressure-level velocity field from $\vec{v}_e(\phi, \lambda; P)$ (Kasahara and Platzman, 1963). In practice, there is no perfect way to separate the environmental and vortex components of the flow. Fortunately, nature has already provided for us.

Recall that the tropical cyclone inflow and outflow spiral in opposite directions. That means that there is a level in the storm (typically about 500 mbar) where, to some extent, the flow is neither in nor out, and is neither cyclonic nor anticyclonic. The dominant motion is upward motion due to convection, and horizontally from the environmental wind. This region tends to approximate geostrophic balance so the 500 mbar geopotential heights can be used to determine velocity.

Of course, as mentioned before, the large-scale 500 mbar geopotential heights are impacted by a multitude of different synoptic-scale phenomena. In addition, the innermost regions of tropical cyclones have a thermodynamic structure that leads to modifications of the geopotential heights at all levels, due to the powerful convection present there. However, trained forecasters are able to use 500 mbar geopotential heights, and experimental numerical models decades ago used tracers within an environmental flow to track tropical cyclones (Kasahara and Platzman, 1963).

In addition to deciding the track of the storm, environmental flow can shear the vortex. Environmental winds that are stronger at high levels than low levels, or vice-versa, contribute to the so-called “environmental shear vector” (usually, simply

called the “shear”) defined as such:

$$\overrightarrow{v_{esh}} = \int_{vortex} \overrightarrow{v_e}(\phi, \lambda, 200 \text{ mb}) - \overrightarrow{v_e}(\phi, \lambda, 850 \text{ mb}) dA \quad (2.2)$$

Values of 200 mbar and 850 mbar are the levels traditionally used for the shear vector. They are chosen since they are typically within the outflow and inflow layers, respectively. The stronger that shear vector becomes, the harder it is for the tropical cyclone to maintain its outflow, and its warm core. Shear is believed to be the one of the most dominant effects in determining tropical cyclone intensity, and genesis (original formation of the tropical cyclone vortex). Another dominant effect is the sea surface temperature. These are both well-established, with one of the earliest papers being Weightman (1919), and many since then (e.g.: Paterson et al., 2005; Wang and Holland, 1996; Frank and Ritchie, 1998; Emanuel, 1999).

2.3 Moisture: The Sea, Wake and Rainbands

As mentioned earlier, the tropical cyclone gets nearly all of its energy from latent heat release. The latent heat comes from the ocean surface through moisture fluxes. Hence, anything that can increase, decrease or interrupt the flow of the latent heat to the tropical cyclone inner core will have an impact on its intensity, and a different intensity can lead to a different track through interactions with the environment.

One large contributor to this is the sea surface temperature (SST) under the storm. Cooler SST will deposit less heat into the atmosphere, while warmer temperatures will deposit more. The cyclone's intensity is extremely sensitive to sea surface temperatures. In fact, a difference of two degrees Kelvin can mean the difference between a minor category 1 hurricane and a category 5 (DeMaria and Kaplan, 1994; Emanuel, 1988, 1991). This leads to one of the largest impacts a storm's track can have on its intensity: if the track leads the storm over a cold region of the ocean, the SST will be lower and hence the storm will usually weaken.

The interaction with the sea surface isn't as simple as the temperature of the surface, due to stirring of the ocean caused by interactions with the vortex. The ocean is divided vertically into the mixed layer, the thermocline layer and the thermohaline layer. The mixed layer is the topmost layer, and is the layer that interacts strongly with the atmosphere on a regular day-to-day basis and is much warmer than the rest of the tropical ocean. The thermohaline layer makes up the bulk of the ocean, beginning 100m or farther below the ocean surface and extending

nearly to the bottom. It is largely independent of interaction with the sun, and is much cooler than the mixed layer. In between, there is a transition layer known as the thermocline layer.

The storm vortex forces turbulence in the mixed layer that can stir thermocline water up into the mixed layer, cooling the ocean surface (Prince, 1981; Price et al., 1996). Hence, stronger storms will leave behind a trail of cool sea surface temperatures known as the storm's "wake." The slower the storm moves, the more it will weaken due to the cool ocean temperatures. If it moves over another storm's wake, or its own wake from hours or days in the past, then the storm will weaken.

Due to this, the total ocean heat content, a measure of the total amount of heat in the mixed layer and upper thermocline, is also an important factor in tropical cyclone intensity (Mainelli et al., 2008). This effect has been taken into account for years by the GFDL and HWRF models by initializing the Gulf of Mexico Loop Current, not just with warm sea surface temperatures, but with the correct amount of underlying ocean heat content (Bender and Ginis, 2000; Developmental Testbed Center, 2010).

There is a second feature that can impact the inflow of warm, moist air, and that is the rainbands. A rainband is a band of convection outside the tropical cyclone's eyewall. The convection in the rainband interrupts the inflow of moist air, expelling it before it gets to the inner core (Willoughby et al., 1982; Willoughby, 1988; Jr. et al., 2006). This weakens the inner core of the vortex, expanding the storm's radius, increasing the pressure and decreasing the warm core temperature (Jr. et al., 2006; Willoughby, 1988; Willoughby et al., 1982). All of that leads to a

larger storm with a smaller pressure perturbation and lower wind speeds.

In addition, rainbands throughout the storm will sometimes join to form a circle of convection, effectively a second eyewall. That can lead to an *eyewall replacement cycle*, in which the outer eyewall cuts off all flow to the inner eyewall, killing it off and leaving the storm larger and with lower wind speeds and a smaller pressure perturbation (Willoughby et al., 1982; Willoughby, 1988; Willoughby et al., 1984; Samsury and Zipser, 1995; Black and Willoughby, 1992).

While the increased storm size from rainbands or second eyewalls may weaken the pressure perturbation and maximum winds, they can actually increase the overall kinetic energy of the storm, and as a result, the height of the storm surge (Irish et al., 2008). Here, the *storm surge* is the overall increase of the height of the sea surface as a result of all effects combined: presence of waves, raising of the surface due to the low pressure center of the storm, and other effects as well. The largest of those “other effects” is a vortex produced in the ocean by the tropical cyclone. The underlying ocean spins, pushing water away from the storm center, where it then increases in height in the outer regions of the storm.

The storm surge and waves typically cause more death and property loss than wind does. One example of this is the 1900 Galveston Hurricane, which had a higher death toll than any other natural disaster to hit the United States since the country’s founding, and ranks as the third deadliest Atlantic basin tropical cyclone in recorded history. The city’s highest point was only 8.7 feet above sea level, and the storm surge reached about 15 feet. The resulting force blew over nearly all houses and other man-made structures, leaving only a few well-built mansions with

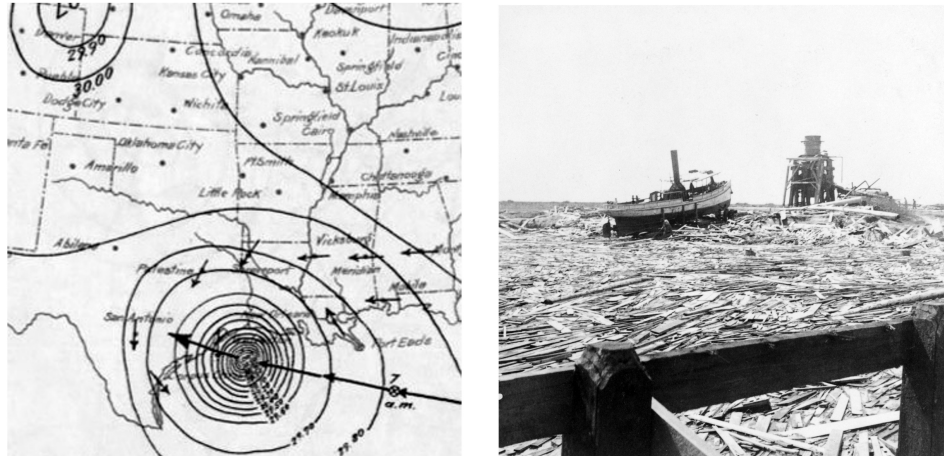


Figure 2.2: The Galveston Hurricane of 1900. Left: surface pressure field analysis courtesy of NOAA, showing the hurricane making landfall. Right: wreckage of broken houses washed out to sea by the storm surge.

solid foundations. This can be seen in Figure 2.2.

After the 1900 Galveston Hurricane, a seawall was built, and the city was, to some extent, rebuilt. However, in 1915, a second powerful hurricane hit the rebuilt city, causing widespread flooding and permanently changing the beach structure, eroding 300ft of shoreline. Fortunately, the Galveston Seawall held, stopping the kinetic energy of the waves and advancing storm surge from hitting buildings.

2.4 Terrain Effects

As discussed briefly in the previous section, tropical cyclones interact with the terrain beneath them as well. The largest impacts are increased rainfall over mountainous terrain, the lack of inflowing moisture due to the lack of an ocean surface and slowing of the tropical cyclone's motion.

The lack of inflowing moisture is a large impact; tropical cyclones can dissipate within hours of making landfall. However, islands that are much smaller than the tropical cyclone can have a relatively small impact since they restrict a smaller percentage of the inflow. Also, some surface types such as marshes are warm enough and wet enough to provide moisture and sustain the cyclone's intensity, or at least reduce its weakening.

Moist air from the tropical cyclone that is heading towards a mountain will undergo forced ascent and adiabatic cooling. This then condenses water vapor and causes severe rain along the mountain's horizontal extent. This effect occurs in tropical cyclones, but to a phenomenal extent, producing as much as a foot of rainfall per day. This is one way in which supposedly "weak" (higher pressure center, lower wind) storms can cause more damage than supposedly "stronger" storms – the larger the diameter of the storm, the higher the chances are of having a mountain under a rainband.

In addition, rough terrain tends to decrease the speed of wind above it throughout the habitation layer (approximately the first 1 km). That will slow the speed of not only the small-scale wind, but the environmental flow as well. Slower environ-

mental flow means slower-moving storms. If a storm moves slower over a mountainous area, the negative impact of the rough terrain on the storm winds can kill off the storm unless some other effect strengthens it. If another effect strengthens the storm, such as a warm sea surface, then the result will be a slow-moving tropical cyclone, pounding the same coastline over and over for days. Also, the slowing of the lowest 1 km results in severe shears, leading to shear instability induced boundary layer rolls, which can provide strong localized wind.

Two good examples of this are Hurricanes Mitch (1998) and Fifi (1974) (see Figure 2.3). Those were the second and fourth deadliest Atlantic basin hurricanes in terms of deaths, and caused most of their deaths and destruction through flooding, and mudslides in the mountain ranges in Honduras (Guiney and Lawrence, 1999; Center, 1974). Both were relatively weak storms, but moved very slowly in warm, deep waters (thick mixing layer), constantly pumping moist air towards the mountains, where they rained out over the same areas, over and over.

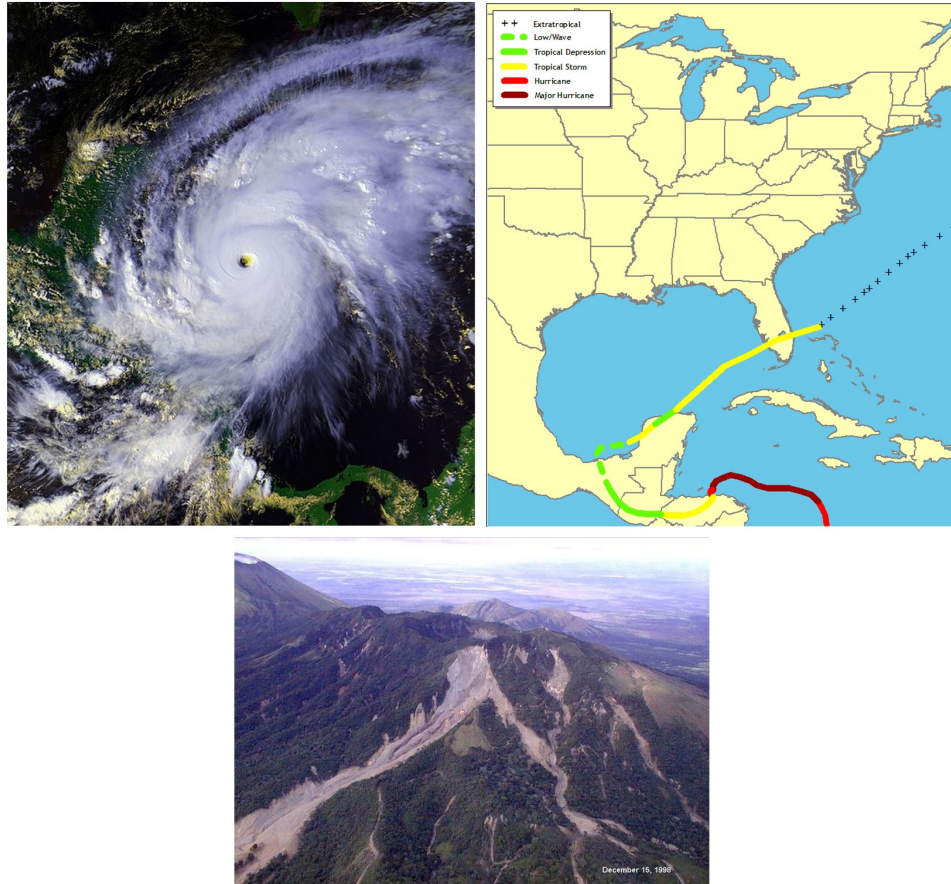


Figure 2.3: Hurricane Mitch (1998). Top left: satellite image of Mitch near its peak intensity as a Category 5 Hurricane. Top right: track of Hurricane Mitch. Bottom: mudslides on the Casita Volcano. Images courtesy of NOAA.

2.5 Inner-Core Structure

The tropical cyclone inner core region is the region that contains the eye, eyewall and inner rainbands. Many papers define this region as everything within twice the radius of maximum wind, which for a storm in gradient wind balance, is also twice the radius of maximum radial pressure gradient. In this violent region of the storm, there are powerful convection towers, strong wind gradients that can spawn vorticity waves or mesovortices, and torrential downpours that drop a river of rain every minute. Such extreme conditions spawn many different features that can modify the intensity of the storm.

One of the earliest examples of this was polygonal eyewalls. Since the entirety of the cyclones' eye can only be observed by radar or satellite, it was originally thought that the polygonal shape was an artifact of a measurement device, or perhaps a topographical effect. The first comprehensive study of polygonal eyewalls was Lewis and Hawkins (1982). That study used two different radars over water to examine several tropical cyclones and verify that they had polygonal eyewalls. The authors even did a survey, showing people motion pictures of the spinning polygons to verify that a majority of those asked believed that the eyewalls were polygonal. Another significant study (Muramatsu, 1986) used radar snapshots of Typhoon Wynne's eye every 10 minutes for 36 hours. The radar was stationed on a small, isolated pacific island in the eye of the storm. The authors witnessed several different polygonal shapes ranging from squares to hexagons, each shape lasting about 30-50 minutes. They also saw a number of small pockets of convection in the



Figure 2.4: Hurricane Isabel (2003) eye and eyewall, as seen from the International Space Station. In the bottom right, convection is seen detraining, and generating gravity waves. Inside the eye, several mesovortices are seen. Near the back in the eye, a hot tower is present. Thin cirrus clouds cover portions of the eye. Spiral clouds are seen climbing up the eyewall to the right.

eye and eyewall. They mentioned a number of past pacific storms with polygonal eyewalls, all of which resulted in similar observations. Polygons with more than six sides have not been observed and the number of sides can change in under an hour (Muramatsu, 1986; Lewis and Hawkins, 1982).

Even after their existence was proven, these polygonal eyewalls were thought to be curiosities rather than a sign of important underlying dynamics. We now know that these polygons are the result of vorticity waves that vary azimuthally

in a sinusoidal manner and can even spawn mesovortices. Both of those dynamical features can impact intensity.

These so-called vortex Rossby waves form in tropical cyclones in regions of strong radial gradients of vertical vorticity. Wave-like patterns move retrograde azimuthally and include large regions of increased or decreased vorticity, divergence, moist convection and vertical motion (Reasor et al., 2000; Kuo et al., 1999). These form due to a combination of barotropic (Smith and Rosenbluth, 1990; Montgomery and Kallenbach, 1997) and baroclinic (Chen and Yau, 2001; Wang, 2002b,a) instability in the high-shear regions of the tropical cyclone. The perturbed vorticity is sometimes interpreted as a mesovortex embedded in the eyewall. Mesoscale vortices, 2-20 km in diameter, are often seen in the eye of a tropical cyclone, the most famous case being in Hurricane Isabel that contained as many as six eye mesovortices at a time (Kossin and Schubert, 2004).

These waves and mesovortices require strong shear regions in a tropical cyclone, and such regions are fairly well-studied and known to exist. Kossin and Eastin (2001), using observations from forty-four hurricanes over twenty years, showed that there appear to be two flow regimes in tropical cyclones. The first regime tends to be associated with intensifying storms. The vorticity is concentrated in a narrow annulus in the eyewall. The shear between the eye and the inner eyewall is strong — the mean wind speed can drop by tens of meters per second over a kilometer (Kossin and Schubert, 2001). There is another, weaker shear region on the outside edge of the tropical cyclone eyewall at a radius greater than the Radius of Maximum Wind (RMW). This first regime typically has regions of high θ_e in the eyewall with warm,

dry eyes (Kossin and Eastin, 2001). The second regime is usually associated with weakening storms. It consists of enhanced angular velocity in the eye and decreased eyewall θ_e . Dewpoints are increased significantly over the first regime while θ_e profiles are monotonic with maxima at the center of the eye (Kossin and Eastin, 2001).

The ways in which such small-scale features impact intensity is complex and still not well-understood. One way in which small scales can impact intensity is via radial eddy transport associated with mesovortices or breaking vorticity waves which can transport dry air from the outer part of the storm in the so-called *anti-fuel effect*, decreasing the storm intensity. It can also transport high- θ_e air into the eyewall from the eye — the *fuel effect*, increasing the intensity of the storm, a mechanism originally proposed by Malkus (1958). These effects were shown to be present in Bonnie in Cram et al 2006, the fuel effect was shown to cause some of Isabel (2003)'s high intensity, examined by Montgomery et al. (2006).

In addition, these features can increase intensity due to a completely artificial reason. Tropical Cyclone intensity in the US is defined as the one minute sustained (averaged) ten meter altitude (nominal anemometer altitude) wind. Any features large enough to be present over an anemometer for 60 seconds during storm passage will increase the storm intensity according to this artificial definition. Even features that are not large enough to last 60 seconds can still increase the average over that 60 seconds.

Another effect in the inner core region is the *Hot Tower*. The results of Kelley et al. (2005) that show that intensification follows the appearance of tall precipitating towers reaching as high as 14 km. Hot towers are thought to be related to

the intensification of storms by adding to the fuel effect through strengthening the upper-level subsidence and also contributing to mid-level latent heating. They are thought to be significantly less diluted than other convection (Zipser, 2003) leading to higher convection efficiency. In some cases these hot towers are vortical, known as Vortical Hot Towers (VHT), and the strong vorticity shear across the tower helps prevent dilution.

2.6 Additional Effects

The above mentioned features are just some of many that are observed in tropical cyclones. Furthermore, there is no reason to believe that we have discovered all of the critical small-scale dynamical processes that can modify tropical cyclone intensity or track.

There are a few other notable features in tropical cyclones not yet discussed. One such feature is boundary layer roll vortices, which are vortices parallel to the ground that exist in the tropical cyclone boundary layer. For example, the Doppler On Wheels project found that these rolls are associated with strong horizontal wind streaks near the ground, which were able to create extreme localized wind damage, from transporting stronger winds aloft down to the surface through pairs of counter-rotating vortices (Schroeder, 1999; Wurman and Winslow, 1998). In many tropical cyclones, these roll vortices were observed in the boundary layer (Morrison et al., 2005) and can play a significant role in heat and momentum transfer between the tropical cyclone and ocean (Zhang et al., 2008b; Foster, 2008). It may be possible for these horizontal vorticity structures to be tilted into the vertical, which would give rise to very small vertical vortices. This type of mechanism is involved in tornado genesis. This would give rise to misovortices, with scales much smaller than the mesovortices in the inner core (in particular, misovortices are nominally 40–2000 meters in scale). Misovortices were observed in the eyewall of Isabel (Aberson et al., 2006) that appeared to form from one of many fingers of cloud on the inner edge of the eyewall. In addition, these roll vortices usually appear in sheets of

rolls whose vorticity alternates in sign. These sheets have typical wavelengths of 3–12 km (Morrison et al., 2005), and often have associated alternating updrafts and downdrafts (Foster, 2005; Weckwerth et al., 1997b,a). As with vorticity waves and mesovortices, these roll vortices can have a direct impact on the typical measure of storm intensity — one minute sustained 10 meter wind — if the roll (or sheet of rolls) is over an anemometer for a significant portion of a minute.

Another feature, of a much larger scale, a “wake” left in the tropopause, similar to the “wake” left in the ocean. Tropical cyclone convection pushes the tropopause up in convective regions, and pulls it down in non-convective regions. There is also a downward motion of a much larger vertical extent in the outflow layer. This variety of upward and downward motion can leave streaks of high or low tropopause heights along the track of the cyclone. Tropopause height is important in tropical cyclone convection as it is the “cap” of convection. The tropical cyclone has a great deal of difficulty pumping air above the tropopause due to the extremely stable stratospheric air above that. Despite that, the tropical cyclone convection does approach and occasionally penetrate the tropopause, with convective towers often reaching 14 km or higher. This leads to an upper-level cold core above the tropical cyclone warm core, with the cold core often reaching well into the stratosphere (Koteswaram, 1967). That can lead to a mixing of tropospheric and stratospheric air and is a dominant effect in impacting ozone on a seasonal timescale, especially due to the injection of water vapor into the stratosphere, where it typically has a long lifetime (Jiang et al., 2004).

2.7 Superintense Storms and Rapid Intensification

Until recently the prevalent view on how tropical cyclones intensify is based on wind-induced surface heat exchange (WISHE). This theory is now known to be incomplete. It includes only axially symmetric effects and makes many other simplifications, causing it to ignore hot towers, mesovortices, ocean heat content, and many other effects. Based on this theory was the Maximum Potential Intensity (MPI) theory, which predicts limits to tropical cyclone intensity based on sea surface temperature and other aspects of the synoptic environment based on axially-symmetric reasoning. That has led to the concept of “superintense” storms, storms that have exceeded the intensity that would be possible under the assumptions of WISHE and MPI.

WISHE theory was proposed as an alternative to another, theory of intensity known as the convective instability of the second kind (CISK), where environmentally-forced CAPE feeds the vortex (Charney and Ellassen, 1964; Smith, 1997; Ooyama, 1964). CISK is now known to be wrong, due to CAPE in tropical cyclones typically being small and due to CISK’s ignoring of the importance of wind-induced latent heat release (Persing and Montgomery, 2005), the basis of WISHE.

WISHE begins at the turbulent sea surface beneath the tropical cyclone, where moisture fluxes into the atmospheric surface layer are enhanced by wind-induced sea surface turbulence. WISHE assumes the standard bulk aerodynamic relative humidity flux formulation. The specific humidity q_b at the bottom of the atmospheric boundary layer differs from the specific humidity q_s at the near the surface. The

vertical moisture flux from the sea to the top of the surface layer is then related as follows:

$$F_q = C_E(\|\vec{V}\|)\|\vec{V}\|(q_s - q_b) \quad (2.3)$$

where C_E is empirically-derived, and was originally thought to be a constant. It is now known that it is a function of $\|\vec{v}\|$, and large changes occur after about 30 m/s (Zhang et al., 2008a). This F_q increases the water vapor mixing ratio q_v in the surface layer. The theory assumes the increase is stronger in the inner core region (where the wind is stronger), hence increasing $\partial q/\partial r$ at the surface, and consequentially $\partial\theta_e/\partial r$ at the surface. Turbulent boundary layer fluxes then increase the $\partial\theta_e/\partial r$ throughout the boundary layer.

The WISHE theory then assumes the boundary layer is under thermal wind balance, hence an increase in $\partial\theta_e/\partial r$ corresponds to an increase in $\partial v/\partial P$ throughout the boundary layer. That increases the wind speed at the top of the boundary layer, producing a stronger wind at the surface. Therein, the WISHE process loops: the stronger surface wind induces a stronger release of moisture into the atmosphere beginning the process anew. This is a positive feedback process that involves thermal wind balance, implying no secondary circulation, therein creating one of the main flaws in the theory (Montgomery et al., 2009).

However, it is clear that asymmetric effects, and highly localized effects, are critical to tropical cyclone intensification (Montgomery et al., 2009, 2006; Abernethy et al., 2006). In particular, vortical hot towers have been shown in models (Nyugen et al., 2008) and observations (Montgomery et al., 2006; Abernethy et al., 2006) to

be linked to intensification beyond what is thought of as possible under WISHE theory, and to be able to obtain more latent heat locally than WISHE suggests is possible (Montgomery et al., 2009).

An unrelated empirical limitation on intensification comes from the Dvorak method (Dvorak, 1984; Velden et al., 2006), a subjective, but highly successful, method of determining a cyclone’s intensity and location from a static image of infrared imager brightness temperatures. The Dvorak method also predicts the 24 hr intensification of the storm, but that is only used as “first guess” guidance. Empirical tables based on cloud shapes and locations and differences since the last forecast cycle provide an estimated intensity, and a 24 hour forecast intensity. Intensification of more than 43 knots in 24 hours is not included in the Dvorak method, and the limit is much lower for weaker storms.

The Dvorak method, despite its simplicity, has intensity values that are well-validated against both 10 meter anemometer and in-situ airplane data and is currently the dominant tropical cyclone intensity measurement. In many cases, storms far into the ocean have no direct wind measurements, and the Dvorak method is the only method by which intensity can be obtained. However, the prediction of intensification has come a long way since the Dvorak method’s 24 hr tables.

These two theoretical and empirical limits on intensity and intensification led to the concepts of so-called “superintense” storms and “rapidly intensifying” storms. Some storms surpass the maximum potential intensity predicted by Emanuel’s MPI theory. In addition, there are often extremely rapid increases in wind and decreases in pressure depth, beyond that of what MPI and the Dvorak method suggest are

possible. One of the prime examples of these was Hurricane Isabel (2003), an extremely well-measured storm that was found to have an intensity that exceeded its MPI. In Isabel, eye mesovortices advected high θ_e air trapped in the eye into the eyewall below the eye inversion, allowing it to pass the intensity that was predicted by the SST-based MPI theory (Kossin and Schubert, 2004; Montgomery et al., 2006; Aberson et al., 2006).

2.8 Summary and Approach to Model Diagnostics

This chapter has introduced the structure of a tropical cyclone, including many detailed features, some of which involve interactions with land surface, the ocean or the stratosphere. This is, by no means, a complete list of the dynamical features present in tropical cyclones. There are more features known that are not presented here, and likely many more not yet known.

However, it is clear that tropical cyclones are incredibly complex systems that interact with features ranging from convective-scale to synoptic-scale, most of which can impact the storm's track or intensity. In addition, some of these features are sensitive to threshold-based processes, or otherwise chaotic processes, rendering it unlikely that any model, no matter how perfect, will reproduce a feature at the exact same location and time that it does in the real storm.

In addition, the factors that impact any given cyclone are frequently different than the features that impact another. This becomes especially true once one extends analysis to the convective and near-convective scales. Such piece-by-piece comparisons can still be done with careful manual analysis of an individual forecast, if a skilled forecaster or modeler takes into account the impact of differing storm environment and history, between model and reality. However, it would be ideal to spend more time analyzing and improving the model and less time figuring out how to do a correct comparison.

It should now be clear that a system of such complexity and variety, a more sophisticated approach is required than a simple, "does this convective cell have the

right size and shape?” Instead, this thesis takes a statistical approach in the hopes that some aspects of the small-scale dynamics will be consistent regardless of storm structure, intensity or location.

Chapter 3

Scale Analysis of Near-Convective Scale Dynamical Processes

As discussed in Chapter 2, it is apparent that small-scale processes in tropical cyclones are critical to their intensity. Forecasting models must be run at higher resolution in order to resolve those features. An analysis such as “is the hurricane in the right place and is it the right size?” is fine for the entire storm, but asking that same question is not feasible for short-lived, small-scale chaotic flows such as mesovortices or convection cells. Instead, one must search for aspects of the dynamics that are the same across many storms, or aspects that can be quantified by combining many storms’ data.

This chapter develops such an approach using in-situ data from NOAA P3 Orion aircraft measurements. The P3 aircraft observations are in this study because it allows an analysis of ranges from 100 meters to 10 km. For models, one of the reasons why this range of scales is especially difficult is because it is the range in which a transition between parameterized convection and resolved (or partially resolved: Bryan et al. (2003)) convection occurs.

This analysis relies heavily on two-point statistics, which allow one to characterize the dynamics at multiple scales. This has an advantage over other scale analysis methods such as the Fourier transform, in that it is tolerant of missing data. The particular statistics used, the increment PDF and structure function,

have not been used extensively in tropical cyclone data analysis.

The remainder of this chapter is divided as follows:

Scale Invariance and Universality will discuss the concepts of scale invariance, and universality, and how they may apply to small scales tropical cyclones. The *Statistical Concepts and Methodology* section discusses the statistics used and reasons for them, relevant analytical and empirical results from turbulence theory, and how this relate to the underlying dynamics of tropical cyclones. *NOAA WP-3D Orion In-Situ Data* describes the relevant measurement devices, and the measurement platform. The data analysis begins in the *Structure Functions* section, which performs a scale-dependent analysis of in-situ wind measurements, decomposing the wind into radial, tangential and vertical components. Some results are conditioned on saturation, to remove or include convective regions. The *Structure Function Slopes* section analyzes the slope of the radial wind structure function, which is of special interest due to known analytical and empirical results. Then, the *Vertical Wind PDF and Normalized Increment PDF* section analyzes the one-point and two-point PDFs of vertical wind data. The *Volumetric Vertical Flux* section examines volumetric vertical fluxes using a storm compositing method.

This chapter then ends in *Conclusions* section, which summarizes results and explains their implications.

3.1 Scale invariance and universality

A system exhibiting scale invariance is one in which the statistical properties at different scales is invariant under a change of scale. Such systems have no preferred length scale. It is seen in areas of physics, most importantly in phase transitions in which density fluctuations appear at all scales (Wilson, 1979), in fluid turbulence in which vortical structures cascade into smaller and smaller eddies (Frisch, 1995; Stanley et al., 2000). Similar structure is seen in geostrophic turbulence in the atmosphere (Frisch, 1995). Scale invariant (fractal) structure has been found in clouds (Marshak et al., 1997; Davis et al., 1994), scalar mixing (Sparling and Bacmeister, 2001) and in many areas of geosciences (Dimri, 2005). Some of the techniques used in these areas will be used in the data analysis in this chapter.

The Navier-Stokes equations, can easily be shown, with some assumptions, to be scale invariant. A simple derivation will be given here, but this derivation can be made more general. The equations can be written as:

$$\rho \frac{\partial \vec{u}}{\partial t} + \rho \vec{u} \cdot \nabla \vec{u} = -\nabla P + \mu \left(\nabla^2 u + \frac{1}{3} \nabla \nabla \cdot \vec{u} \right) \quad (3.1)$$

and:

$$\frac{\partial \rho}{\partial t} + \nabla \cdot (\rho \vec{u}) = 0 \quad (3.2)$$

Suppose the ∇P term is small, and now make these scaling transformations:

$$\begin{aligned} \vec{x} &\longrightarrow \lambda \vec{x} \\ t &\longrightarrow \lambda t \\ \rho &\longrightarrow \lambda \rho \\ u &\longrightarrow u \end{aligned} \quad (3.3)$$

where we have essentially scaled the coordinate system (and, of course, the density) by a factor λ . In the Navier-Stokes equations above, the λ factor cancels out, indicating that if $\rho(\vec{x}, t)$ and $\vec{u}(\vec{x}, t)$ are solutions, then $\rho(\lambda\vec{x}, \lambda t)$ and $\vec{u}(\lambda\vec{x}, \lambda t)$ are also solutions.

Broadly speaking, in turbulent flows, these equations divide scales into three ranges: the large scales, the inertial range and the dissipation range. In the dissipation range, kinetic energy is converted to thermal energy, and the $\mu\nabla^2\vec{u}$ term dominates. At scales just larger than the dissipation range lies the inertial range where the $\rho\vec{u} \cdot \nabla\vec{u}$ term dominates. Above the inertial range is the forcing scales where energy is input to the system from the outside. In 3D isotropic, homogeneous turbulence, energy cascades downscale from the large scales through the inertial range (Falkovich and Sreenivasen, 2006; Kolmogorov, 1941, 1991, 1962). This cascade terminates at the dissipation scale where kinetic energy is converted to thermal energy.

In 2D turbulence, enstrophy ($\|\nabla \times \vec{u}\|^2$) cascades downscale from large to small scales, while the energy cascade is upscale due to vortex mergers (Frisch, 1995). The scaling range depends on the scale of the forcing which can be small scale. One characteristic of a scaling range is the power law behavior for certain statistical quantities described later. It is likely that forcing and dissipation occur over a wide range of scales in tropical cyclones due to the wide variety of dynamical processes that can occur.

The “two-point” scale-dependent statistics described below also allow an investigation into the properties of *scale invariance*. Scale invariance is a situation

where the statistics are related by a simple change of scale. It is not clear whether a scale invariant range exists in tropical cyclones. There are many features such as the eye, eyewalls, rainbands that may have preferred scales. At smaller scales of a few km or below the situation is not so clear because the forcing from convection is small scale (or could be multiscale), so there might not be much of an inertial range.

A related concept is the idea of *universality*. We use this term here to refer to statistical properties that are the same for all storms, for example, values of power law exponents in statistical quantities.

The importance of universality or scaling symmetry across scales that are marginally resolved, or that are below the model gridscale cannot be overestimated. If some processes existing below the gridscale produce fluxes or heat generation that cannot be represented through turbulent assumptions, then the effects of those processes will not be present in the model. It has been shown that some of these small-scale processes in tropical cyclones influence the large scale, as was discussed in Chapter 2. These symmetries (or lack thereof) might give clues about the small scale dynamics or mixing processes, and will be used later in this thesis to diagnose a high-resolution hurricane model.

This chapter is not meant to be a comprehensive work on tropical cyclone turbulence and scaling. However, it is hoped that it will form the basis of more comprehensive studies on the subject. Furthermore, the statistical properties found here are useful for model diagnostics, as will be seen in Chapter 8.

3.2 Statistical concepts and methodology

3.2.1 Challenges in the application of statistical methods to observations of Tropical Cyclones

Aircraft in-situ observations are a 1D sampling of a system whose statistics may be non-isotropic, non-homogeneous and non-stationary in general. That is, the statistical distribution of wind, temperature, etc. may vary in time (*non-stationarity*), they may vary with sampling direction (*non-isotropic* or *anisotropy*) and they may vary with location (*non-homogeneous*).

There is always the possibility that the observations are sampling a non-representative regime, and in fact it is difficult to say how the small scale variability should be characterized, whether it is sampled sufficiently, and whether the statistics have converged. There is a trade-off between the need to form statistically robust ensembles by compositing while at the same time avoiding compositing across regimes from different statistical populations. It can be difficult to distinguish between different realizations of the same statistical ensemble vs. real differences in statistical populations.

There are also some other aspects of the methodology that have to be considered. In addition to wind measurements, the aircraft provides temperature (T) and dewpoint temperature (T_d) measurements. Unfortunately, those measurements are unreliable due to so-called *wetting errors*. Such errors involve water being blown into the measurement devices by strong updrafts. The dewpoint temperature is then

increased and the temperature is decreased. That leads to the in-situ measurements being supersaturated by extreme amounts during and shortly after updrafts. Due to this, the in-situ temperature and dewpoint temperature will not be used much in this thesis, except as a test for whether the air is saturated.

Also, when the P3 flies through strong turbulence, the plane can pitch or roll. If uncorrected, this would cause immediate, large errors in the wind measurements. These effects have been removed by combining data from accelerometers, a GPS receiver and gyroscopes onboard that correct for these motions, and also because several anemometers are present. In addition, anemometers are placed in areas that keep them outside plane-induced turbulence. However, those instruments do require calibration which happens only every few years. Regardless, a variety of error correction techniques are used and that leads to the P3 wind measurements having an estimated error of $\pm 0.3m/s$ (Khelif et al., 1999; Masters and Leise, 1993; French et al., 2009), which is small compared to the wind values that will be studied here.

3.2.2 One point and two-point statistics

For the reasons stated earlier, especially the sampling issues, the focus of this analysis is mainly on “two-point” statistics. While the one-point PDF is a distribution of the values of the field variable itself, the two-point increment PDF is the distribution of increments of the field, i.e. differences in the field between two points separated by a given distance.

A one-point Probability Distribution Function (PDF) is the frequency distribution of values of some variable. If x_i is the (discretized) value of some scalar field variable x (e.g. x could be wind speed or potential temperature), then p_i = fraction of instances of x with values between x_i and $x_i + \Delta x$. A PDF is essentially a histogram (and sometimes simply called a “distribution”), but this term will be used when discussing distributions that are statistically robust and have a well-defined form. One point distributions can be difficult to characterize from observations, especially aircraft observations for the reasons cited earlier.

3.2.2.1 Increments

The most general definition of an increment is:

$$\mathcal{I}(\vec{r}; \vec{\Delta s}) \equiv (\vec{v}(\vec{r} + \vec{\Delta s}, t) - \vec{v}(\vec{r}, t)) \cdot \vec{\Delta s} / \Delta s \quad (3.4)$$

where \vec{r} specifies the first measurement and $\vec{\Delta s}$ specifies the vector separation. For one-dimensional P3 data, a one-dimensional increment is used. For the j th measurement and separation distance Δs ,

$$\mathcal{I}(s_j; \Delta s) = (\vec{v}(s_j + \Delta s, t) - \vec{v}(s_j, t)) \cdot \hat{s} \quad (3.5)$$

On a moving platform, spatial increments also imply a time increment; the two measurements are not at the same time. For the smaller scales, this thesis makes a “frozen turbulence” assumption. What is being assumed is that $f(r_1, t_1) - f(r_2, t_2) =_d f(r_1, t_1) - f(r_2, t_1)$ — equivalence in distribution. This is a weaker assumption; it means that the value assumed by the field $f(r_2, t_1)$ belongs to the same statistical population from which $f(r_2, t_2)$ is drawn. This may be a fairly weak assumption since for increments over 10km are separated in time by approximately $10km/135m/s = 80$ sec, but it is important to note that information in the flow is likely to move slower than the typical speed of motion of the P3 (135 m/s).

3.2.2.2 Structure Function

The n th order structure function (SF) is the n th moment of the distribution of increments:

$$\mathcal{S}_n(\Delta s; \vec{v}(\vec{r}, t)) \equiv \langle \mathcal{I}(\vec{r}; \vec{\Delta s})^n \rangle \quad (3.6)$$

For a P3 transect, a 1D sampling, this simplifies to:

$$\mathcal{S}_n(\Delta s, \vec{v}(s_j, t)) = \langle (\mathcal{I}(s_j; \Delta s))^n \rangle \quad (3.7)$$

The “second order” structure function ($n = 2$) is used in the analysis in this chapter.

The second order structure function is sometimes called the “variogram,” especially in geoscience. Similar ideas have been used to characterize scale-dependent variability in turbulent mixing of atmospheric tracers (Sparling and Bacmeister, 2001), cloud structure (Marshak et al., 1997; Davis et al., 1994), cosmic microwave background distribution (Cayón, 2010), agricultural resource economics (Anselin, 2001), and the clustering behaviors of female Elks (Weckerly et al., 2004).

3.2.3 Advantages of Two-Point Statistics

The purpose of two-point statistics is to give information about scales of variability, but they have a number of other advantages. The SF is insensitive to the overall bias in the data (due to the subtraction in the increment). Adding random, uncorrelated noise adds a constant to the SF. Often, increments are more stationary and homogeneous than the raw data values, hence making the two-point statistics less dependent on sampling. Unlike other scale-dependent methods such as the Fourier analysis, missing data is not a crucial problem.

In addition, the structure function has a simple linear relationship with the autocorrelation, as will be proven below. The Fourier transform of the spectral density is the autocorrelation due to the Wiener-Khinchin Theorem (under appropriate assumptions). The structure function is preferable due to its use of subtraction of measurements, which is better for reduction of numerical error than multiplication of measurements (used by the autocorrelation). However, due to the linear relationship between the two, the structure function can still be used to study the spectral density.

In a scaling range, the kinetic energy spectral density follows a power law (Kolmogorov, 1941, 1991, 1962; Frisch, 1995), something that has been observed in many observational and modeling studies (e.g. see review paper Falkovich and Sreenivasen (2006)). When an energy density has a power law $E(k) \propto k^{-p}$, the structure function will follow $\mathcal{S}_2 \propto \Delta s^{p-1}$. Perhaps the most famous of these power laws is the “Kolmogorov 5/3 slope,” from the 3D isotropic, homogeneous, turbulent energy cas-

cade (Kolmogorov, 1941, 1991, 1962; Falkovich and Sreenivasen, 2006), $E(k) \propto k^{-5/3}$ which results in a structure function $\mathcal{S}_2(\Delta s) \propto \Delta s^{2/3}$. That 2/3 slope was based on a variety of approximations which broke down somewhat, but Kraichnan (1968) developed improvements using conservation laws and came up with a very slight correction based on a 2D energy-ensrophy cascade. Turbulence that is 2D isotropic does not have vortex stretching and other complex phenomena that allow for rapid energy transfer between scales. This results in a larger slope of $E(k) \propto k^{-3}$, and hence $\mathcal{S}_2(\Delta s) \propto \Delta s^2$ for 2D turbulence (Kerr, 2002).

Rotating flows cause a preferred direction in the horizontal; tangential and radial wind is clearly different, except at the smallest of scales. This is a breakdown of isotropy; rotational flows are strictly anisotropic. These rotational flows produce an energy spectrum $E(k) \propto k^{-2}$ in the radial direction and hence $\mathcal{S}_2(\Delta s) \propto \Delta s^1$. That gives the same power spectrum as gravity waves. The problem of *spectral ambiguity* occurs: various physical phenomena can have the same spectral energy density power law exponent and hence structure function power law exponent.

There is no expectation that the winds in tropical cyclones will match the predictions of the above theories for 2D or homogeneous, isotropic 3D turbulence, nor rotating, anisotropic turbulence. While there are features in tropical cyclones that are akin to 2D turbulence, such as vortex Rossby waves and related mesovortices, there are features that are not 2D isotropic. For example, the sheets of boundary layer rolls often seen in tropical cyclones are not isotropic and are more typical of 3D turbulence. Misocyclones, tornadoes, long-lived helical hot towers and other such features have significant vertical structure that does not fit the simplicity of 2D tur-

bulence. Even vortex Rossby waves, despite being possible in 2D barotropic models, actually tilt in the vertical and have spatially shifted entrainment, detrainment and vertical motion (Kwon and Frank, 2005, 2008).

However, despite these limitations, this work presented in this chapter does find universality in some statistics of the wind field. That indicates that, while the simplicity of 2D or 3D turbulence does not apply, a more sophisticated theory may describe tropical cyclone turbulence. Hence this chapter only presents the universality (or lack thereof) that is found in the dataset, and suggests ways in which it can be applied to model validation. That model validation will be explored more in a later chapter.

3.2.4 Structure Function and Autocorrelation

As mentioned earlier, the structure function and autocorrelation have a simple linear relationship. The autocorrelation function for 1D data, is defined as:

$$\mathcal{A}_n(\Delta s; \vec{v}(s_j, t)) = \langle (\vec{v}(\vec{r}(s_j), t) \cdot \hat{s}) (\vec{v}(\vec{r}(s_j + \Delta s), t) \cdot \hat{s}) \rangle - \langle (\vec{v}(\vec{r}(s_j), t) \cdot \hat{s}) \rangle^2 \quad (3.8)$$

For brevity, define

$$X \equiv \vec{v}(\vec{r}(s_j), t) \cdot \hat{s} \quad (3.9)$$

and

$$Y \equiv \vec{v}(\vec{r}(s_j + \Delta s), t) \cdot \hat{s} \quad (3.10)$$

Then the structure function can be written as:

$$\mathcal{S}_2 = \langle (Y - X)^2 \rangle = \langle X^2 \rangle + \langle Y^2 \rangle - 2\langle XY \rangle \quad (3.11)$$

If the scale Δs is small compared to the total length sampled then $\langle X^2 \rangle \approx \langle Y^2 \rangle$,

and:

$$\mathcal{S}_2 \approx -2(\langle XY \rangle - \langle X^2 \rangle) \quad (3.12)$$

Under this simplified notation, the autocorrelation is:

$$\mathcal{A} = \langle XY \rangle \quad (3.13)$$

Hence,

$$\mathcal{S}_2 \approx -2(\mathcal{A} - \langle X^2 \rangle) \quad (3.14)$$

Note that the variance $\nu = \langle X^2 \rangle$, so this means:

$$\mathcal{S}_2(s) \approx -2(\mathcal{A}(s) - \nu) \quad (3.15)$$

The variance ν is not scale-dependent, so for a given scale Δs , this equation gives a simple linear relationship between the structure function and autocorrelation.

3.2.5 Correlation Length

The correlation length \mathfrak{L} is a measure of the range over which fluctuations in a field are correlated. It is defined as:

$$\mathfrak{L} = \int_0^\infty \frac{\mathcal{A}(s)}{\mathcal{A}(0)} ds \quad (3.16)$$

Recalling that $\mathcal{A}(0) = \nu$ and substituting the linear relationship with structure function for $\mathcal{A}(s)$:

$$\mathfrak{L} = \int_0^\infty \frac{\nu - \mathcal{S}_2(s)/2}{\nu} ds \quad (3.17)$$

If \mathcal{S}_2 follows a power law up to a *transition length scale* L and is 2ν thereafter, then:

$$\mathcal{S}_2 = \begin{cases} bs^p & s \leq L \\ 2\nu & s \geq L \end{cases} \quad (3.18)$$

and so,

$$\begin{aligned} \mathfrak{L} &= \int_0^L \frac{\nu - \mathcal{S}_2(s)/2}{\nu} ds = \int_0^L 1 - \frac{\mathcal{S}_2(s)}{2\nu} ds = \int_0^L 1 - \frac{bs^p}{2\nu} ds \\ &= s - \frac{bs^{p+1}}{2\nu(p+1)} \Big|_0^L = L \left(1 - \frac{bL^p}{2\nu(p+1)} \right) \end{aligned} \quad (3.19)$$

Because $\mathcal{S}_2(L) = bL^p = 2\nu$,

$$\mathfrak{L} = L \left(1 - \frac{1}{p+1} \right) = \frac{Lp}{p+1} \quad (3.20)$$

Hence, the correlation length \mathfrak{L} can be determined from the structure function transition scale L and the power law exponent p .

3.3 NOAA WP-3D Orion In-Situ Data

The NOAA P3 Orion aircraft have been used for decades in observing hurricanes, especially hurricanes that are expected to produce extreme damage, or hurricanes of special research interest. There are two of these aircraft, affectionately nicknamed “Kermit” and “Piggy” by the hurricane research community, and accompanied by appropriate custom-made decals from Jim Henson himself. These aircraft are outfitted with a wide assortment of observational equipment.

The in-situ wind measurements used in this thesis come from the 1Hz resolution data distributed by the NOAA Hurricane Research Division. The wind measurements made by each P3 come from three different sources: a five-hole gust probe system on the aircraft radome, Rosemont five hole 858Y probes on the fuselage, and a nine-hole Best Aircraft Turbulence gust probe system at the end of a 2m boom in front of the nose. These wind measurements are corrected for the airplane motion using an aircraft Inertial Navigation System (INS). The INS is used to calculate the P3’s velocity, position and orientation at any given time. That system uses the original known location, velocity and orientation of the plane at some original time (typically the runway), and integrates accelerations generated by eight anemometers and two gyroscopes to determine the velocity at later times. This is periodically corrected using GPS location and velocity measurements. (French et al., 2007)

In addition to wind measurements, the aircraft provides temperature (T) and dewpoint temperature (T_d) measurements. Unfortunately, some of the measurements have so-called *wetting errors* that occur when water is blown into the mea-

surement devices by strong updrafts. The dewpoint temperature is then increased and the temperature is decreased. That leads to the in-situ measurements being supersaturated by extreme amounts during and shortly after updrafts. These problems do not however preclude our use of the data as a simple test for whether the air is saturated. In regions where $T_d \geq T$, the air is either saturated, or was recently saturated and the instrument is still recovering. The latter case will only include data a few seconds after the wetting error. Typically that will include regions that are saturated anyway, and even when those regions are not saturated, the total addition to the sampled area will be small. Due to this, $T \leq T_d$ is a reasonable test for whether the plane is in or close to a saturated (nominally cloudy) region.

3.4 Structure Functions

This analysis starts with an application of structure functions to in-situ wind measurements. Horizontal wind is available in all eighteen storms, while vertical wind is available in only fourteen (it was unavailable in the 2009 and 2010 storms, and in some flights in prior storms). This data was subsetted into radial passes and then grouped radial passes into passes at the same altitude, similar time, same sampling rate (airplane ground speed), and by the same aircraft. The winds from these groups of radial passes were then analyzed via the structure function, and was conditioned on saturation when appropriate.

Analysis of structure functions from individual time periods, pressures, storms, etc. is needed to establish universality or analyze effects of different situations. However, it is useful to combine all data into a single structure function to aid analysis, and also to verify that later results thought to be universal combine to a similar structure function when all data is used.

All structure functions are shown in Figure 3.1. Several interesting scaling regimes can be seen, some of which will be examined more closely later. In particular, the vertical wind structure functions, both saturated and unsaturated (brown and red lines), have a $2/3$ slope up to about 1 km, curve, and have a 0 slope after about 5 km. Radial wind, past about 9 km, has a slope of 1 in unsaturated regions (black line). In saturated regions, before about 2 km, radial wind (green line) has a slope of 0.8. Between about 1.5–15 km, the tangential wind has a slope of 2 (dark blue line).

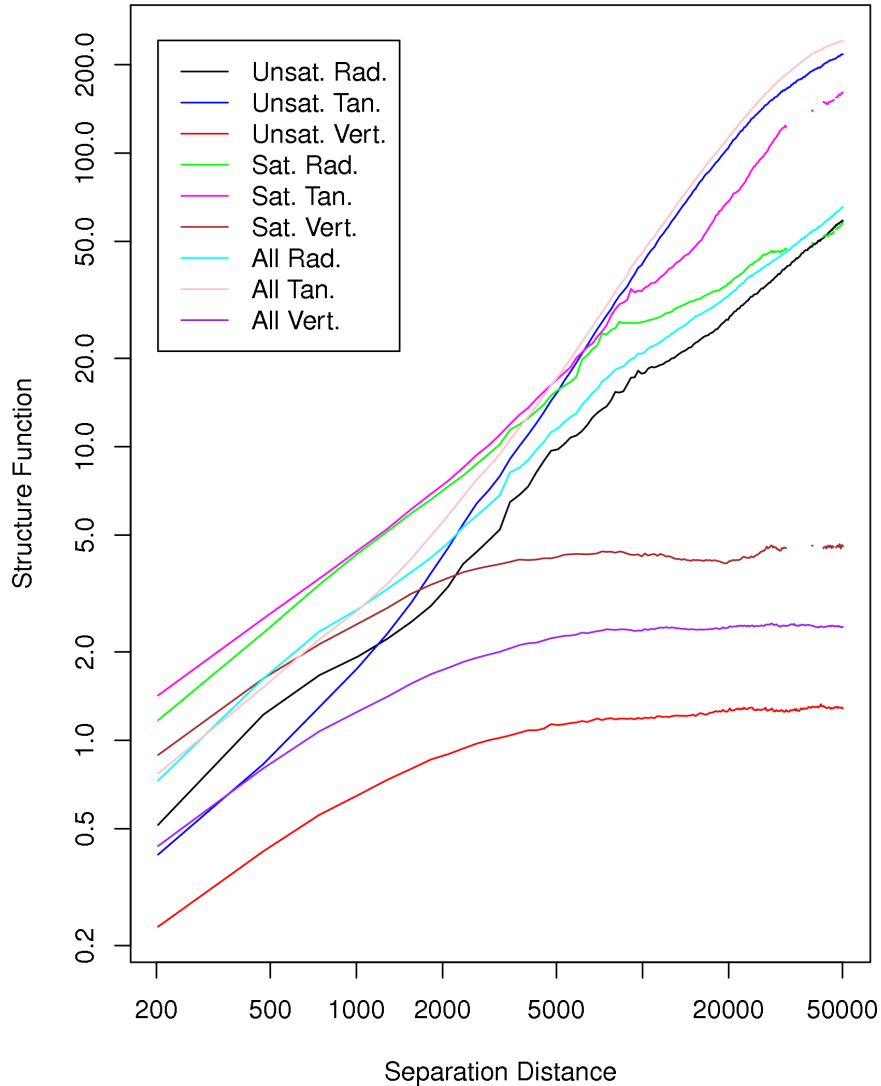


Figure 3.1: Structure functions of all data from all radial passes on a log-log plot.

The radial wind slope of 1 is a very clear slope that spans a wide range of scales. One can see this better on linear axes, seen in Figure 3.2, which again contains all structure functions. This slope of 1, however, is not consistent among multiple storms — for most storms, the structure function of radial wind is very noisy beyond about 15 km. That may be due to undersampling since few 15–50 km scale features are sampled in each hurricane. On the other hand, individual storms

don't have many 15–50 km radial width features in them, so this slope 1 may not be a feature of individual storms, instead it may be something that is only seen when averaging over many storms.

Slopes below 2 km are consistent among all storms and time periods, as will be examined in the remainder of this section. However, it appears that two common forms of turbulence are not at work: the radial wind structure function does not follow $\Delta s^{2/3}$ as would be expected by an upscale energy cascade from the energy injection scale, or Δs^2 , which would be seen from a downscale enstrophy cascade.

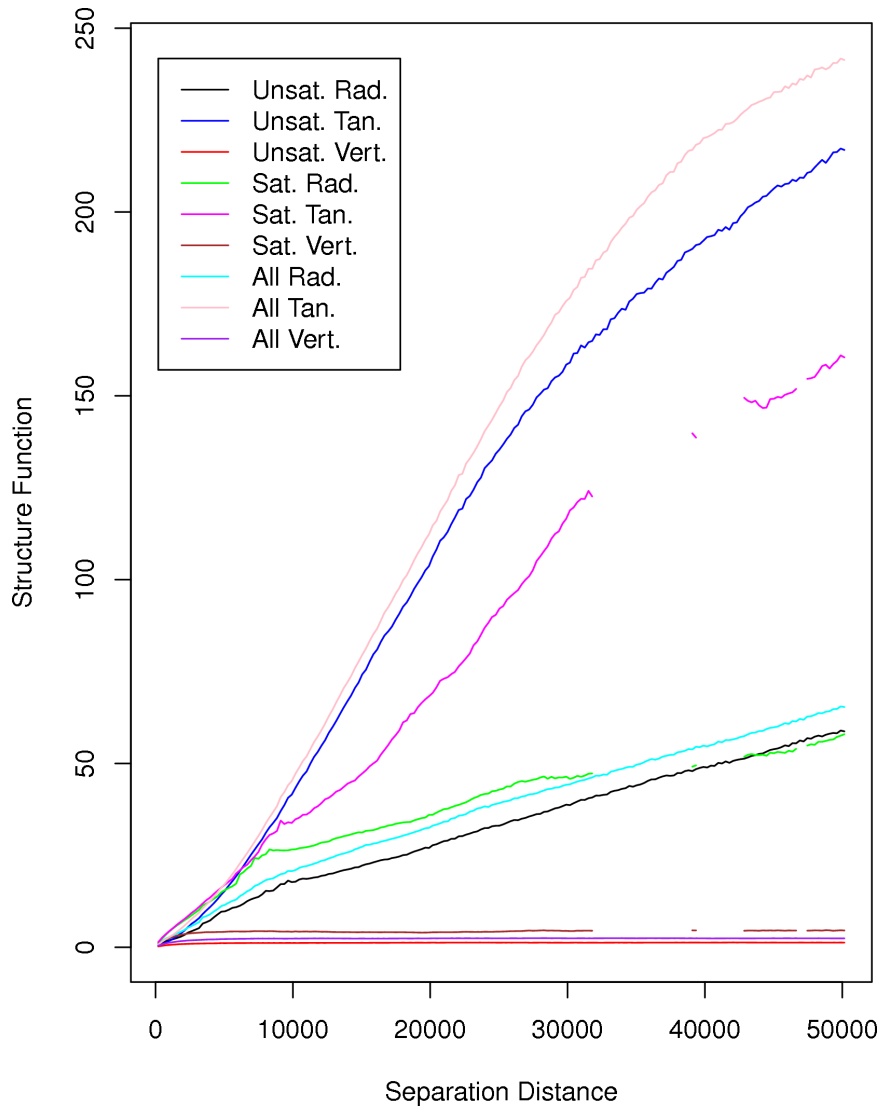


Figure 3.2: Structure functions of all data from all radial passes on a linear plot.

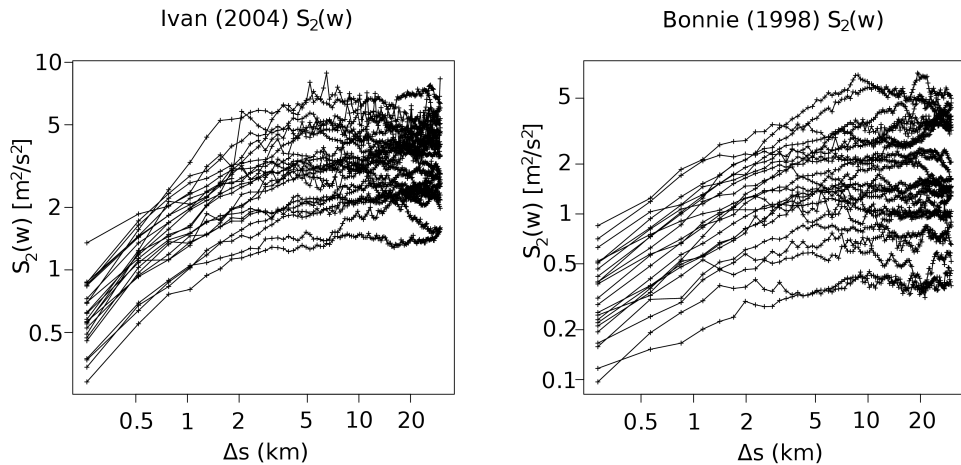


Figure 3.3: Structure functions of vertical wind for all radial passes in Hurricane Ivan (2004) at left, and Bonnie (1998) at right.

3.4.1 Vertical Wind Structure Function

The second-order structure function of scalar field w is defined as:

$$\mathcal{S}_2(\Delta s, w(s_j, t)) = \langle (w(s_j + \Delta s, t) - w(s_j, t))^2 \rangle \quad (3.21)$$

where the quantity in parentheses $(w(s_j + \Delta s, t) - w(s_j, t))$ is the increment of w .

Example structure functions are shown in Figure 3.3a for Hurricane Ivan (2004) and Figure 3.3b where all structure functions for the given storms are over-plotted. These two storms are chosen since they have more available data than any others. In a vast majority of cases, not just for the two storms shown but for all fourteen, the structure function levels off at a scale in the range 1-6 km.

Such a constant p region is seen in most of the structure functions up to

around 1–6 km when the large scale begins to dominate, but the exact p value varies. Recalling that the quantity being analyzed is vertical wind, and that slow rising or subsidence cannot be represented due to the 0.1 m/s precision, this indicates that convective structures have scales 1–6 km. That range can be refined more through the $\mathcal{L} = Lp/(p + 1)$ relation previously derived.

Showing scale invariance requires fairly conclusive evidence. From these simple line plots, it is not clear that there is a scale invariant range from a few hundred meters to a few km in the structure function since curved lines can be seen up to 1–6 km, and only every third structure function bin is plotted to make the plot more readable.

However, the scale r' where p changes can be shown more rigorously through line fits. This thesis will refer to that scale as the *transition scale*. Examples of this is shown in Figure 3.4. For each structure function, scales are divided up into scales somewhat larger and smaller a given scale Δs_i . Then for each possible Δs_i , a line fit is done to all well-sampled scales just less than Δs_i and another line fit to all well-sampled scales just greater than Δs_i . A scale is considered “well-sampled” if there are enough data points such that the scale will have been sampled a minimum of ten times. In the examples, those line fits are shown in yellow, for fits before Δs_i and pink for fits after Δs_i . Data from under-sampled scales is shown with the symbol “+”, while well-sampled scales are indicated with a “+” and a “o”.

The mean absolute variation from the fit is calculated for each line: v_+ for those after Δs_i and v_- for those before Δs_i . The fit that minimizes $v_-i + v_+/i$ is chosen as the final fit. A value of $i = 4$ was chosen to allow the large scale regions to

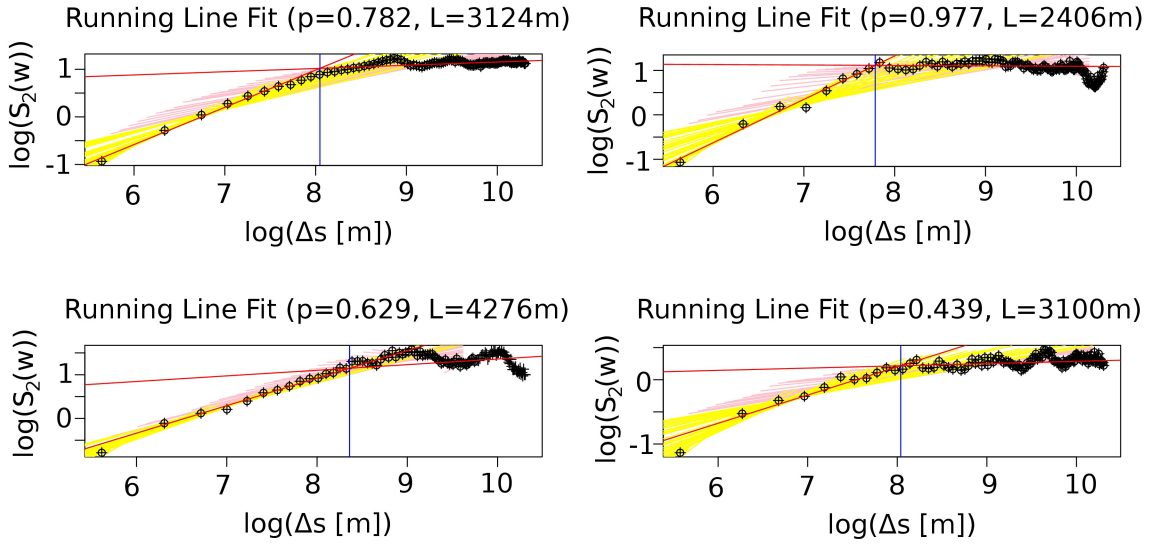


Figure 3.4: Example line fits to vertical wind structure functions.

vary from linear more, since those values tend to be sinusoidal or otherwise noisy. A sinusoidal structure function occurs when a field is periodic with wavelength λ . The first peak will occur at $\lambda/2$, and there will be a peak or trough every $\lambda/2$ thereafter.

A sinusoidal structure function is expected since regular or semi-regular convection cells may occur. After the final fit is chosen, the scale r' at which the two lines intersect is identified. This is shown in the examples with red lines for the final chosen fits, and blue vertical lines at the intersections.

A plot of all transition scales p' are shown in Figure 3.5a. Most of the transition scales lie in the 1–3 km range, with a long tail reaching to larger scales. The correlation length is calculated using the previously derived $Lp/(p+1)$ correction factor, and is shown in Figure 3.5b.

There is a clear and sharp peak at 500 meters, indicating that most of the convection cells are around that size. Furthermore more than 90% of the cases have

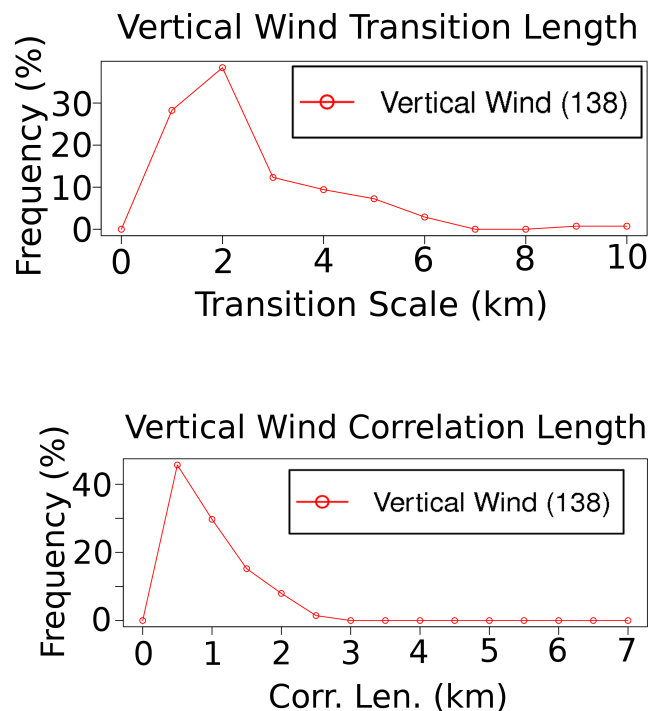


Figure 3.5: Top (3.5a): transition scales from vertical wind structure functions, obtained using the described double line fitting routine. Bottom (3.5b): correlation length, calculated from the power law exponent and transition scale, as derived in Section 3.2.5. Numbers in parentheses are the number of samples.

a correlation length below 3 km.

It is of interest to ask whether this depends on sampling pressure level, storm wind intensity, or storm intensification. Figure 3.6 examines this by conditioning on pressure (above or below 700 mbar), storm wind intensity (category 3 and higher, or below category 3), and two different levels of rapid intensification (RI): a gain of 30 knots in ≤ 24 hrs and a gain of 30 knots in ≤ 36 hrs.

It can be seen that RI induces a curious second peak in the PDF of corre-

lation length (Figures 3.6c and 3.6d), which may be a sign of hot towers forming. Those features are high convective towers that always appear before or during rapid intensification, as will be examined in more detail in Chapters 7 and 8. Due to their high helicity, they are prone to vortex mergers, vortex stretching and other helicity-conservation phenomena. However, regardless of that second peak, the first peak around 500 m is still present in the RI and non-RI cases.

When conditioning on storm intensity and transect pressure level, a widening of the peak at 500m is seen. Stronger storms and higher pressures (lower altitudes, in or near the boundary layer) have a wider with a larger number of cases at 1 km correlation lengths. What is clear though, is that in all cases, the strong peak around 0.5–1 km remains. That suggests that, although hot towers, vortex Rossby wave induced convection, etc. can produce wider convection cells, the vast majority of the area of tropical cyclones is made up of smaller convection.

That result is similar to with what is found in two other large-scale studies that used a different methodology. Both Jorgensen et al. (1985) and Eastin et al. (2005) took NOAA P3 Orion airplane tracks, selected out sequential regions where $w > 0.5$ m/s and called them “updraft cores.” Using that definition of “updraft core,” the Eastin study found that 80% of the cores were less than 3 km in width. The Jorgensen study found about 90%. Unlike the structure function approach taken here, their method of taking an arbitrary cutoff of 0.5 m/s has the disadvantage of ignoring any smaller structures within (such as self-similar structures, or simpler clusters of smaller convection cells). It also is sensitive to instrument noise. However, the fact that the similar result of cores concentrated at large scales is reassuring as

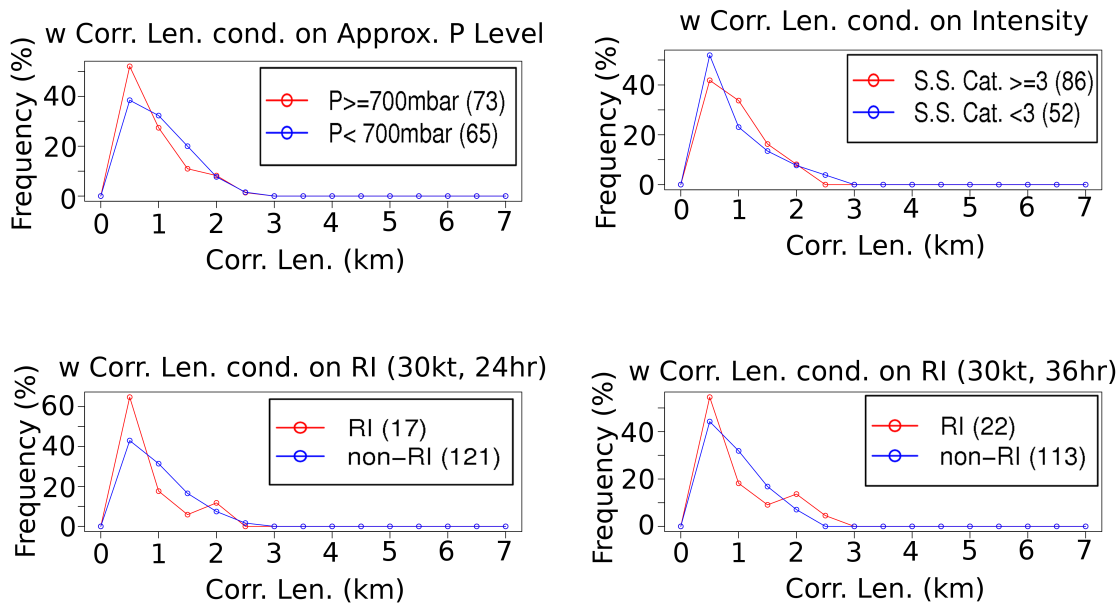


Figure 3.6: Top left (3.6a): PDF of vertical wind correlation length, conditioned on pressure; top right (3.6b): on storm wind intensity; bottom left: on intensification of 30 knots within 24 hrs or less (3.6c); bottom right (3.6d): on intensification of 30 knots within 36 hrs or less. In parentheses are the number of samples.

it is corroborated by this study as well.

What has been consistent among the various conditionings is that there is a strong peak in the PDF of correlation length at 500m, and the vast majority of the correlation lengths are $< 3 \text{ km}$. As one gets farther and farther below the correlation length, the similarity between points separated by ds gets stronger and stronger.

3.4.2 Horizontal Wind Results

While the analysis of the prior section was done for vertical motion, in this section the same analysis is applied to the radial and tangential wind. There are a number of flights for which vertical wind was not available but horizontal wind was, so the statistics in this section are more converged, and a total of eighteen storms have available data.

The precision of horizontal wind is the same as for vertical wind (0.1 m/s), with an error of about 0.3 m/s. However, the typical tropical cyclone horizontal wind speeds are much higher so motions seen are no longer just updrafts and downdrafts. One might expect that small scale horizontal wind perturbations in regions of active convection could be statistically different from those in non-convecting regions due to both convection-induced turbulence (especially on smaller scales) and larger-scale vertical motions inherent in eyewall and rainband structure. For this reason, this section will condition on saturated versus unsaturated conditions. Later, all regions will be analyzed together. However, this section does not analyze the slopes of the structure functions; that will be analyzed in the next section.

Another way to condition the statistics is to form statistical ensembles according to region within the storm. This was tried for five storms: Humberto (2001), Isabel (2003), Katrina (2005), Rita (2005) and Helene (2006) (Trahan et al., 2008). Observations from the P3's side-scanning lower-fuselage radar was used to divide up the storm into eye, eyewall and rainbands. In these, rainband convection and eyewall convection were found to have the same statistical properties as analyzing both

combined. The results for either region are not as well-converged as both regions combined due to under sampling (especially in the eyewall, which is a typically very thin region) and so the combined results are presented.

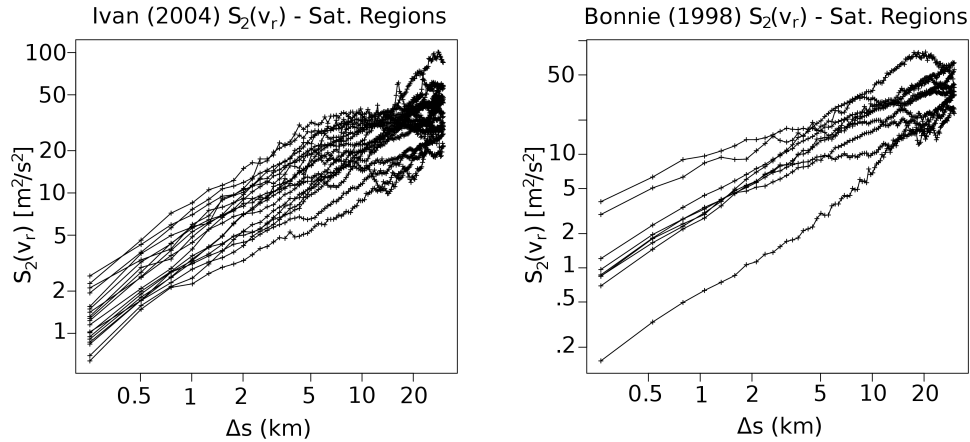


Figure 3.7: Structure functions of radial wind in saturated regions for all radial passes in Hurricane Ivan (2004) and Bonnie (1998).

3.4.3 Saturated Regions

This analysis begins by analyzing the non-eye, saturated regions of the storm. Removal of the eye is critical for this, otherwise the eye vs. non-eye increments dominate the statistics due to their large magnitude. Sample results, again for Bonnie and Ivan, are in Figures 3.7b and 3.7a. A transition scale is sometimes present, but appears to occur at a larger scale than the vertical wind. This is especially true for Bonnie. That is likely caused by inflow associated with Bonnie's multiple rainbands, and deeply convective eye mesovortex.

The exact scale of the correlation length can be found through an analysis identical to that of the vertical wind. The results are shown in Figure 3.8, which shows a histogram of the transition scale in the radial wind, when one exists. Correlation lengths near those of the vertical wind do exist, but many lie at larger

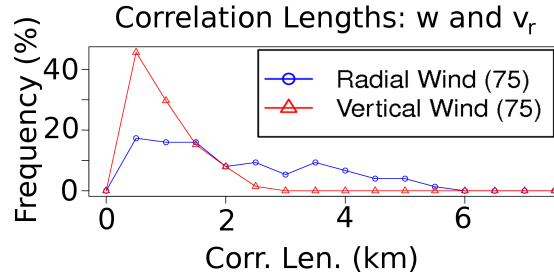


Figure 3.8: Correlation lengths derived from vertical wind and radial wind structure functions, obtained using the previously described double line fitting method and correction factor to the transition scale.

scales.

In addition, some of the cases in Figure 3.7 appear to have two transitions, one near the w correlation length and another transition to steeper slopes at larger scales (nominally, 10-20km) that are likely due to the storm scale secondary circulation. That may be what is causing the correlation length distribution in Figure 3.8.

The presence of a transition scale is to be expected. The updrafts and downdrafts responsible for the similar transition scale in the vertical wind structure function will also have associated convergence from convective entrainment. However, as was discussed in Chapter 2, there are many other effects with associated radial wind, such as the cyclone secondary circulation in smaller storms like Hurricane Karl (2010), mesovortices, and vorticity rolls, which may not necessarily have the same radial regularity.

A manual analysis of radial passes has revealed that the convective entrainment can cover a region significantly larger than the region with upward vertical motion.

In some cases the convergence appears to be caused by several regions of vertical motion acting together. These regions of convection cells acting collectively (such as rainbands and eyewalls) likely contribute to the longer correlation lengths.

The next analysis is of the tangential wind in saturated regions. Figures 3.9b and 3.9a show the same two example cases as before: Bonnie (1998) and Ivan (2004). In these two storms, as well as the other 16 that are not shown, no consistent transition scale is seen — typically there is a near-constant slope across all regions analyzed. This indicates that any convectively-induced vorticity perturbation near most convective cells is small compared to the large-scale vorticity decrease across the cell. Note that this is not an indication of the relative magnitude of convectively-induced vorticity perturbations in hot towers since the P3 is unable to safely sample within those features, so usually tries to avoid them (though sometimes not with complete success).

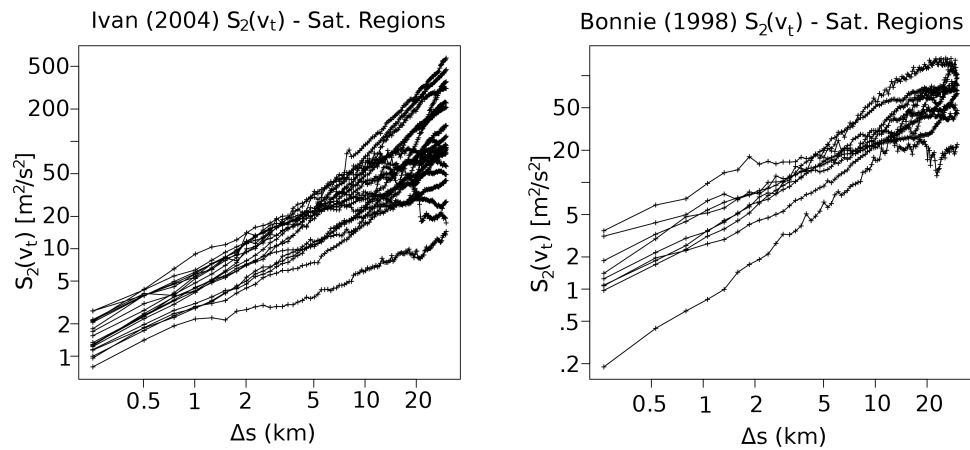


Figure 3.9: Structure functions of tangential wind in saturated regions for all radial passes in Hurricane Ivan (2004) at left and Bonnie (1998) at right.

3.4.4 Unsaturated Regions

The structure function of both radial and tangential wind in unsaturated regions rarely shows any transition scales, and are closer to a power law. Figures 3.10b and 3.10a show structure functions of radial wind in Bonnie (1998) and Ivan (2004), respectively. Transition scales are rarely present, and most structure functions are seen to be fairly linear across a wide range of scales. The corresponding tangential wind is seen in Figures 3.10d and 3.10c, where the results are much the same.

This is not necessarily an expected result since “textbook” hurricanes are thought to be in approximate gradient wind balance, especially away from convection, and balanced winds are not turbulent. However, these results suggest that turbulence exists, even outside of the saturated regions. Inside saturated regions, a clear transition was often seen from a power law to a flatter scaling. This was especially true for vertical wind. That suggests that convection is what is breaking the scaling symmetry. Note, however, that another process, such as boundary layer rolls, may be responsible for the spacing of convection and hence indirectly responsible for the break in scaling symmetry.

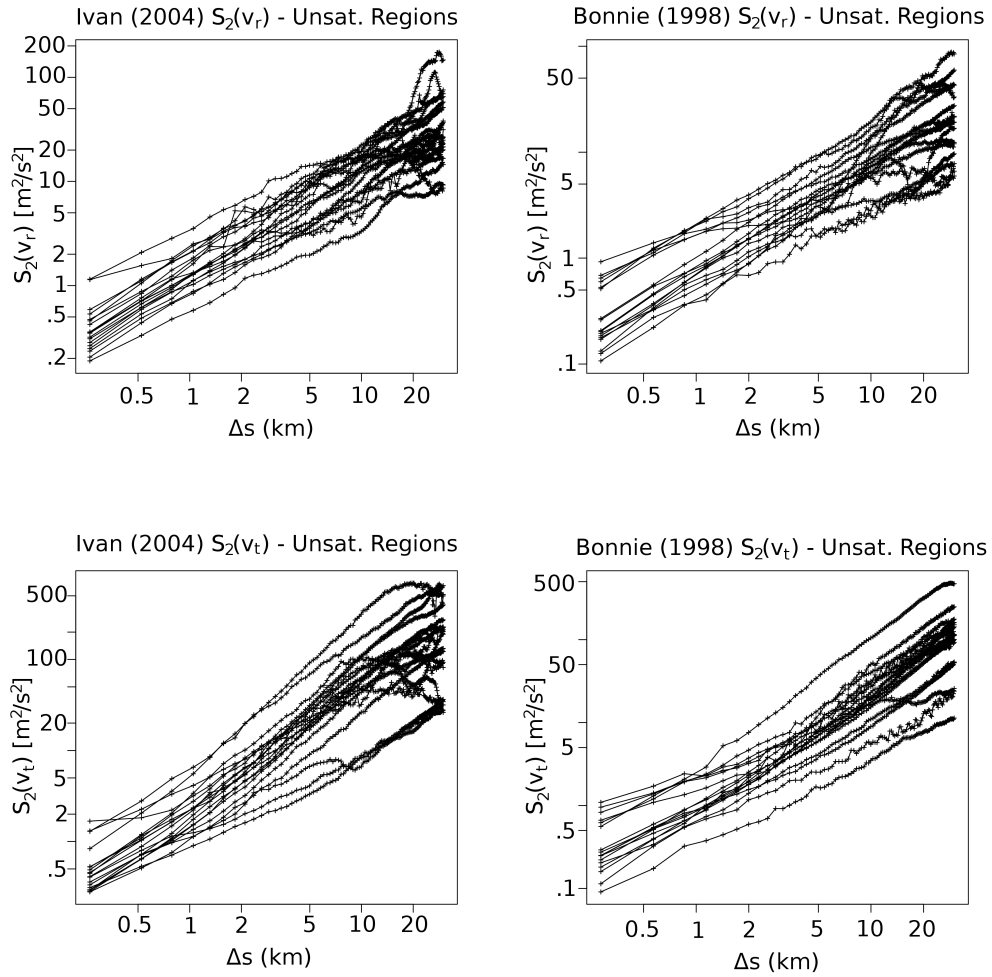


Figure 3.10: Top left and right: structure functions of radial wind in unsaturated regions of Ivan (2004) and Bonnie (1998). Bottom left and right: structure functions of tangential wind in unsaturated regions of Ivan (2004) and Bonnie (1998).

3.4.5 Other Conditioning

When the structure function of radial or tangential wind is computed, without conditioning on anything (ie. use all data from all radial passes), then the results are essentially the same as for structure functions in unsaturated regions. Transition scales are rarely present, and most structure functions have a roughly constant slope across all scales.

3.5 Structure Function Slopes

As discussed earlier in this chapter, the slope of the longitudinal (in the direction of increment) wind has a special meaning in empirical and analytical studies. Specific types of turbulence have specific predicted slopes, so it is of interest to see whether there is a consistent slope seen in structure functions of hurricane in-situ wind in regions where the log-log plots are linear.

Because radial transects are being analyzed, the longitudinal structure function is the structure function of radial wind. Here, several conditionings and processing methods are used. The analysis is repeated with and without detrending of the data, to remove the storm-scale component. The analysis is conditioned on saturation, where convection is present to produce convection-induced turbulence, and unsaturated regions, where the disruptive effects of convection are lessened. Also, an analysis of all radial transect data with no processing is shown.

All of these analyses were performed using a line fit routine similar to the one described previously, but with only one line fit rather than two (no requirement of a transition scale; the entire structure function is allowed to be fit to a line). This resulted in Figure 3.11 which shows that conditioning on saturation or detrending the data makes little difference in the of the slopes. Also, the slopes vary pretty widely, with the half maximum range of around 0.75–1.05.

With a range so large, it is not possible to make any firm conclusions about which of the various analytically predicted phenomena are responsible for hurricane turbulence. However, the $2/3$ slope expected by the 3D turbulent energy-enstrophy

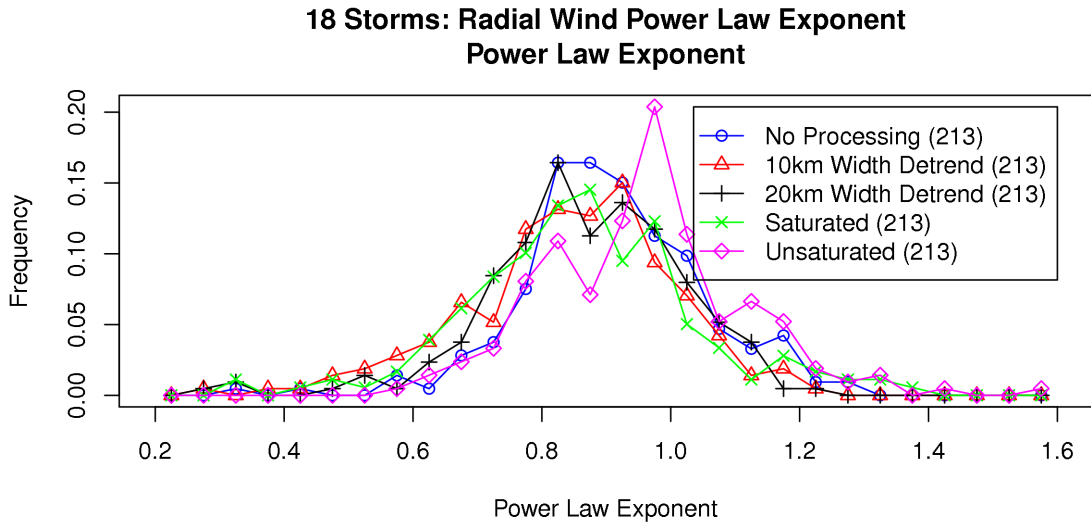


Figure 3.11: PDF of the slopes of radial wind structure functions, with and without conditioning on saturation, and with various (or no) detrending.

cascade is not clearly present, so it is reasonable to conclude that tropical cyclone turbulence is 3D isotropic, homogeneous turbulence. Similarly, 2D turbulence, with its expected slope of 2 (when the upscale enstrophy cascade dominates), is also not plausible. Both gravity wave and anisotropic rotating turbulence, with their expected power law of 1, are possible explanations. Note that the slope is closer to 1 for the unsaturated regions (about 0.95). In unsaturated regions, air tends to be more stable, and gravity waves launched from nearby convection could be present and would contribute to this slope.

HWRF Karl 13I 2010 Vertical Wind vs. Obs

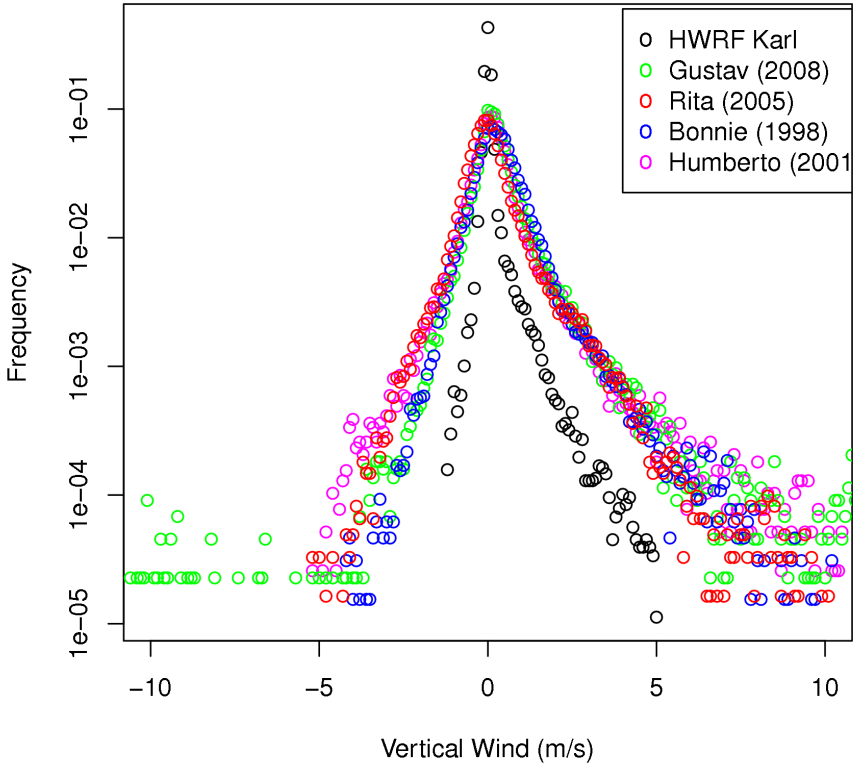


Figure 3.12: Example PDFs of vertical wind values from several storms and a model. Colored PDFs are observations and black is the model.

3.6 Vertical Wind PDF and Normalized Increment PDF

This section examines the vertical wind PDF and PDF of its normalized increments for any universality, or lack thereof.

The vertical wind PDF is shown in Figure 3.12, for four storms with a suitably large amount of samples. In black is results from a model, to be discussed later. It is clear that updrafts have a slightly larger magnitude than downdrafts; the positive tail of the distribution has about twice the magnitude of the negative.

The Gaussian core is likely due to the measurement precision, known to be about ± 0.3 m/s (French et al., 2007). Hence, conclusions about wind speeds around that magnitude cannot be firmly made from this data.

At larger wind speeds, however, there appears to be a similar shape of the PDF between about -2 – 4 m/s. Near-exponential (linear on this semi-log plot) ranges are visible between ± 1.5 m/s. For winds stronger than that, deviations from those two linear regions involve raising above the exponential PDF rather than dropping below, indicating that some minimal level of strong vertical motion is present, with occasional intermittent strong updrafts and downdrafts. Also notice the upward tilt in the PDF at 2 m/s.

One other notable fact is that the mode of the distribution is 0, but the distribution is asymmetric. The area being sampled does not include the outer environment where hurricane outflow induces large-scale downflow. Instead, the P3 samples the inner regions of the storm where the total mass flux is upward. Hence, the mean of the distribution must be non-zero. However, since the mode is zero, this means most of the area is not taking part in the storm-scale upward motion. Instead, a mean upward flow is achieved through having more updrafts than downdrafts, and stronger updrafts than downdrafts. This suggests that the bulk of the upward and downward mass flux is concentrated in small percentage of the area of the storm.

The vertical wind increments as defined earlier are $w(s) - w(s + \Delta s)$ where s is along the path of the plane. However, this section will order the increments by radius r outward from storm center and plot instead $w(r + \Delta r) - w(r)$ so that the sign of the increment now has a physical meaning. Secondly, to more easily compare

multiple scales, the increment PDF will be normalized by dividing by the structure function of scale $\Delta s = \Delta r$. This allows the shapes of the PDF to be compared by correcting for the different magnitudes of the change in w across different scales.

As discussed before, radial passes have been grouped into those of the same storm, and approximate time and pressure and for each group, the increment PDF for several different Δr were calculated. Examples of the normalized w increment PDF are shown in Figures 3.13a and 3.13b.

Consistent among all of the PDFs is that the PDF is symmetric, or close to symmetric, about 0. This means that, although radially inward versus radially outward has a strong physical meaning for tropical cyclone horizontal wind, it has only a weak impact the small-scale structure of the vertical wind. Curiously, this holds from all Δr scales analyzed: approximately 300 m to 6 km. Furthermore, within each group of radial passes, the PDF of any given scale Δr_1 has the same shape as that of any other scale Δr_2 . This indicates that there is some degree of scale invariance in the shape of the PDFs.

This also supports the idea that the vertical wind has an inertial range. A power law scaling was often seen in the vertical wind structure function. Now, the it is clear that the increments are also often self-similar.

However, between different groups of radial passes (different storm, time period or pressure), the PDF of w increments does vary. It typically has a Weibull shape in the tails, with varying exponents, and is Gaussian near the core. The Weibull

distribution is defined as:

$$f(x; \lambda, k) = \begin{cases} \frac{k}{\lambda} \left(\frac{x}{\lambda}\right)^{k-1} e^{-(x/\lambda)^k} & x \geq 0 \\ 0 & x < 0 \end{cases} \quad (3.22)$$

Note that the distribution is only defined for positive x , so one must negate x to fit the negative increments. The cumulative distribution function (CDF, the integral from 0 to infinity of the PDF) is simply $1 - e^{-(x/\lambda)^k}$, again only when $x \geq 0$.

The Gaussian core is expected due to the prior mentioned measurement error. However, sometimes the PDF is Gaussian throughout. Coming back to the prior example PDFs, Figure 3.13a contains a Weibull and Figure 3.13b contains an approximate Gaussian (note the logarithmic Y axis). The tails of these distributions are not always statistically converged, which can cause problems when fitting the Weibull. Unconverged regions (past the first point where a bin has 0 elements) were removed during the fit to avoid that.

Since many of the PDFs are stretched exponentials in the tails, it is worth performing a fit to the stretched exponential (Weibull) distribution in the tails of the distribution. This was done for detrended data (subtracting the X km boxcar averaged values from w before calculating S_2 and increments) and also for the original, non-detrended data. An example fit on the Weibull plot (a plot on which a Weibull distribution shows up as linear) in Figure 3.14a. The Weibull fit was done simply by performing a least squares line fit on the Weibull plot. The CDF for the same example dataset is seen in Figure 3.14b.

Small-scale detrending (up to nominally 5km) does not appreciably change the results, so only the non-detrended results are shown here. The data is then

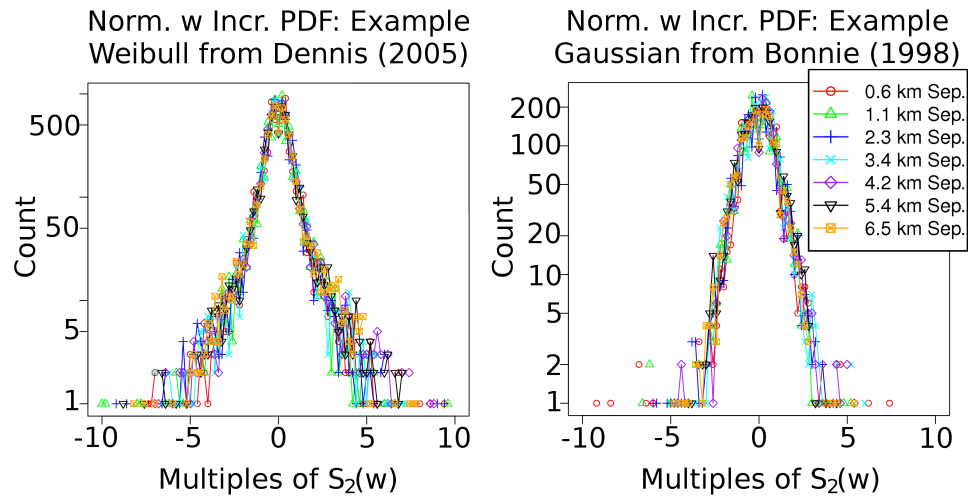


Figure 3.13: Example normalized increment PDFs. Left (3.13a): one with a Gaussian-like core and Weibull-like distribution in the tails. Right (3.13b): one that is Gaussian-like throughout. Note the logarithmic Y axes.

divided into saturated and non-saturated regions and present the results for 3 km increments in Figure 3.15. Fewer k fits are available for saturated regions since less data is saturated than unsaturated. Values for k of 0.85–1.1 dominate the results for both datasets.

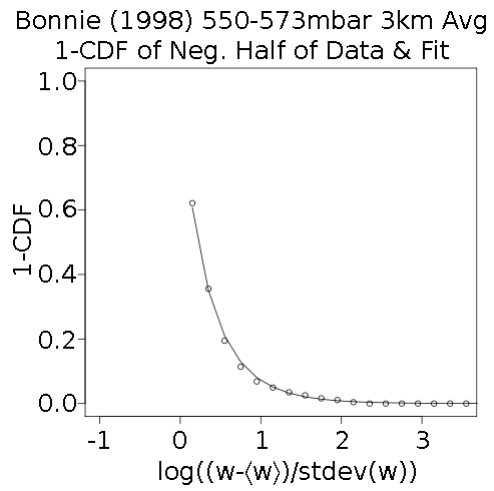
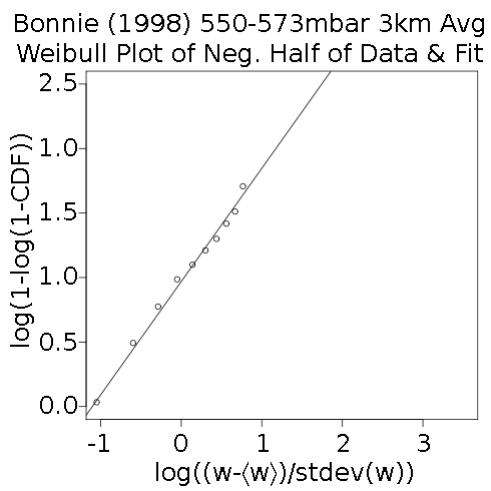


Figure 3.14: Example of a Weibull fit. Left (3.14a): a “Weibull plot”, where axes are chosen such that a Weibull distribution will be linear on that plot. Right (3.14b): the resulting fit to a CDF.

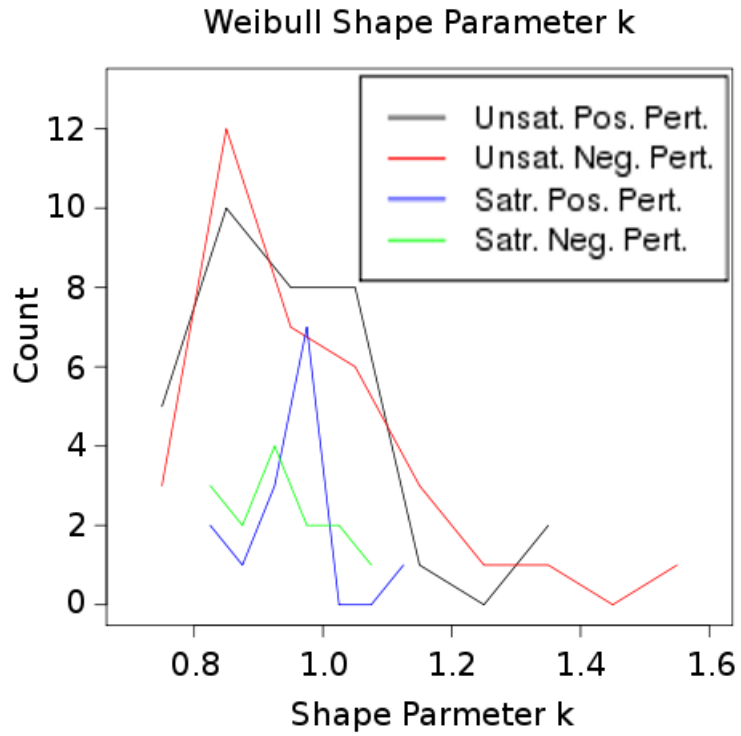


Figure 3.15: Weibull k exponents for normalized w increment PDFs from two different conditionings (saturated and unsaturated) and for the positive and negative half of the PDF.

3.7 Volumetric Vertical Flux

This section performs an analysis of in-situ data from the various P3 flights through 18 North Atlantic tropical cyclones. The analysis begins with the vertical volumetric flux density, a analysis similar to those performed in the past Eastin et al. (eg., see 2005). The volumetric flux Fl_{storm} is calculated using all vertical wind measurements w_j in each region R_i :

$$Fl_{storm} = \frac{\sum_i \pi(dr)^2(i^2 - (i-1)^2) \sum_{j \in R_i} w_j}{\sum_i \pi(dr)^2(i^2 - (i-1)^2)} \quad (3.23)$$

This is essentially an area-weighted average of annuli and a central circle, with the assumption that the measurements within each annulus or circle are representative of the statistics within that circle. Throughout this section, $dr = 10km$.

No density is included in this flux measurement; this is the volumetric flux rather than the mass flux. This is done because two major sources of variation in the P3 density measurement are artificial: variations in the P3's altitude, and wetting errors (Eastin et al., 2005) which cause spikes in the measured temperature when updrafts blow water into the temperature and dewpoint temperature measurement devices. This limitation makes the analysis presented here a measure of vertical motion density, but a poor analogue for mass flux density.

After calculating the fluxes, this analysis selects the region within each storm with the strongest (largest magnitude w) 25% of the upward volumetric flux and the strongest 25% of the downward volumetric flux. Figure 3.16a shows a histogram, including all storms, altitude ranges and time periods, of the percent of the area

within each case taken up by the strongest 25% of the upward volumetric flux. For the bulk of the cases, 3–7% of the storm contains the strongest 25% of the volumetric flux. Figure 3.16b is the corresponding plot for downward flux and shows a typical range of 2–7% of the area taken up by 25% of the downward flux, but with the peak percentage around 3% rather than the 4% in the updrafts.

In general, there are rarely two flights from two different levels at the same time, so a direct comparison of fluxes at different levels for the same storm is not possible. However, with the abundance of data available, it is still possible to make a comparison of the flux at high and low levels across many storms. This is done by dividing the data into measurements above and below 700 mbar. None of the data used is above 450 mbar, and not much is above 550 mbar, so the hurricane outflow layer is not present in any of these cases.

Figure 3.16c shows a histogram of the percent of the area within each case taken up by the strongest 25% of the upward volumetric flux, conditioned on height. The histograms are virtually identical; vertical flux is just as dense above and below 700mbar. This suggests that the updrafts do not expand or contract much in the range of pressures observed: 900 mbar to around 500 mbar. In other words, no significant horizontal expansion or contraction in updrafts is present until at or above the, nominally 500 mbar, steering flow.

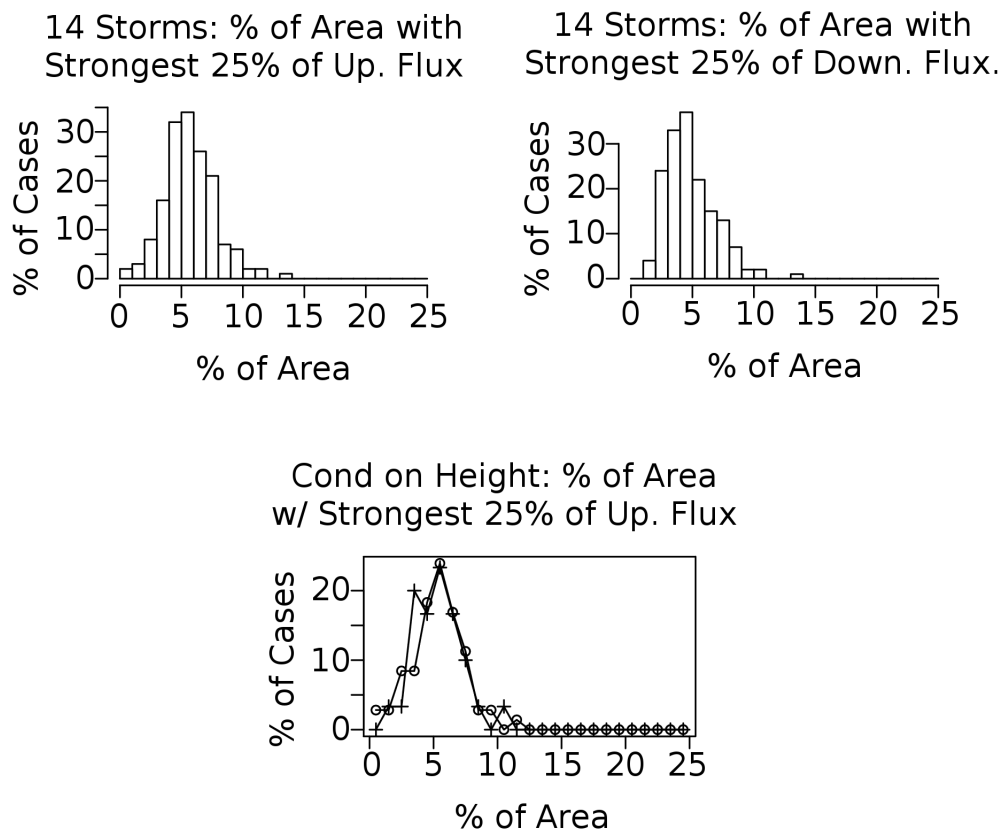


Figure 3.16: Top left (3.16a): histogram of upward volumetric flux concentration in fourteen North Atlantic tropical cyclones. Top right (3.16b): downward flux. Bottom (3.16c): upward flux conditioned on pressure: circles are $P < 700\text{mbar}$ and plusses are $P > 700\text{mbar}$.

3.8 Conclusions

To date, there has been little analysis of scale-dependent variability in tropical cyclones, and this study sought to address that issue. In doing so, a new framework is developed for analyzing scales of motion in tropical cyclones based on two-point statistics. While this analysis was done mainly for the purposes of model diagnostics, it has uncovered a number of aspects of tropical cyclone small scales that are also of importance to other fields of tropical cyclone study.

In particular, a preferred scale of motion is seen in vertical wind with a peak around 2 km in the distribution of transition scales and around 0.5–1 km in correlation lengths. That indicates scales beyond around 2 km have little or no correlation in vertical wind. That peak is independent of intensity, intensification and airplane pressure level, providing a universal statistic that can be used for model diagnostics and design of parameterizations.

Furthermore, the vertical wind normalized increment PDF is scale invariant: within one time period of one storm, the PDF has the same shape regardless of scale, up to a scale of around 6 km. That PDF tends to have a Gaussian core, and typically Weibull tails, but is sometimes Gaussian throughout. It is speculated that the PDFs Gaussian throughout are from times when the plane simply does not fly through strong convection.

Updrafts and downdrafts are seen to be highly concentrated, judging by vertical volumetric mass flux derived from a storm compositing method. The vertical wind one-point PDF provided similar results. Occasional high-velocity upward and

downward motion is seen, but the bulk of the vertical motion is slow, and within about -2-2 m/s, the PDF shape is consistent between storms.

The radial wind was also analyzed, and its structure function had a power law region with $S_2(v_r) \propto \Delta s^p$. Values of p can be used to characterize the type of turbulence present. Fully characterizing that is outside the scope of this thesis, but some conclusions can be made from the distributions of p seen. Various processing methods and conditionings were tried on the radial wind data before determining p . Unsaturated regions had a sharp peak at $p = 0.95$ and half-maximums at around 0.8 and 1.05. All other cases had distribution with half-maximums at 0.75 and 1.05 and a peak around 0.85. From this, it seems unlikely that 3D isotropic downscale energy cascade ($p = 2/3$), 2D upscale energy cascade ($p = 2/3$), or the downscale enstrophy cascade ($p = 2$) are the dynamical regimes present. However, gravity waves ($p = 1$) are likely in unsaturated regions (where p peaked at 0.95), and stratified anisotropic rotating turbulence (p of $2/3$ or 1 : Yeung and Zhou, 1998; Hattori et al., 2004; Mahalov and Zhou, 1996) is possible as well.

The vertical wind analysis raises questions for numerical models whose resolution is near the convection scale. What, though, will happen if one uses scales only slightly larger than the correlation length scale? Is a convection scheme necessary? Will a 3 km model, unassisted by a convection scheme, correctly average over several 1 km downdrafts and updrafts within each 3x3 km grid cell?

If that can be achieved, then one would be resolving the effects of convection, without resolving the convection itself, but without the abrupt, damaging effects of a convection scheme on small-scale structure. The fact that the radial wind

transitions scales, when present, are usually above 3 km suggests that the associated entrainment and detrainment should be resolvable.

The particular analysis methods and scales chosen were chosen due to the fact that they can be applied to models of near-convective scales (around 1–6 km resolution). These and other concepts will be explored in Chapter 8.

Chapter 4

Wind Bias in the Utopian Model

One of the main goals of this thesis is to analyze model-related issues in tropical cyclone intensity forecasting. An inherent assumption in that is that one has a way to classify the intensity of a modeled tropical cyclone. What is used in the real world is the maximum one minute sustained (averaged) ten meter altitude winds, while in models the gridpoint maximum wind is used. This leads to a systematic, resolution-dependent bias. In this chapter, a theoretical construct is introduced: the *Utopian Model*, which is a model whose forecast is the real atmosphere, in a finite difference grid (or a finite element grid, or spectrally-decomposed).

By this definition, the Utopian Model is essentially a coarse-grained version of the real atmosphere. That concept is used to estimate the extent to which the model systematically underestimates the intensity solely due to the area averaging effects inherent in numerical forecasting, even if all other aspects of the model are perfect. This is an issue with the very definition of model predicted intensity as the gridpoint maximum wind.

The organization is as follows. The *Background* section explains this problem more thoroughly. The *Methodology* section describes a method by which one can average and subsample data to obtain the wind bias of the Utopian Model, as its resolution varies. Section *Results and Discussion* presents and discusses the results

of that analysis. The *Conclusions* section explains the implications of these results to modeling and model diagnostics.

4.1 Background

Three common approaches to tropical cyclone forecasting involve numerical modeling: the finite difference method, the finite element method and spectral modeling. In all cases, space and time are discretized. The finite difference method represents space as an orthogonal grid of warped cubes, and calculates fluxes between the cubes by both solving the equations of motion of the atmosphere (*grid scale fluxes*). The finite element method is similar, except that cubes are not required; any mesh of volumes is allowed. Spectral modeling spectrally decomposes the wind, temperature and other fields and numerically solves a set of coupled equations for the time evolution of the mode amplitudes. All numerical models discretize space and time (or limit the number of modes), and have an upper bound on space and time resolution. The field variables are grid scale averages and sub-grid scale processes, for example microphysics or boundary layer turbulent fluxes (*subgrid scale fluxes*), must be parameterized.

The ideal goal of a forecasting model is to predict the real world with 100% accuracy. For a perfect finite difference model, that means each grid cube's temperature contains the actual volume averaged temperature at that exact time in that volume. The area averaged 2 meter altitude temperature at the bottom of each bottom-most grid cube contains the actual area averaged 2 meter altitude tempera-

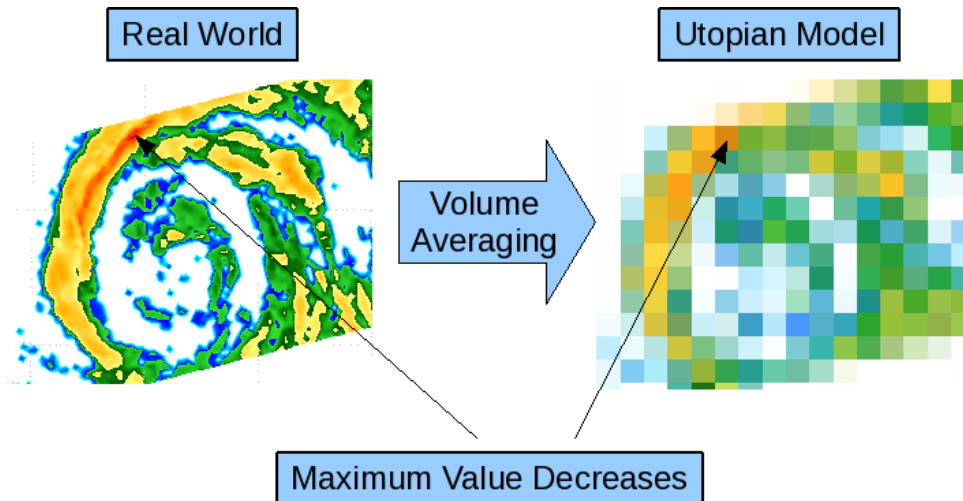


Figure 4.1: The Utopian Forecasting Model is a model that produces a perfect forecast 100% of the time, represented in a finite element or finite difference grid, or in a spectral model. An inherent averaging and subsampling (or spectral truncation) is inherent in that, leading to a drop in maxima.

ture. As a result of that averaging, the maximum value drops. See Figure 4.1 for an example. The same effect happens similarly for a finite element model: volume or area averaged values are computed rather than point values. Spectral models have the same limitation due to the limited number of modes.

The accurate prediction of hurricane intensity is of paramount importance, but is one of the most problematic aspects of hurricane forecasting in the US. One aspect of this problem is the very definition of "intensity" which does not take into account the finite resolution of a forecast model. The National Hurricane Center uses the one minute sustained (averaged) ten meter altitude winds as their definition of hurricane intensity, and evaluates HWRF model intensity forecasts entirely based on that quantity. The official NCEP Hurricane Tracker uses the model instantaneous

gridscale maximum 10 meter wind as the model's predicted intensity (Developmental Testbed Center, 2010).

There are two different sets of averaging between those two measures of ten meter wind. The model wind is temporally averaged over one timestep (a few seconds to a few minutes depending on model resolution), and is spatially averaged over a gridbox (a few km to a few tens of km) or similarly spectrally averaged. The real-world wind is the wind measured by an anemometer, stationary relative to the Earth, over a 60 second time period. This can be viewed equivalently as a linear spatial average in the frame of reference of the moving storm. A typical storm speed is around 5–15 m/s, which means 60 seconds corresponds to a motion of 300–900 meters in the storm's reference. That is effectively a turbulent scale. This is being compared to model winds, which have been averaged over a 2D box around 6–30 km on each side, a scale above the convective scale and in some cases larger than the storm RMW. Comparing model gridpoint scale maximum wind to actual anemometer wind is a comparison of storm-scale wind to turbulent-scale wind.

With an abundance of in-situ wind data from NOAA P3 radial passes of North Atlantic hurricanes, there is an opportunity to analyze the effect of averaging on hurricane wind intensity. In this chapter, the difference between the value of the wind at a point and the average in a surrounding neighborhood (a "gridcell") will be computed from P3 aircraft data. The P3 data are 1D transects, and it is argued below that a 1D average over a scale L is a good approximation to a 2D average over a gridcell of area L^2 . This chapter shows that the differences depend on the size of the neighborhood and implicitly on the intermittency of the small scale fluctuations

in the wind.

The analysis below will be based on averaging along radial segments, which are much more numerous than tangential segments. In addition, tangential flight segments are typically not in high wind regions.

For axially-symmetric storms that are large relative to the model resolution, this should make no difference. The axial symmetry implies that the tangential averaging will make zero impact on the drop of the wind within each grid box. The large size implies that the curvature of the storm will not be significant within the grid box. Hence, for the “textbook hurricane” being simulated by a model that has a sufficiently high resolution to represent it, the radial average is sufficient.

It is for small storms and storms that are highly axially asymmetric that a problem comes up. If the tangential variation within a gridbox is significant, there will be an additional drop beyond what an analysis based on the radial variation would predict. Since tropical cyclones have very strong variations in wind in the radial direction, it seems unlikely that the tangential variation would ever exceed the radial variation. However, it is still possible for the tangential variation to be significant. Such a case would happen, for example, in tropical cyclone genesis cases where the storm is made up of many individual vortices that have not yet formed a coherent storm-scale structure. The use of radial segments may underestimate the resolution sensitivity.

If the radial variation predicts a drop-off of a fraction f_v of the maximum wind, and the tangential wind has as much variability as the radial wind, then the worst variation seen for radial and tangential combined, would be f_v^2 . That is likely

a fairly large overestimate, but is the best that can be done with the available data.

It does give us a range, however: $f_v - f_v^2$.

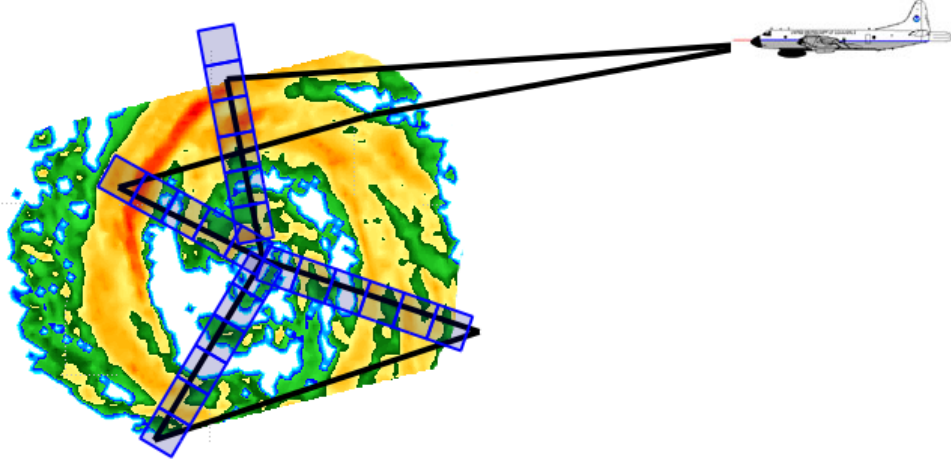


Figure 4.2: Diagram of P3 sampling used to emulate the Utopian Model.

4.2 Methodology

This chapter uses the same NOAA P3 dataset as described in Chapter 3, but divides that data up differently. The data is grouped into six-hour intervals (21Z–3Z, 3Z–9Z, 9Z–15Z and 15Z–21Z) and pressure levels (250–350 mbar, 350–450, 450–550, 550–675, 675–775, 775–875, 875–950, where nearly all data lies between 450–875 mbar). The six hour intervals are chosen to be centered on the forecast cycles used by NCEP (0Z, 6Z, 12Z and 18Z).

The data processing concept is depicted in Figure 4.2. For each group of data (of similar pressure and same time and 6 hr period), and for each desired averaging width Δs , the data is boxcar averaged with width Δs and subsampled at every Δs . This is intended to emulate a finite difference or finite element model of resolution Δs . The maximum of that subsampled and averaged data is then the maximum wind.

What is desired is to determine how much the maximum wind drops relative

to some wind value that is declared the “truth” wind value v_{truth} . Typically, the Best Track wind is used for the “best known intensity,” but is not suitable in this case. The reason is that, if the P3 did not sample the region with the actual wind maximum, then it is not possible to determine the dropoff of the maximum with resolution. Any Δs would result in the wrong maximum. Hence, the “truth” wind must be based on the P3 data. Instead, this chapter uses the reasoning described earlier and subsamples and averages at a distance Δs_{truth} corresponding to the distance an Earth-stationary anemometer would travel in the storm’s reference frame. This can be expressed as:

$$\Delta s_{truth} = v_{storm}(60seconds) \quad (4.1)$$

The resulting wind maximum v_{truth} that comes from the averaging and subsampling is then used as the true maximum wind for comparisons. Various Δs_{truth} values will be explored since the storm motion speed does vary. For this analysis, v_{truth} values of 5 m/s and 10 m/s will be used since they are typical storm motion speeds.

4.3 Results and Discussion

The results of this analysis are shown in Figure 4.3, using the 300 meter averaged winds as the “truth” wind. Note that the dropoff has a non-linear dependence on the truth wind. Also note that the wind drops more for lower resolutions. The resolutions are chosen to more or less match certain NCEP models: the black 38 km is the NCEP GFS model’s resolution until June 2010, while the purple 27 km is the resolution of the upgraded GFS as of late June of 2010, and also is the resolution of the outer domain of the NCEP HWRF forecasting model. Green 9 km corresponds to the current HWRF inner domain resolution, and 3 km is the resolution of the new experimental triple domain HWRF.

Next, it would be useful to compare many resolutions to see if there is a common pattern in the dropoff rate, and for that purpose a single value $f_v(\Delta s, \Delta s_{truth})$ representing the dropoff would be ideal. To obtain that dropoff, first a least squares line fit is obtained to the data for each resolution is performed as shown in Figure 4.3. The intersection of that line with the line of constant $v_{truth} = 85knots$ then produces a value $v_{max}(\Delta s, 85knots)$ for the maximum wind at the model resolution Δs when $v_{truth} = 85knots$. Then, set:

$$f_v(\Delta s, \Delta s_{truth}) = \frac{v_{max}(\Delta s, 85knots)}{85knots} \quad (4.2)$$

where v_{max} must be specified in knots. The value of 85 knots was chosen since it is near the middle of the distribution, where the line fit will be least problematic.

That process was applied to several different resolutions, using various values for Δs_{truth} , and in two different pressure ranges. This results in Figure 4.4, where

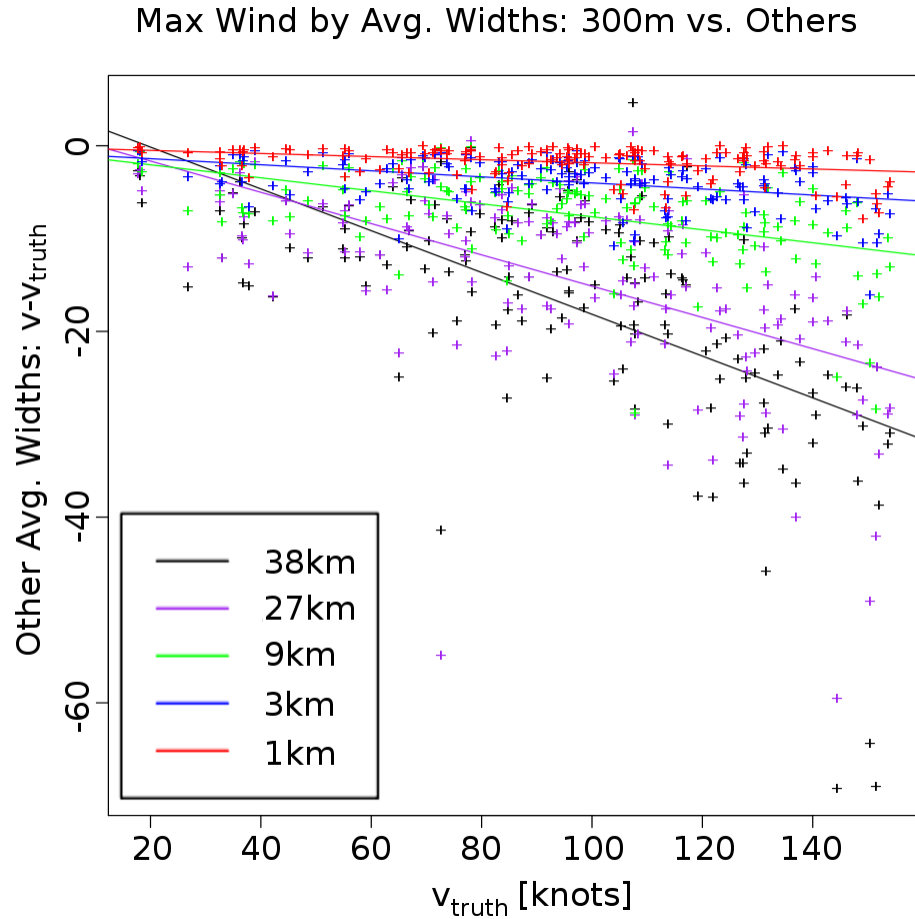


Figure 4.3: Dropoff of the maximum wind of various resolution Utopian Models as compared to the “truth” wind speed from a 300 m averaging.

$100f_v(\dots)$ has been plotted. The Δs_{truth} values of 600 m and 300 m correspond to a storm moving at 10 m/s or 5 m/s, while $\tilde{100}\text{--}150$ m refers to performing no averaging or subsampling (the airplane sampling rate is approximately every 100–150 m). It can be seen that the pressure level chosen makes little difference until very small resolutions, nominally less than 1–3 km. However, the Δs_{truth} chosen still makes a sizeable difference at most resolutions.

If one chooses the 10% level as the maximum acceptable drop in intensity then

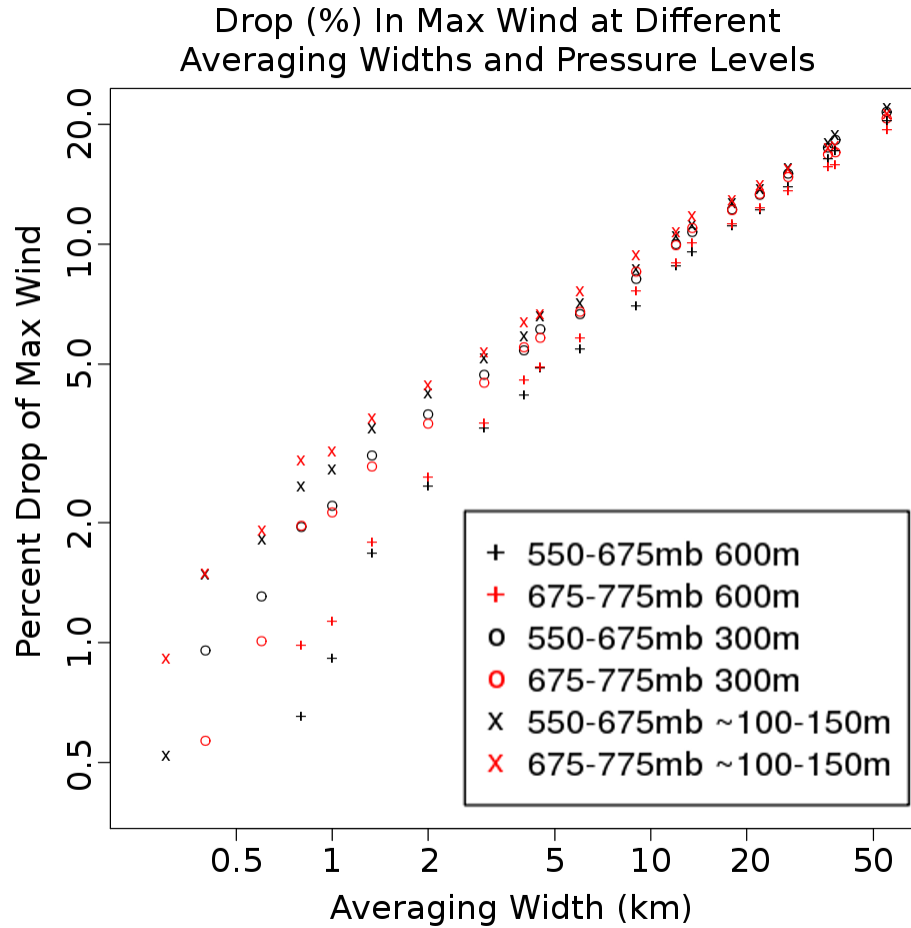


Figure 4.4: Percent dropoff of the maximum wind predicted by Utopian Models of various resolutions, for a storm of “truth” maximum wind of 85 knots.

this means dropping to a resolution of 9 km or better is critical for representing a storm’s maximum. If one chooses the 2% level as a level below which further improvement is not needed, then there is no real improvement to representing intensity beyond about 1 km resolution.

4.4 Conclusions

The definition of tropical cyclone wind intensity is the one minute sustained (averaged) ten meter (anemometer height) altitude winds. However, numerical models, regardless of resolution, use the gridpoint maximum wind as their reported intensity. This ignores the fact that a model predicts a different quantity: the area averaged wind values within each grid box as it varies with time. The gridpoint maximum wind (an area averaging and a temporal averaging) is not the one minute averaged anemometer wind (a temporal averaging). This chapter relates the two quantities, giving a resolution dependent relationship between gridpoint maximum and maximum anemometer wind. It is found that, for a resolution of 1 km, and a storm moving at 5 m/s, there is a dropoff of 2% from the 1 minute sustained 10 meter winds. If one increases to 10 km, that dropoff expands to 10%. This suggests that increasing resolutions beyond 1 km will not gain any significant ability in *resolving* intensity.

This chapter has only taken into account the drop due to radial averaging within model grid boxes, providing a fractional dropoff f_v of the maximum wind, as a function of storm speed and maximum wind. Tangential averaging is not taken into account. For the “textbook hurricane,” an axially symmetric storm that is large compared to the grid scale, the difference would be zero. However, for an asymmetric storm, such as a storm still undergoing genesis, the tangential variation may be significant. For this, an overestimate of f_v^2 is given, meaning that the tangential variation is as large as the radial variation.

The results of this study are a prediction on how the maximum wind *should* drop as grid scale increases. However, it is possible that one could run a low-resolution model and incorrectly “tune” it to produce a maximum wind bias (error relative to the real world maximum) of 0. In doing so, the model would then implicitly have a positive intensity bias.

Lastly, this study only determines the effects on resolving the wind maximum, and does not determine what is needed to resolve the dynamical processes that drive tropical cyclone intensity. Higher resolutions may, or may not, be needed to correctly forecast intensity change. However, being able to resolve the intensity of the storm is a prerequisite to being able to predict it.

Note that the main issue here is actually the representativeness of extreme values, not just in a tropical cyclone, but in any dataset. This work calls into question the wisdom of attempting to predict an extremum, a quantity whose value is resolution-dependent.

Chapter 5

TRMM Satellite Overpass Database

While the P3 in-situ airplane flight-level data examined previously can provide much information about the mid-level winds, it provides no information about what is going on at the top of the storm. The Tropical Rainfall Measurement Mission (TRMM) satellite can be used for that purpose. That satellite contains infrared, visible and microwave passive imagers, an active weather radar and a lightning sensor. However, only the weather radar and the $10.8 \mu m$ infrared band of the imager will be used here.

To analyze cloud tops, a database of TRMM overpasses is required, which must be categorized by storm, basin and other parameters. No database of TRMM overpasses existed as of the writing of this thesis, so one had to be created. This chapter describes how the database was created. Also explained in this chapter is certain properties of the TRMM Precipitation Radar (PR) and Visible and Infrared Scanner (VIRS).

The remainder of this chapter is divided into five sections. Section *TRMM Instruments* provides an explanation of the TRMM PR and VIRS instruments. *TRMM Data Examples* shows examples of the PR and VIRS data and explains some of its limitations in the context of this analysis. Next, *Finding TRMM Tropical Cyclone Overpasses* describes how a database of 2081 overpasses of 827 tropical

cyclones was created. Section *A First Look at the Database: Discussion* performs a manual analysis of rapidly intensifying cyclones and raises questions about what must be examined in a bulk statistical analysis. The chapter then ends with the *Conclusions* section, which summarizes main results.

5.1 TRMM Instruments

The TRMM satellite is a lower earth orbiter at an approximately 34° incline, limiting its view to the tropical regions. (Coincidentally, the tropical regions of Earth are also where tropical cyclones form, so that is not a large limitation here.) Onboard the TRMM satellite are several instruments, including an active radar, a lightning sensor and passive microwave, infrared and visible imagers. Used here are the 13.8 GHz TRMM Precipitation Radar (TRMM PR) and the Visible and Infrared Scanner's (VIRS) channel 4, which images in an approximately $10.8 \mu\text{m}$ band. Weiler (2007)

The TRMM PR swath is approximately 225 km in width before its 2001 orbit boost, and 249 km in width after, due to a higher orbit. It has a vertical resolution of 250 meters and is able to see as high as 20 km with a cloud top sensitivity of 18 dbZ. The limit of 18 dbZ echo tops is a consequence of the design requirements of measuring both the ground reflection and rainfall rates of 0.7 mm/s. Measurement of the echo top was not so much an intended part of the design, but was simply a consequence of the instrument being a radar. The horizontal resolution of the PR was 4.4 km before the orbit boost and 5 km after, both of which are around the upper range of the scale of convection, as previously discussed. The thin 225–249 km swath means that PR data will not be available for the entire storm, except for the very smallest of storms. However, it is generally available for most of the inner core region, out to twice the radius of maximum wind (2 RMW).

The TRMM VIRS channel 4 has twice the resolution of the PR: 2.2 km before

the orbit boost and 2.5 km after. These high resolutions are ideal for this study, which aims to diagnose the near-convective scale resolutions. However, it has a much wider swath of 720 km before boost and 833 km after. The higher resolution places the VIRS measurements near the high-resolution end of the 1–6 km scale of convection discussed in Chapter 3. Unlike the PR, the VIRS does, of course, only provide a 2D swath of data, rather than the full 3D radar field of the PR.

5.2 TRMM Data Examples

The TRMM satellite’s sensors are powerful instruments, but with some limitations. Those issues will be discussed in this section through an example: Hurricane Bonnie (1998), during a TRMM overpass on August 26 at 11:37 UTC.

Bonnie was a well-measured storm, having a NOAA P3 Orion aircraft flying through the storm at the same time as a GOES-8 Rapid Scan Operation and TRMM overpass. The location of the plane at the time of overpass is marked with a red airplane in Figure 5.1b. From nearly simultaneous GOES and VIRS data shown in Figure 5.1a, we can see a large swath of the storm has brightness temperatures around 200K, indicating near-tropopause height convection. The yellow lines in that figure denote the two edges of the TRMM VIRS swath. Note the large size of that swath, encompassing much more than the 2 RMW “inner core” region, and in fact, nearly the entire cloud shield.

In Figure 5.1b, the TRMM 18dbZ echo top height shows a large amount of active convection in the northwest quadrant of the storm extending to around 10km with peaks above 14km. For Bonnie’s latitude and the time of year, this corresponds to approximately tropopause-height convection over large areas of the storm, agreeing with what is seen in the VIRS imagery in Figure 5.1a.

The NOAA P3 Orion aircraft present in this storm at the same time gives us measurements of wind, and hence RMW. In Figure 5.1c, we show the P3 in-situ winds over-plotted on the 2.5km altitude TRMM PR radar reflectivity. The P3 observations through the eye and eyewall indicate that the RMW is about 85 km, in

the middle eyewall region. The official RMW estimate (from the TCVitals database Trahan and Sparling (2011)) was 74 km RMW, which may have included other measurements such as land-based radar. Note that, due to the enormous size of this storm, the swath cuts off some of the 2 RMW region, even if one takes the smaller 74 km estimate.

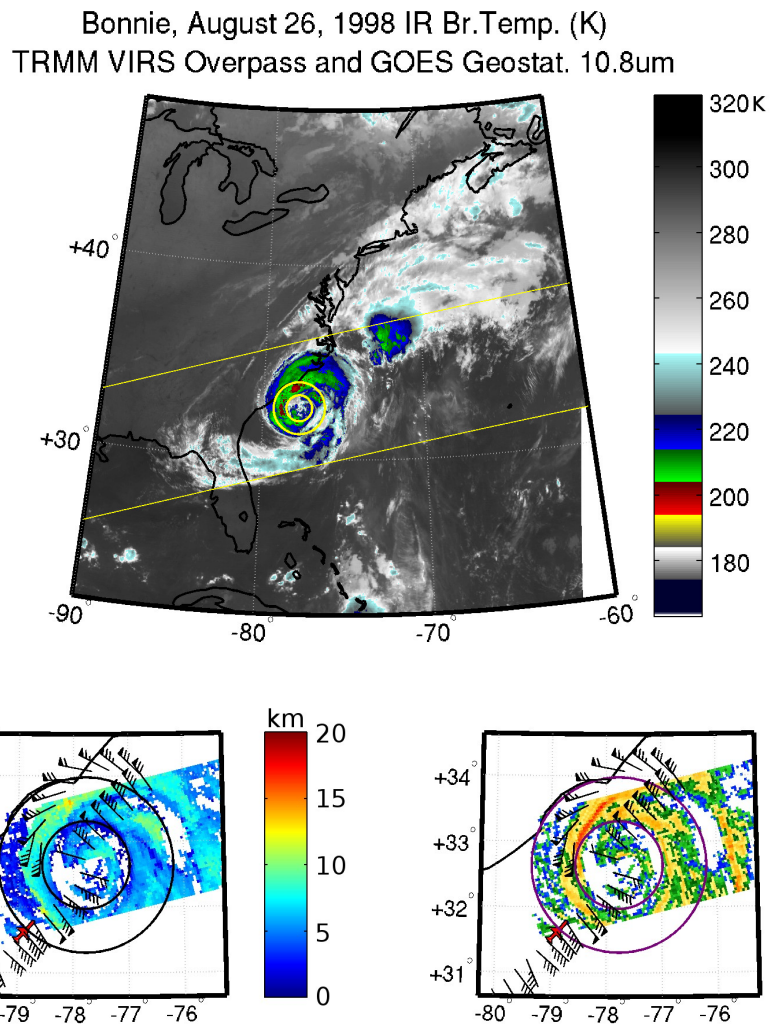


Figure 5.1: Hurricane Bonnie (1998) satellite images from GOES-8, TRMM-VIRS and TRMM-PR with circles plotted at 1 and 2 RMW. Top (a): VIRS 10.8 μ m channel and GOES-8 10.8 μ m channel. Bottom left (b): TRMM 18dbZ echo top height and NOAA P3 Orion in-situ wind measurements (red airplane shows the P3 location during TRMM overpass). Bottom right (c): TRMM 2.5km radar reflectivity (dbZ) with the same P3 wind.

5.3 Finding TRMM Tropical Cyclone Overpasses

In order to perform the comprehensive statistical analysis of TRMM observations presented in this and the next chapter, it was first necessary to create a database of TRMM satellite overpasses as no suitable database was available. The first method that comes to mind would be manually examining every TRMM overpass and finding tropical cyclones. However, that would be a gargantuan undertaking, and largely unnecessary since other organizations have already identified tropical cyclone locations on a regular basis over the past 160 years. Hence, those databases were used in tandem with the TRMM satellite ground point locations over the entire lifetime of the satellite to locate the times and locations of overpasses. In short, this requires three tools: a database of tropical cyclone locations, a database of TRMM satellite locations and a way to compare them efficiently.

5.3.1 NOAA and JTWC Best Track Databases

Two US Government organizations split the duty of maintaining tropical cyclone track information and publicly distributing it. The NOAA National Hurricane Center (NHC) maintains the NOAA Best Track Database, which contains tropical cyclone locations and intensity for tropical cyclones in the Atlantic, North East Pacific and some of the North Central Pacific. The US Navy Joint Typhoon Warning Center (JTWC) maintains track information for the rest of the basins in the JTWC Best Track Database (Chu et al., 2002). It is important to note that the World Meteorological Organization (WMO) divides up the task of basin best track among a larger number of centers, including ones that are part of the Indian, Chinese and other governments, so other track databases exist, possibly with different storm center locations and intensity.

For this analysis, the public NOAA Best Track commonly used by the tropical cyclone research community was not used because it does not contain all numbered storms. In addition, it discards most of the information available about each storm such as the radius of maximum wind, 34 kt, 55 kt and 64 kt wind radii, radius of outermost closed isobar, outermost closed isobar, storm motion vector and others. Instead, the NOAA Best Track database was obtained in its original complete form from internal NOAA sources.

Only numbered storms were used in this study due to two limitations. The pseudo-numbers 90–99, used for non-numbered storms, are reused for multiple storms in the same season, greatly complicating any automatic analysis. Even if a manual

analysis were to be done, the unnumbered Best Track data is usually discarded at the end of the season so such an analysis is not even possible for most years.

5.3.2 TRMM Ephemeris Data

Orbital ephemeris data was obtained from Celestrak, a company that obtains and categorizes many satellites' ephemeris data and provides it through a simple on-line interface. Given the US Government NORAD satellite catalog number (TRMM is 25063), and a timespan, data is provided. This ephemeris data contains such information as satellite location, velocity, estimated acceleration, orbit number and others. Generally, for TRMM, the data was available every 16 hours.

5.3.3 Finding TRMM Crossovers

The Spacetrak4 program is designed to use orbital ephemeris data to determine the future location of a satellite Vallado et al. (2006). It works by taking NORAD two line element sets (ephemeris data), with orbital information, and advecting the satellite around the Earth, taking into account atmospheric drag and various gravity sources.

Modifications were added to allow Spacetrak4 to read the NOAA and JTWC Best Track databases, and a satellite ground point computation was added. Then, for each storm during TRMM's lifetime, this modified Spacetrak4 was run to find overpasses of that storm. All overpasses where Spacetrak4's guess of the TRMM ground point passed within 110 km of the interpolated Best Track storm center were retained.

There were some uncertainties in this method that had to be taken into account. Spacetrak4 program may not do a perfect job of tracking the satellite, the satellite ephemeris data isn't perfect and has finite precision, and the code to compute the satellite ground point may not be exact either. Hence, a second stage was necessary to verify the overpass. For each potential overpass detected by the modified Spacetrak4, the relevant TRMM data was automatically downloaded. Each swath center point has a corresponding time at which the data was observed, and so the storm location from Best Track was interpolated to that time. Hence, for each swath center point, this gave a distance to the interpolated Best Track storm center at that exact time. If the swath center point was within 90 km of the storm

center, the overpass was retained, and all data within 500 km of the center is stored and categorized.

The automated crossover detector was run for all TRMM data from launch through 12:00 UTC on November 6, 2010. This resulted in a database spanning 13 years of TRMM overpasses, including 2081 overpasses of 827 tropical cyclones.

5.4 A First Look at the Database: Discussion

This section presents a manual analysis of one interesting subset of the TRMM database: rapidly intensifying storms. This is, by no means, all that can be done with the database, and Chapter 6 will provide a more rigorous statistical analysis. This manual analysis was done first before a bulk statistical analysis, and was done to open questions about what statistics should be analyzed.

The method by which “rapidly intensifying storms” were selected was straightforward. First, of the entire database, overpasses where radius of maximum wind data was available were analyzed. Among those, the maximum one minute sustained ten meter winds were examined during crossover and for 36 hours after crossover. If at any time, the maximum wind was at least 30 knots higher than at the time of crossover, then the case was declared a rapidly intensifying (RI) storm. This differs from the standard definition of rapid intensification, which is 30 knots in 24 hours. That definition is the approximately 95th percentile over-ocean 24 hr intensification in the 1989–2000 Atlantic Basin tropical cyclones (Kaplan and DeMaria, 2003; Franklin, 2009). This definition was relaxed to 36 hours to allow a larger number of cases, while still retaining a fairly rapid rate of intensification. In total, there are 139 RI cases in this database.

In this detailed case-by-case analysis, one interesting feature was seen: among these rapid intensification cases, even the ones that are well-developed, a vast majority of the storm has echo tops between 6km and 9km, including in the eyewall region. A few cases are seen with large areas of higher convection, but were due to

land interactions or shear. For the most part, cloud tops above 9 km were few, and were either scattered or isolated towers.

One large subset of the RI cases had interesting attributes. Of the 139 cases 69 had an eye clear of convection in radar and an eyewall that is at least 75% closed with at least tropical storm strength (nominally, “well-developed” cyclones). Of those, 67 (all except 2) had at least 50% cloud cover over the eye in IR data, an area that is typically cloud-free in the “textbook hurricane.” Those 67 also had one or more areas of strongly peaked convection along the eyewall with echo tops that are at least 3km above the bulk of the eyewall convection and at least 11km in altitude.

An example of this is shown in Figures 5.2 and 5.3. Figure 5.2 shows the 18 dbZ echo top height, where an eye is clearly visible. The bulk of the 18 dbZ echo top heights are green or the darkest shade of red, the 5–9 km range. Isolated areas of higher convection are seen in the echo top heights. In the infrared data in Figure 5.3, in addition to the usual tropical cyclone cloud shield, the eye is completely covered in low brightness temperatures. For that to happen, either there must be no warm core present, or convective detrainment must be able to overcome any warm core that is present at the detrainment level. These low eye brightness temperatures slope towards higher values (lower altitudes) in the eyewall, suggesting that air is subsiding under these clouds. Any subsidence over the eye will increase the strength of the warm core, possibly explaining the rapid intensification.

This is no great surprise, since it is already known that convective detrainment often dominates the brightness temperatures in the inner core region. Often, during rapid intensification, one or more convective towers will obfuscate the eye, preventing

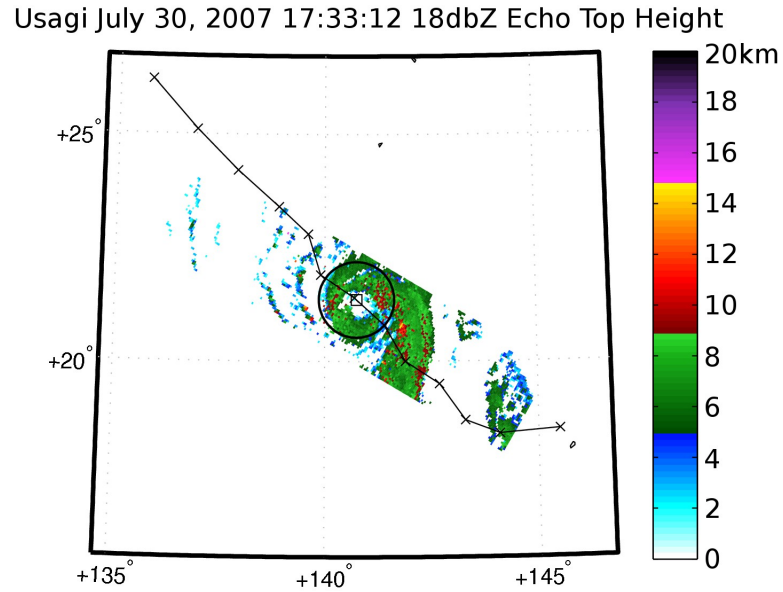


Figure 5.2: TRMM PR 18 dbZ echo top height from Typhoon Usagi (2007) on July 30, 2007 at 17:33:12 UTC. The X marks are 6 hourly JTWC Best Track storm center positions and the square is those positions interpolated to the time of overpass. The circle is the JTWC 2 RMW circle.

one from seeing the mid-level and low-level subsidence, caused by these towers, that is forming or strengthening the eye Heymsfield et al. (2001); Guimond et al. (2010).

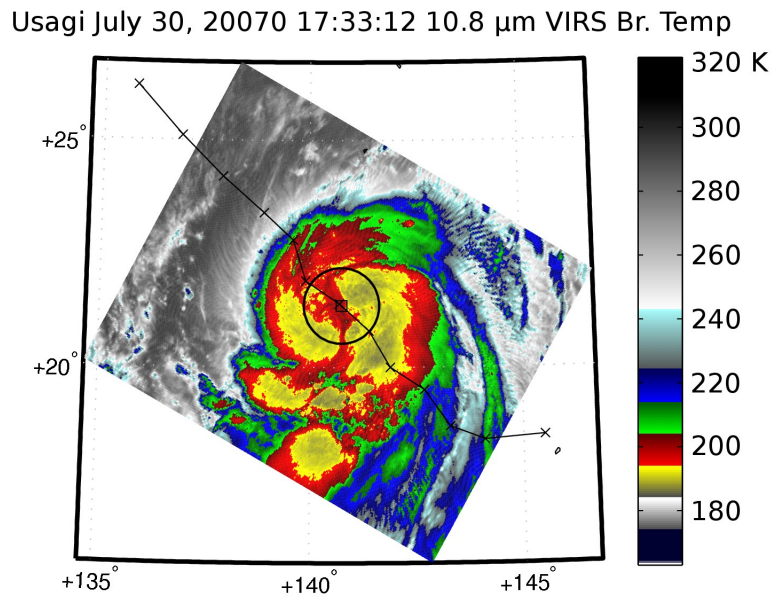


Figure 5.3: TRMM VIRS channel 4, 10.8 μm brightness temperatures from Typhoon Usagi (2007) on July 30, 2007 at 17:33:12 UTC. The X marks are 6 hourly JTWC Best Track storm center positions and the square is those positions interpolated to the time of overpass. The circle is the JTWC 2 RMW circle.

5.5 Conclusions

A categorized database of TRMM crossovers of tropical cyclones was created, and is the only known database of its kind, containing 2081 overpasses of 827 tropical cyclones. Furthermore, the software used to create this database can be easily be extended to additional storms, more TRMM products, or even other polar orbiting satellites, to produce a larger database. This database has potential value far beyond what it is used for in this thesis and will be a useful resource for hurricane researchers. It was used to perform a simple manual analysis on 139 rapidly intensifying cases. Several interesting observations have been made subjectively, and the next chapter will examine whether they hold up in an objective analysis of the entire database. Nearly all active 18 dbZ echo tops from the PR were between 5–9 km, suggesting that stratiform precipitation and low convection is dominant, with isolated areas of strong convection, a point that is supported by results in Chapter 3. Also, in about half of the cases analyzed, areas of isolated or asymmetric high peak 18 dbZ echo top were seen to be under vast clouds of high-altitude (low temperature) detrainment in the $10.8 \mu\text{m}$ VIRS data. This detrainment was seen over a complete or nearly ($> 75\%$) complete eye in 67 of the 139 cases, suggesting that subsidence forced by convective detrainment was contributing to the RI.

The next chapter will perform a bulk statistical analysis of the TRMM database to see if these and other facts hold true in the entire dataset. A comparison of RI versus non-RI will be given, as well as statistics conditioned on intensity.

Chapter 6

TRMM Statistical Analysis

The previous chapter presented a TRMM database of 2081 overpasses of 827 tropical cyclones, created using an automated TRMM tropical cyclone detection program. A simple manual analysis of 139 rapidly-intensifying (RI) cases was performed, where RI was defined as a gain of 30 knots or more within 36 hours of the time of overpass. It was found that in many of these storms, there was isolated or asymmetric high convection with outflow over the eye, a phenomenon that may conceivably cause intensification through eye subsidence forcing warming of the storm's warm core. Most of the radar 18 dbZ echo tops were between 5–9 km.

Do these subjective assessments hold up in an objective analysis of the entire dataset? Are there any relationships between cloud tops, and tropical cyclone intensity or intensification?

Others have already answered those questions with analytical studies or small observational studies of a few storms. In particular, the axially-symmetric theory of intensity, WISHE theory 2.7, suggests a relationship between cloud top and tropical cyclone intensity (subject to convective efficiency). Many studies have shown that hot towers appear before or during intensification (eg., see Guimond et al., 2010; Zipser, 2003; Kelley et al., 2005).

However, this chapter will examine a much larger number of tropical cyclones

than past studies, to answer these questions more rigorously. In doing so, this chapter develops a new framework for analyzing this large database.

The organization of this chapter is divided into three sections. *Methodology* describes the new framework for analyzing the database. *Results* analyzes radar and infrared cloud tops as they relate to intensity and intensification. *Discussion* discusses the implications of this research.

6.1 Methodology

The goal of this methodology is to relate a given statistic about tropical cyclone intensity or intensification, to a given statistic about cloud tops. For the most part, these are the two cloud top quantities that will be analyzed. For each storm,

- for a given threshold temperature, the percentage of the storm area within $2RMW$ that has a TRMM VIRS $10.8 \mu m$ brightness temperature below that threshold.
- for a given threshold altitude, the percentage of the storm area with active radar signatures within $2RMW$ with an 18 dbZ echo top height above that threshold.

This analysis requires determining the percentage of the storm area that has a prescribed value of a given quantity. This in turn requires a clear definition of storm area and that sampling issues be addressed. What is required is a measure of the radius of maximum wind, and a method to account for the areas within $2RMW$ that lie outside the swath.

For each TRMM overpass, the NHC or JTWC Best Track database values for the storm latitude, longitude and maximum one minute sustained ten meter wind are interpolated to to the time of the overpass. This is also done with the RMW, using the RMW from the Best Track when available. When the Best Track RMW is unavailable, the TCVitals RMW is used instead. Among the TRMM overpasses in this study, 1494 have both VIRS and PR data available and an RWM from TCVitals or Best Track.

This analysis will be restricted to regions within $2RMW$ of the storm center. In some cases, the PR sampling will contain only a fraction of the $2RMW$ area. Any analysis of the PDFs of the PR measurements would overly weight well-sampled regions if no correction is made. For that reason, a storm compositing method is used, which divides the storm into concentric annuli of radius dr with a circle of radius dr at the center. Within each annulus or circle, if a sufficient number of measurements are present, then the measurements in that region are assumed to be a well-sampled representation of the entire region. Then, given a condition C , the fraction F_i of measurements that meet condition C within each region R_i is calculated. The fraction of the area of the storm that meets condition C is then an area-weighted average:

$$F_{storm} = \frac{\sum_i \pi dr^2 (i^2 - (i-1)^2) F_i}{\sum_i \pi dr^2 (i^2 - (i-1)^2)} \quad (6.1)$$

This method is also applied to the VIRS data, in the rare instances when the storm $2RMW$ region lies partially outside the VIRS 700km swath.

6.2 Results

The analysis begins with the distribution of the median $10.8 \mu\text{m}$ brightness temperatures, conditioned on intensity. For intensity, the Saffir-Simpson (SS) category is used. That scale is typically used only for North Atlantic, and East and Central Pacific basin tropical cyclones, but here is applied worldwide.

Figure 6.1a shows the distribution of median $10.8 \mu\text{m}$ brightness temperature, conditioned on intensity. The strongest storms, SS category 4 and 5, have a median brightness temperature within 2 RMW that is near the nominal tropopause temperature. Lower SS categories have distributions peaking at lower and lower brightness temperatures, with distributions getting steadily wider. The weakest storms, ones that have not reached SS category 1 yet, have a nearly flat distribution that even includes values near the ocean temperature.

This is, to some extent, expected as there are more ways in which a storm can be weak than strong. Despite the variety of interesting features in category 3 and higher storms, nearly all of them involve high clouds and a semi-coherent storm-scale vortex. On the other hand, weak storms below category 1 can be several scattered vortices slowly merging, or a large region of stratiform precipitation, an ex-Hurricane over a Mexican mountain range, or a sheared vortex, or any number of other things.

The distribution of median 18dbZ echo top height, again conditioned on intensity, is plotted in Figure 6.1b. The distribution is again narrower for the strongest storms. Unlike the brightness temperature distribution, the peak of the distribution

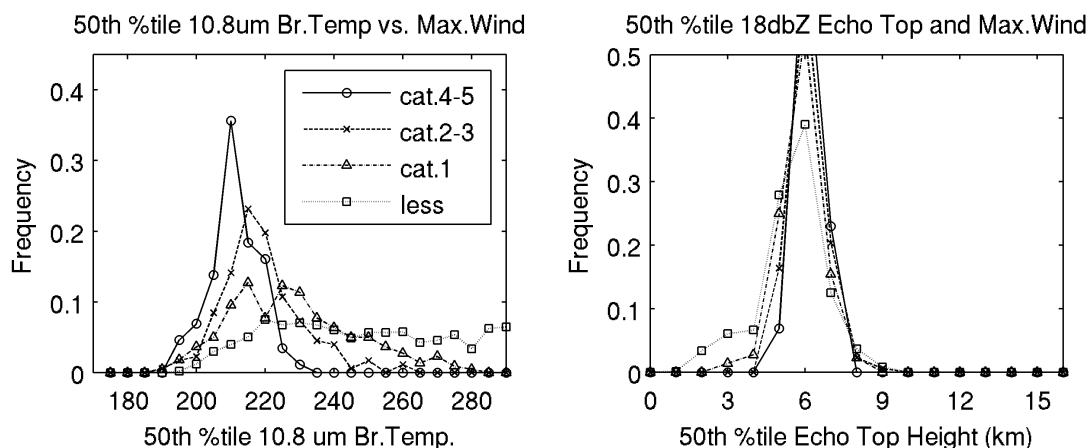


Figure 6.1: PDF of median TRMM VIRS 10.8 μm channel brightness temperature and 18dbZ echo top height, conditioned on tropical storm intensity. Intensity categories are the Saffir-Simpson scale.

is nearly the same (at 6km) for all storm intensities. Given the strong relationship between intensity and 10.8 μm VIRS brightness temperature, this suggests a difference in the hydrometeor distribution in the upper levels, above the melting level (nominally, 5 km), too weak to be detected by a radar with a sensitivity of only 18 dbZ for cloud tops.

In addition, of the TRMM overpasses with PR data (1544 overpasses of 673 storms), in 95% of the overpasses, 80% of the area in $2RMW$ with active radar returns has echo tops <9 km, and in 81% of cases, 90% of the area in $2RMW$ with active radar returns has echo tops <9 km. This suggests that stratiform precipitation and low-altitude convection is dominant in tropical cyclones, and that any upward mass flux is either highly concentrated, or contains only very small or very few hydrometeors. That corresponds well to what was found in an earlier chapter from

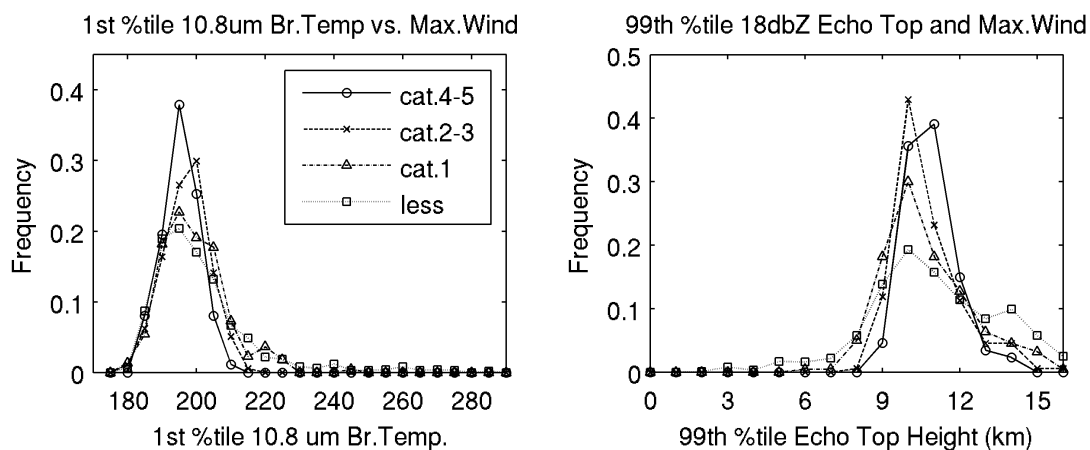


Figure 6.2: PDF of 1st percentile TRMM VIRS 10.8 μm channel brightness temperature and 99th percentile TRMM PR 18dbZ echo top height, conditioned on tropical storm intensity. Intensity categories are the Saffir-Simpson scale.

P3 measurements: a disproportionate amount of the upward volumetric mass flux comes from highly-concentrated areas of strong vertical motion (also found by others using P3 data (Jorgensen et al., 1985; Eastin et al., 2005)).

If wind-induced surface heat exchange is all that is determining the total “fuel” for convection, then the 1st percentile brightness temperature should be dependent on the intensity as well. Figure 6.2a shows the 1st percentile brightness temperature, conditioned on intensity. For completeness, Figure 6.2b shows the 99th percentile 18 dbZ echo top height conditioned on intensity. Neither appears to have any significant relationship with intensity. This is expected of the radar data, where the median also had no relationship with intensity. However, the brightness temperature result has a bit more meaning: it indicates that any storm, regardless of wind speed, is able to produce high localized convection.

It is also interesting that values lower than 190 K are never found in the median 10.8 μm brightness temperature (Figure 6.1a). Individual 1st percentile values as low as 180 μm are sometimes seen, as shown in Figure 6.2a. Rare values below 180 μm are also present, though not easily seen in the plot due to their extreme rarity. (Typhoon Mitag/Mira in 2007 is one such case.) This suggests that more buoyant air and less dilute updrafts can happen, and can produce penetrative convection. However, from the median brightness temperature reaching no lower than 190 K, it seems that storm-scale convective detrainment is limited by the synoptic-scale tropopause, which rarely has a temperature significantly below 190 K even in the tropics.

Another matter of interest is rapid intensification (RI) of tropical cyclones. Typically, the threshold for rapid intensification is defined as a gain of more than 30 knots in 24 hours. That is the 95th percentile 24 hr increase observed in the 1989–2000 Atlantic tropical cyclones (Kaplan and DeMaria, 2003; Franklin, 2009). As discussed in the previous chapter, this is relaxed here to 30 knots in 36 hours to allow a large TRMM sample set. In total, there are 139 cases in this database where the intensity is at least 30 knots higher within 36 hours after the overpass. Figure 6.3a shows the PDF of the 1st percentile TRMM VIRS 10.8 μm brightness temperature, conditioned on RI vs. non-RI cases. The RI cases always have 1st percentile brightness temperatures of 205K or lower, with nearly all below 200K, whereas only half of the non-RI cases lie below that threshold.

The radar echo tops do not have as much of a relationship to intensity, as seen in Figure 6.3b. An examination of other radars suggests why this is so. An example

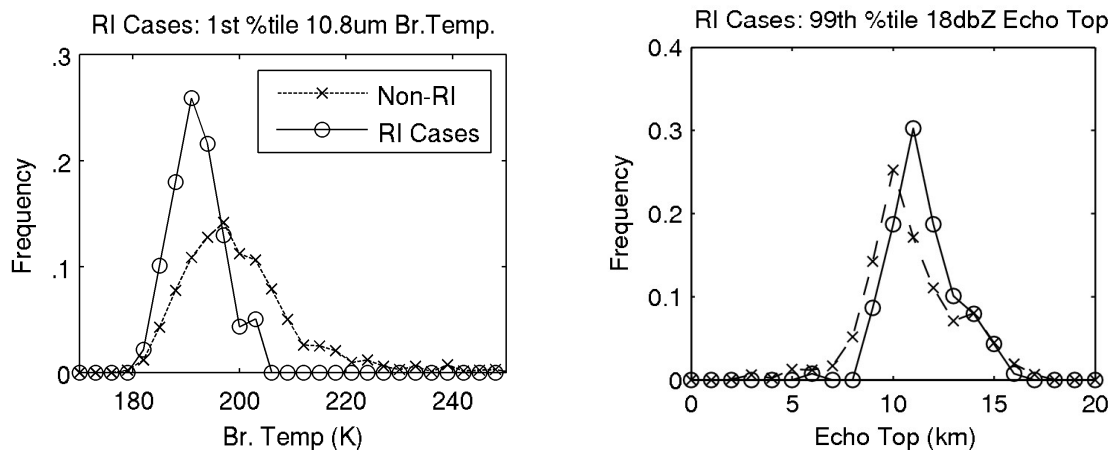


Figure 6.3: PDF of 1st percentile TRMM VIRS $10.8\mu m$ channel brightness temperature and 99th percentile TRMM PR 18 dbZ echo top height, conditioned on RI vs. non-RI cases.

TRMM radar swath is shown in Figure 6.4, where it is clear that the radar echos are cut off at 18 dbZ. The more sensitive (but rarely available) ER-2 EDOP radar is shown in Figure 6.5 and yet more sensitive CloudSat in Figure 6.6. In both cases, it is clear that the regions with high clouds extend significantly beyond 18dbZ. That is likely the reason that the difference between RI and non-RI 99th percentile radar echo top is weak.

There is an important issue to consider here: deep moist convection, regardless of intensity or driving force, has a lifecycle to it. Once the “fuel” to the convection is used up, the convection dissipates temporarily (Halverson, 2011). If TRMM samples during the lulls between convective bursts, then the brightness temperatures will be temporarily high, despite any the powerful convection or rapid intensification. This is something that is clearly seen in any GOES $10.8\mu m$ rapid scan of a highly

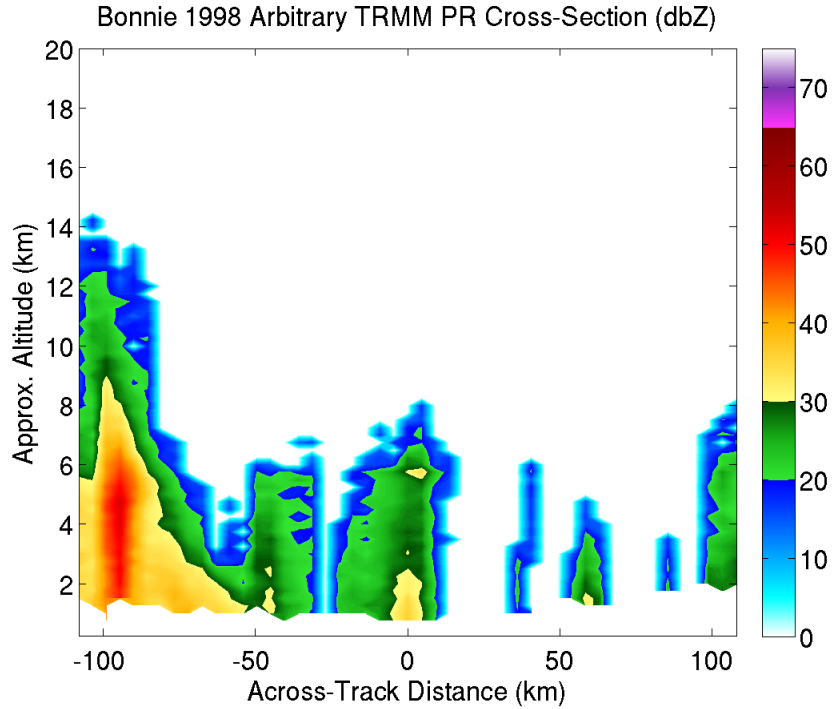


Figure 6.4: Example TRMM precipitation radar cross-section. Note that the reflectivity tops are cut off at 18 dbZ.

convective tropical cyclone, which unfortunately cannot be placed in a printed thesis. However, this “lull” effect is apparently small enough so that a significant difference between RI and non-RI storms is clear, and also such that all storm intensities are able to produce near-tropopause 1st percentile brightness temperatures.

6.3 Discussion

Prior studies have shown a relationship between rapid intensification (RI) and hot towers. In addition, it is known that all storms, regardless of wind speed, are able to produce isolated areas of near-tropopause convection. However, storm-scale outflow height is predicted by axially-symmetric theories to be dependent on storm-

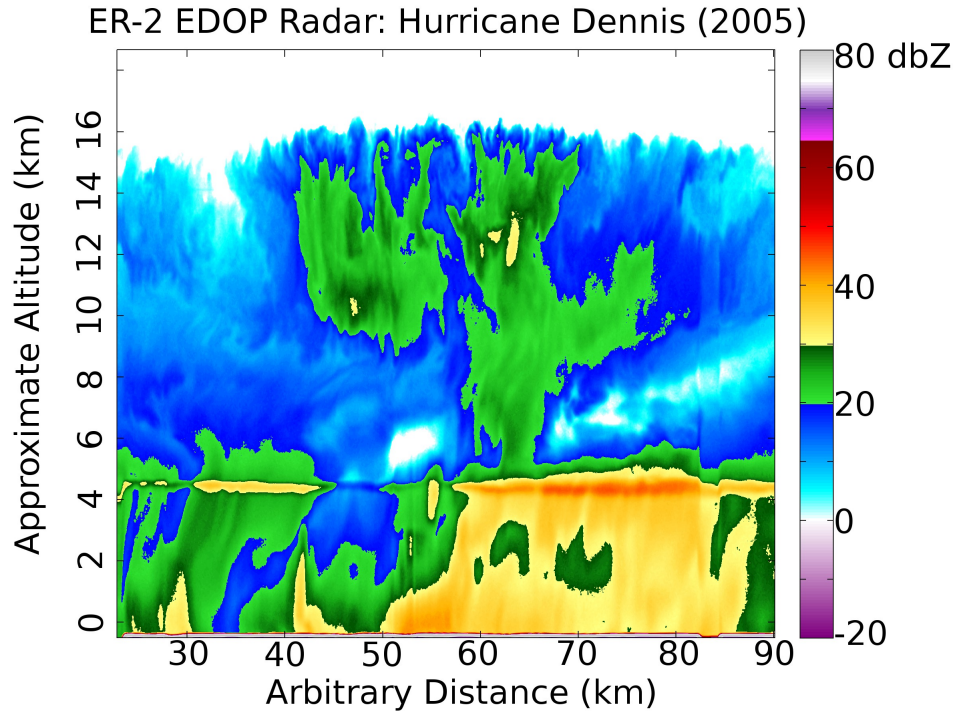


Figure 6.5: Example ER-2 EDOP radar cross-section. Note that the reflectivities for higher convection go far beyond 18 dBZ.

scale wind speed. What has not been done thus far, is a large, comprehensive study determining whether this holds true with a large sample of storms. This chapter describes such an analysis, using 1494 TRMM overpasses of tropical cyclones worldwide, focusing on areas within $2RMW$.

All storms, regardless of wind speed, are able to achieve near-tropopause 1st percentile brightness temperatures. However, median brightness temperatures, an analogue for storm-scale outflow height, is dependent on wind speed. In particular, the distribution of median brightness temperature (storm-scale outflow height) is sharper and at lower temperatures (higher altitudes) for stronger storms. Weaker storms have a wider distribution, and it peaks at higher temperatures (lower alti-

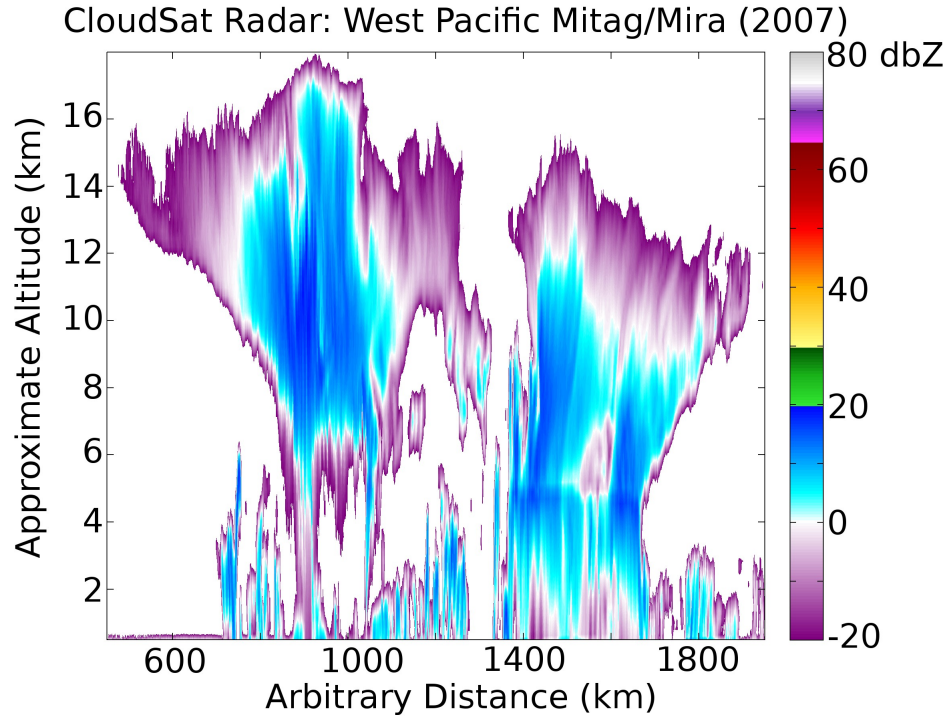


Figure 6.6: Example CloudSat radar cross-section. Note that the reflectivities for higher convection go far beyond 18 dBZ. Gaps at mid- and low-levels are because reflectivities with values greater than around 20 dBZ are not visible to CloudSat due to its different frequency.

tudes). The wider distribution is likely because there is a wider variety of shapes a weak storm can have than a strong storm.

Lastly, it is seen that low 1st percentile brightness temperatures are a necessary, but not sufficient, condition for rapid intensification. No RI storms have a 1st percentile brightness temperature above 205 K, whereas around 50% of non-RI storms have 1st percentile brightness temperatures above that. Since the 1st percentile will pick out hot towers, this means hot towers are a necessary, but not sufficient condition for rapid intensification.

Radar echo tops were found to be typically around 5–9 km in height with few reaching above that. Hence, fluxes are highly concentrated or contain major hydrometeor size distribution differences, with isolated areas that have larger hydrometeors, and the bulk of the storm losing most of its hydrometeors at low levels. Chapter 3 had a similar finding: the vertical volumetric mass flux is highly concentrated. A connection between the two is likely, especially since strong updrafts are known to produce large hydrometeors via graupel and hail processes.

As mentioned early in this chapter, other researchers have found a connection between hot towers and rapid intensification, and studies predict the relationship between storm-scale outflow and intensity. However, this work confirms those effects for a large sample set (139 TRMM overpasses), and provides a framework and database for further analysis. These results will be useful as model diagnostics, since the exact same statistics used here can be analyzed in a large sample set of tropical cyclone simulations to evaluate whether model cloud tops are realistic. This analysis will be done in Chapter 9.

Chapter 7

High-Resolution HWRF: Design, Rationale and Bugs

This chapter introduces the model on which diagnostics will be performed. Decisions that must be made in designing a high-resolution model are discussed and the particular choices made are explained. This chapter and the next will also introduce model diagnostics, based in part on observational work presented in previous chapters.

The model being examined contained a major bug, which also exists in the current operational HWRF, and went undiscovered for over two years. Model diagnostics that led to the discovery of this bug are presented in this chapter.

The next chapter will build on this one, by presenting a more complete analysis of the buggy and bug-free version of the model aimed at assisting future development of this model.

This chapter is divided into five sections. *Designing a High-Resolution Hurricane Model* explains decisions that must be made when designing a high-resolution tropical cyclone forecasting model. *High-Resolution HWRF* explains the design of the model analyzed in this thesis: high-resolution HWRF. *High Resolution HWRF Forecasting Ability* shows the high forecasting ability of this model in comparison with operational models. *Ice-Water Forgetfulness Bug* describes a major bug found in the model, that is also present in the current operational HWRF. *Fixing the Bug*

— discusses how the bug was fixed, and the improvements to forecasting ability after the fix. *Conclusions* summarizes results.

7.1 Designing a High-Resolution Hurricane Model

Five years ago, one of the major questions in hurricane modeling research was, “do we need a high-resolution model to simulate a hurricane’s intensity?” Now, the answer is known to be “yes,” due to many small-scale dynamical processes that are able to impact tropical cyclone intensity. As discussed in chapter 4, these features are not only needed for their dynamical processes, but are also needed to merely resolve the wind maximum, the definition of intensity.

Small-scale features contribute to intensity and intensification. If we want to model intensity change, we need to be able to either model those features, or their effects. We also need to be able to resolve the gridpoint maximum wind since that is the measure of model predicted intensity used by NOAA. While Chapter 4 examines the resolution dependence of resolving the wind maximum, the problem is more complex than that. A number of features and physical processes that are critical to intensity change cannot be resolved without a high-resolution model.

The first and simplest aspect of that problem of resolving intensity change is that a low-resolution model cannot even resolve the storm. This is exactly the same as the problem of being unable to resolve the wind maximum, as explained in Chapter 4, but the problem extends to all 2D and 3D fields. This is especially true of small storms, whose RMW is near or below the resolution of the model, preventing

the storm-scale structure from even being represented. This has been a problem with HWRF with storms such as Hurricanes Karl (2010) and Alex (2010). Hurricane Alex (2010) is a notorious example for HWRF, when the operational HWRF was unable to represent the reorganization of Alex after it passed the Yucatan. Instead of turning it into the compact 17 km RMW storm that it was, the 9 km resolution HWRF model generated a giant 300 km RMW monster storm, albeit with a maximum wind value not far from reality (Trahan et al., 2010).

How often this problem will occur can be judged from Figure 7.1, which shows the radius of maximum wind and the radius of the outermost closed isobar (ROCI) at mean sea level pressure (MSLP), two different measures of storm size, taken from the TCVitals database, which has a minimum of 9 km for RMW. We can see that typical global model resolutions of 30 km and worse will have an RMW below their resolution fairly often.

Next among the horizontal scales to be resolved are the rainbands, eye and eyewall (or eyewalls), and non-convective regions between the rainbands and eyewalls. As explained in Chapter 2, these features are important for the structure and evolution of the hurricane, including the intensity, size and track. They vary in scale, especially rainbands, which can be thin streaks near the eyewall, only 10 km wide, or outer rainbands hundreds of kilometers in scale. Eyes can vary over an order of magnitude, such as Hurricane Wilma's (2005) (Pasch et al., 2006) 5 km diameter eye at peak intensity, and Hurricane Dennis (2005) (Bevin, 2006) with an eye as large as 100 km diameter.

If one can resolve the rainbands, eye and eyewalls, then the next horizontal

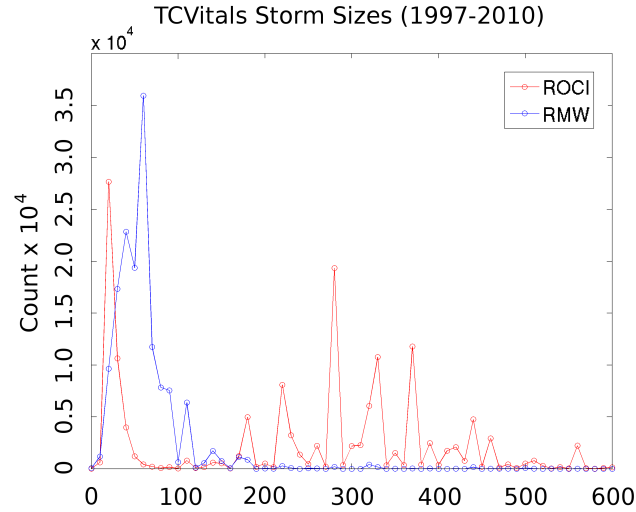


Figure 7.1: Radius of Outermost Closed Isobar (ROCI) and Radius of Maximum Wind (RWM) from a large number of tropical cyclones worldwide, taken from the real-time TCVitals database.

scales to resolve are those involving the numerous features within. Vortex Rossby waves and mesovortices in the eyewalls are believed to be critical to fluxes that allow storms to sustain higher intensities than the symmetric MPI theory suggests, due to asymmetric fluxes contributing to both the symmetric component of the storm, and to local increases in wind speed (Montgomery et al., 2009; Kossin and Schubert, 2004; Montgomery et al., 2006). Studies have shown that resolutions of, nominally, 2–6 km are enough to simulate these features (Davis and Bosart, 2002; Liu et al., 1997; Gentry, 2007; Davis et al., 2010).

There is also the complicated matter of convection. At scales much larger than a convection cell, using a convection parameterization is necessary. However, resolutions of, nominally, 4 km and lower are able to resolve convection (Weisman

et al., 1997; Davis and Bosart, 2002; Davis et al., 2010). That is corroborated somewhat by the analysis of the scale of convection in Section 3.4.1, where a scale of convection of, nominally 1–6 km was found and a scaling regime below that.

A number of other features of interest must be resolved. This includes downdrafts, for which either a convection parameterization, or explicitly resolved convection (nominally, 4 km or better resolution) is required and sufficient representation of non-hydrostatic processes (Weisman et al., 1997; Kato and Saito, 1995). Also, sheets of boundary layer rolls are known to exist in hurricanes and contribute significantly to fluxes. Those have wavelengths of 2–12 km, and since they have a wave structure, at least four times that resolution is required to even express them in a model. Boundary layer parameterizations with non-local mixing processes can take into account the mixing processes involved in the smaller rolls, somewhat mitigating that problem.

Reasonable high-resolution features can develop in a high-resolution model that is initialized and forced with low-resolution initial and boundary conditions. This was seen, for example, in two well-validated simulations: Scott Braun’s simulation of Hurricane Bonnie (1998) (Braun et al., 2006; Braun, 2006; Cram et al., 2007), as well as another group’s simulation of Hurricane Andrew (1992) (Liu et al., 1997), both of which were initialized by 2.5° resolution GFS GRIB files. This means that, although one must have the resolution and physics to model the features of interest, the parent model does not need to.

7.2 High-Resolution HWRF

The model used for this analysis will be a high-resolution (3 km) version of the HWRF model, which is a modified version of the 9 km resolution NCEP operational HWRF model, described in detail in Appendix A. A multitude of problems had to be overcome in order to produce this model. Only the problems relating to dynamics are discussed in this chapter. Some of the other problems are discussed in Appendix C.

The initial and boundary conditions for the model come from the NCEP operational GFS global spectral model, also described in Appendix A. This modified HWRF has three computational domains: one $75 \times 75^\circ$, 27 km resolution stationary outer domain, one $10 \times 10^\circ$, 9 km resolution storm-following domain, and a $6 \times 6^\circ$, 3 km resolution storm-following domain. The 3 km resolution was chosen because it was the highest resolution that was able to be run with the available real-time computational resources and within other, technical limitations.

The starting point for designing this model was the 2011 NCEP operational HWRF model, chosen because it has a competitive track forecasting skill, and its intensity forecasting errors are ones that should be solvable through higher resolution. Specifically, the model is incapable of representing small storms, and has a habit of rapidly expanding them, sometimes by a large amount in the first 12 hours of the simulation.

The outer 27 km domain was designed around the needs of hurricane track forecasting skill. The GFS, as will soon be shown, generally has better track forecasts

than any of the regional models, and also has a resolution close to 27 km. Hence, the outer domain was designed to be as similar as possible to the GFS model. Some differences remain due to the needs of hurricane forecasting and the different dynamical cores. These differences are the same as those of the low-resolution HWRF. The HWRF uses the Ferrier (or ETAMP) microphysics scheme and is non-hydrostatic, while GFS uses an older scheme and is hydrostatic. Both of those differences are required to produce microphysics and non-hydrostatic variables for interaction with the 9 km domain. Also, like low-resolution HWRF, the GFS momentum mixing and shallow convection are both turned off, reducing subgridscale diffusion effects. That was found to be necessary to simulate storms other than the storm of interest (storms in the 27 km domain).

The 9 km and 3 km domains were modified somewhat to improve the hurricane boundary layer. The momentum diffusivity constant was reduced, and the dynamical core diffusion constant was also reduced. These suggestions from HRD tended to reduce the model's habit of producing unrealistically large boundary layer depths in their idealized simulations. This tuning also eliminated the model's prior gigantic positive intensity bias, reducing it by more than 15 knots in the 2010 North Atlantic.

The 3 km domain varies from the 27 km and 9 km domain in one critical way: the convection scheme is disabled. This was done for many good reasons. The first reason was a practical one: it further reduced the positive intensity bias. Also, with the convection scheme enabled, the storms were highly symmetric, and had little resemblance to an actual hurricane. In addition, as discussed in the prior section,

there are a number of features that can be resolved at 3 km resolution, so long as one does not use any parameterizations that destroy the near-gridscale horizontal features. Convection schemes, due to their rearrangement of the entire vertical column of the atmosphere, are particularly bad for that. The other parameterizations are identical to those of operational HWRF, detailed in Appendix A. These were chosen out of necessity, and with very little freedom due to some limitations of the HWRF system.

7.3 High Resolution HWRF Forecasting Ability

Research papers on hurricane models, at this point, usually delve into analyses of model fields, comparisons to observations and the like. Those analyses, in and of themselves, are of limited use to operational forecasting for one important reason that the research community nearly always overlooks. A model that produces one perfect simulation will usually perform poorly when run for a large sample of hurricane simulations, *if* it is able to even run on such a large dataset without crashing or requiring human intervention.

One goal of this research is to benefit operational forecasting models, so these forecasts were run for a large sample set. In particular, 48 storms were run, and simulations were run every 6 hours of each storm's lifetime, as is done in operational mode. That amounted to a total of 1035 simulations. The sample set was chosen by the National Hurricane Center, taking storms from 2008–2010 North Atlantic and 2009–2010 East Pacific Seasons.

High-Res HWRF and Others: Intensity Error

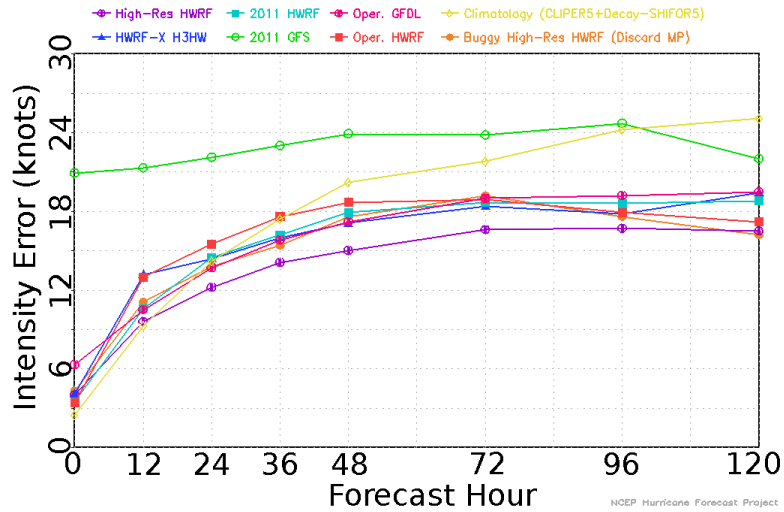


Figure 7.2: Wind intensity error: mean absolute difference between model predicted gridscale 10 meter wind and observed one minute sustained ten meter wind over a large number of simulations. See Table 7.1 for a larger legend.

Analysis of the model’s forecasting skill is ongoing. However, a comparison of skill for 2010 North Atlantic forecasts is available and this model represents big improvements over past HWRF versions. The storm structure is greatly improved, and the intensity is better. Storm structure is not something that can be easily quantified, but intensity can, and so it will be discussed in detail here. Also, it will be shown that track forecasting skill of this model is comparable to that of other operational models.

The primary intensity measure used by NOAA is the one minute sustained ten meter winds. A measure of the skill of that field is shown in Figure 7.2 which shows the mean absolute intensity error (relative to observations) as a function of forecast hour.

Name	Description
High-Res HWRF	the model discussed here. Purple lines with circles.
Buggy High-Res HWRF	the previous high-resolution HWRF, with a microphysics-related bug that will be discussed later. Orange with filled circles.
2011 HWRF	one of the two models from which high-resolution HWRF was derived. Cyan with squares.
HWRF-X H3HW	the other model from which high-resolution HWRF was derived. Designed by HRD and run in real-time in 2010. Blue lines with triangles.
2011 GFS	parent global model that feeds boundary conditions and input conditions to high-resolution HWRF. The 2010 retrospective runs of the 2011 GFS were used.
Oper. GFDL	the NCEP operational GFDL simulations of 2010. Pink lines with circles.
Oper. HWRF	the NCEP operational HWRF simulations of 2010. Orange lines with circles.
Climatology	a pair of statistical models that guess hurricane track and intensity based on climatology data.

Table 7.1: Description of models shown in figures 7.2, 7.3 and 7.4

High-Res HWRF and Others: Intensity Bias

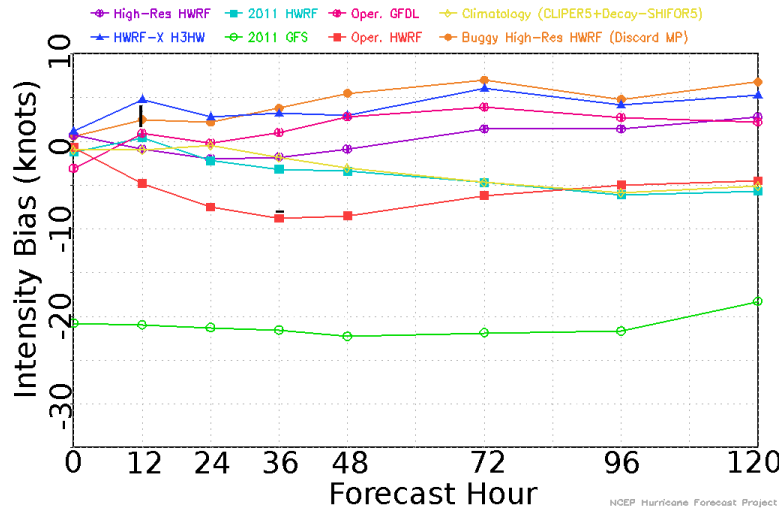


Figure 7.3: Wind intensity bias: mean difference between model predicted gridscale 10 meter wind and observed one minute sustained ten meter wind over a large number of simulations. See Table 7.1 for a larger legend.

It is clear from this that the intensity errors of the high-resolution HWRF are superior to all other plotted models. In Figure 7.3, we see that the intensity bias (mean non-absolute deviation from observations) is close to zero. Recall from Chapter 4 that a zero intensity bias is not what is expected in a correct finite difference model. However, the expected bias for a 3 km model is around 2%, which corresponds to 0–3 knots, so this problem is quite small, especially in comparison to the 15 knot absolute error in the intensity.

The track errors are competitive, but not superior, as can be seen in Figure 7.4. The track errors vary between that of the two progenitors of this model: 2011 HWRF and HWRF-X H3HW (cyan and blue lines). This is thought to be the combination of two factors: the outer domain parameterizations are run less frequently than in

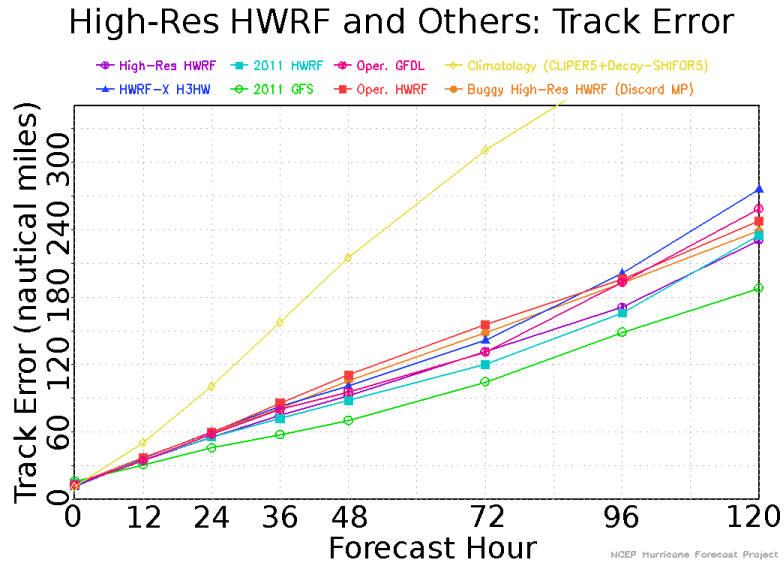


Figure 7.4: Track error: mean distance between model predicted storm center location and observed storm center location, averaged over a large number of simulations.

See table 7.1 for a larger legend.

2011 HWRF out of computational necessity, and a slightly different surface layer tuning is used to tune hurricane intensity. However, the surface layer tuning will affect all three computational domains, not just the inner 9 km and 3 km domains that contain the hurricane. Plans to improve the track forecast are in progress.

The current version of this experimental high-resolution model is competitive with operational models. Previously, this model had a positive intensity bias of 15–20 knots and track errors far worse than any regional model. The tremendous improvement in such a short time was due to model diagnostics and hard work. A full explanation of all diagnostics and problems solved would take hundreds of pages, so only some will be listed in this chapter and the next. In particular, diagnostics that led to the correction of a major microphysics-related bug will be discussed, and

diagnostics related to a current effort to improve the small-scales in the hurricane will be presented. (A few larger problems encountered and how they were solved is described in Appendix C.)

7.4 Ice-Water Forgetfulness Bug

Upon beginning this model to observational comparison, the goal was to redo the same analysis performed for observational data using model output, and look for discrepancies. This analysis resulted in discovering a bug that had gone unnoticed for over two years. A number of analysis methods led to discovery of this bug, but for the most part, they are the same methods that will be described in the next chapter. Hence, for brevity, only the last two analyses are shown here as they are the two that were critical to the discovery.

After comparison of the model to in-situ wind data (which will be discussed in the next chapter), a subjective analysis of cloud tops ensued. The initial goal was to do a subjective comparison of the type seen in Chapter 5.

A direct comparison of TRMM brightness temperatures to simulated TRMM brightness temperatures could conceivably be done, but was deliberately avoided. That is because comparing simulated brightness temperatures to real ones would not be a validation of just the HWRF model. It would be a validation of the combination of the HWRF model and the radiative transfer model used to generate the simulated brightness temperatures.

Instead, the TRMM brightness temperatures are treated as cloud top temperatures, and are compared against model cloud top temperatures. The “cloud top” is somewhat of an arbitrary distinction: how much condensate is required for something to be considered the “top” of the cloud? Various cutoffs should be used in any model analysis to determine the sensitivity to that cutoff. For each cutoff

chosen, the “cloud top temperature” is the temperature interpolated to the location where the condensate mixing ratio is equal to the desired threshold. In this analysis, mixing ratios of between 10^{-7} to 10^{-3} were tried, with 10^{-5} appearing closest to reality.

An especially surprising feature appeared just after every nest motion: mid-level clouds spontaneously appear. In GOES Rapid Scans, such features do not occur in only three minutes, so this suggested something is wrong, probably with the microphysics around the time of nest move. A detailed examination of the model source code revealed a section of code that discards all microphysics information, other than total condensate mixing ratio, every time the nest moves. The Ferrier microphysics scheme that is used in HWRF is designed to assume all condensate is small liquid cloud droplets when this happens. This effect is illustrated in Figure 7.5 which shows the ice fraction.

Hence, every time the nest moves, enormous amounts of latent heat is artificially generated by simply “forgetting” that most of the condensate was ice before the nest moved. Over the course of a half hour or so after the nest moves, the droplets freeze and the latent heat is released into the atmosphere. Unfortunately, the nest generally moved again before or not long after the ice reforms, so this extra “voodoo energy” is being deposited almost constantly. The effect that has on the storm environment was clear. A number of thunderstorms that were not part of the hurricane were being driven mostly by the “voodoo energy.”

This was clearly seen in movies of the 500 mbar geopotential heights, ice fraction and cloud top temperature. Every time the nest moved, there was a clear shock.

Giant gravity waves were launched from any region that had ice-phase condensate. In Hurricane Karl (2010) after it passed the Yucatan, thunderstorms to the west of the storm could be seen getting suddenly stronger after every move, slowly having more and more of an impact on the steering flow.

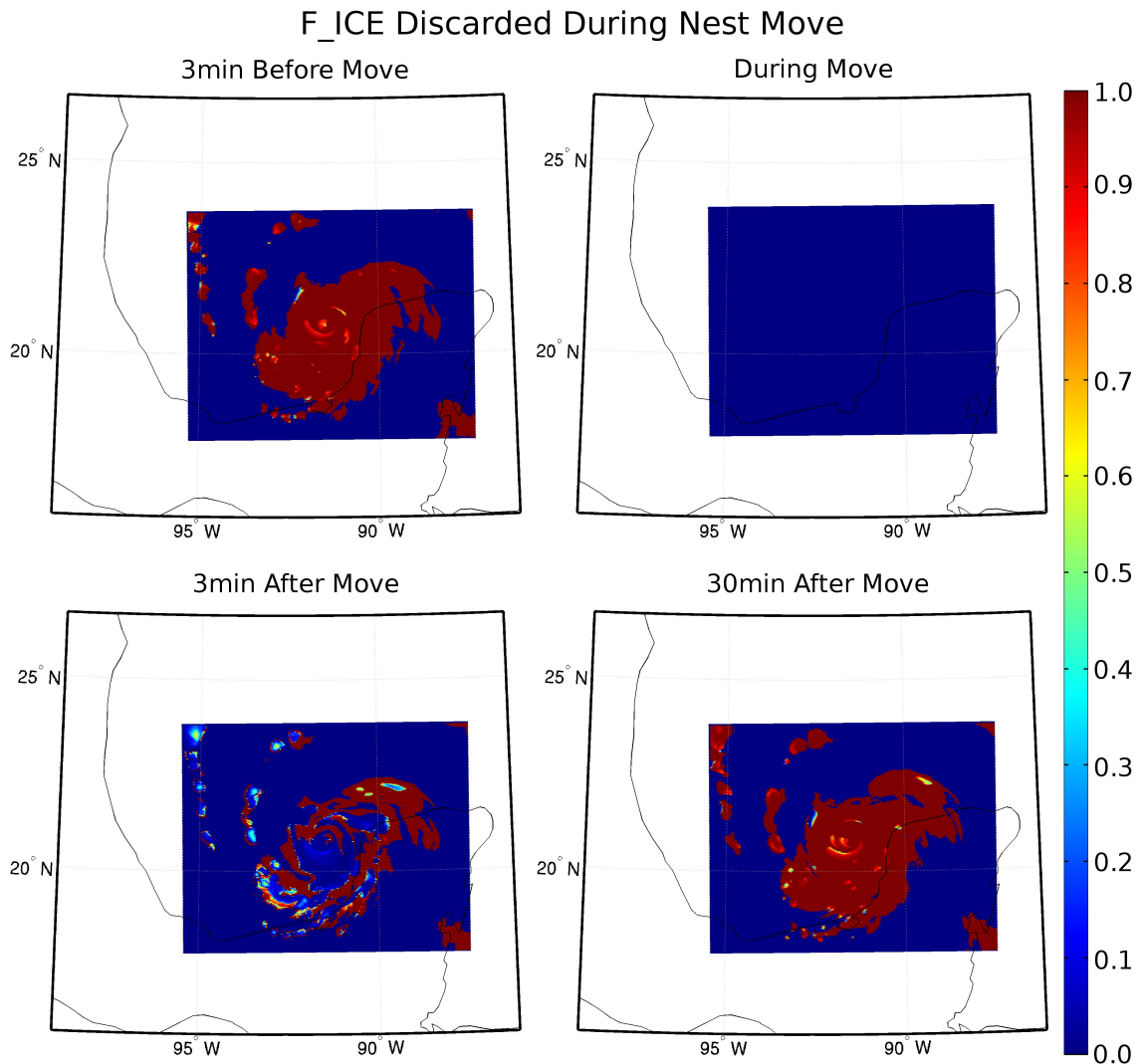


Figure 7.5: Ferrier Scheme ice fraction (fraction of condensate in ice form). Top left: 3 minutes before the nest moves. Top right: at the time of nest move. Notice that all ice fraction has been set to 0, indicating rain. Rain fraction and riming factor (not shown) have been modified to change the rain to small cloud droplets. Bottom left: small cloud droplets start to freeze. Bottom right: a half hour after nest moves, the atmosphere has recovered.

7.5 Fixing the Bug

Removal of this bug has a substantial positive effect on the forecasting skill, as can be seen in earlier figures. Figure 7.2 showed intensity error. The orange line labeled “buggy high-res HWRF” is the version with the bug, while the purple line labeled “high-res HWRF” is the corrected version. This bug removal results in a substantial improvement in the intensity forecast, allowing the model to surpass all other regional models shown. Track forecasting skill had a similar improvement, shown in Figure 7.4. With the bug, the model is usually the second worst model shown here. Without the bug, the model track is almost as good as 2011 HWRF.

7.6 Conclusions

This chapter presented the model that will be used to demonstrate diagnostics in this thesis. This model is a high-resolution version of the NCEP operational HWRF model, and is intended to become the 2012 operational HWRF, subject to resource limitations. In developing this model, many issues were found and fixed. One major bug was found, that also existed in operational HWRF, wherein the model “forgot” the type of condensate present in the atmosphere every time the nest moved, and reverted it all back to small cloud droplets. Correcting this bug had a substantial positive effect on the forecasting ability of the model, giving it track skill competitive with operational models and intensity forecasts better than operations. There were many other model problems found and fixed, and some are discussed in Appendix C.

The next chapter will continue on from this point in the analysis. The high-resolution HWRF with the bug fix described, is the current “best known working” version of high-resolution HWRF. It is that version that is being run in real-time as part of a joint NOAA HRD-EMC effort towards producing the 2012 HWRF. This model will be analyzed in more detail in the next two chapters to demonstrate more model diagnostic tools. Comparisons of the buggy and bug-free versions are shown, since they may shed light on issues not yet solved.

Chapter 8

Model Diagnostics: In-Situ Data

The previous chapter introduced a high-resolution HWRF model. A bug was found in that model, and is also present in the operational HWRF. That bug was corrected, and a test set of 1035 forecasts, chosen by the National Hurricane Center, was run with the corrected model. This set of runs will now be analyzed in more detail using a more complete suite of diagnostic methods. The goal of this analysis is to diagnose how physical processes are being represented in the model and whether they are realistic, guided by the statistical signatures inferred from the observations of tropical cyclones discussed in previous chapters.

This chapter develops diagnostics methods for performing a scale analysis on model fields and comparing it to results from in-situ NOAA WP-3D Orion aircraft measurements, as analyzed in Chapter 3. This chapter also analyzes the decrease in maximum wind with decreasing resolution, akin to what is done in Chapter 4.

The organization of this chapter is as follows.

Section *Simulated Aircraft Measurements* describes how the model was run with high-frequency output, allowing a fake NOAA P3 Orion to be flown through it via interpolation. This is extremely computationally intensive, so only one pair of simulations (one from each of two model configurations) is analyzed this way. The analysis of that simulation begins in *Vertical Wind PDF* which analyzes modeled

and actual vertical wind one-point PDF, using data from the simulated P3 campaign. *Structure Functions* continues by comparing the model and simulated structure functions. All 1035 simulations run are then analyzed in *Maximum Wind Dropoff with Resolution* which uses results and methodology from Chapter 4 to analyze the behavior of the model in the first six hours of the simulation as the model adjusts to its initial state. *Possible Reasons for Missing Downdrafts* speculates as to reasons why the high-resolution HWRF has little or no downdrafts. Lastly, *Conclusions* summarizes results and discusses implications.

8.1 Simulated Aircraft Measurements

A scale analysis of P3 airplane track measurements has two critical properties. First, the data is in radial passes, typically at a constant pressure level. Second, they are measured by a plane moving at a finite speed. Any two measurements compared are in the same radial pass, and are separated in both space and time. Having all data in radial passes means inner radii are sampled more than outer radii. Simulated aircraft measurements must reproduce these two sampling characteristics in order for the comparison to be fair and meaningful.

The model vs. P3 comparison was performed by first running the model with output generated every 3 minutes. Then, a fake NOAA P3 Orion aircraft was flown through the model on constant pressure levels in radial passes every 30° in a pattern simulating that of a real measurement campaign. The ground speed used was 135 m/s which is the median ground speed of all measurements from all radial passes in the 18 available storms. This is shown in Figure 8.1: 4D model data is linearly interpolated spatially and temporally to an aircraft moving through model fields. This is done for radial transects every 30° at several different vertical levels.

The North Atlantic Hurricane Karl (2010) was chosen for this, at the September 15, 2010 6:00 UTC cycle. This is the third forecast cycle of Karl, chosen because it allows some time for the model to “spin up” a realistic vortex. The time period analyzed is 12:00 UTC September 16 through 6:00 UTC on September 17, which overlaps with a NOAA P3 Orion flight. One unfortunate problem is that NOAA HRD, which manages the P3 aircraft, stopped producing vertical wind data after

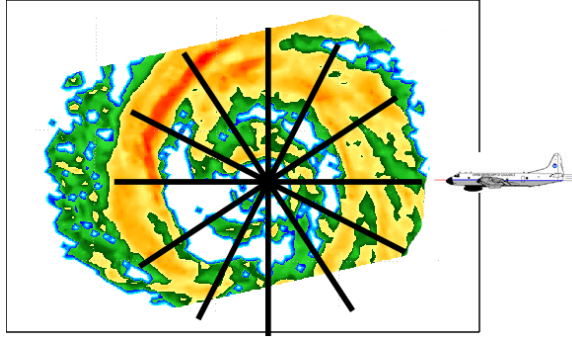


Figure 8.1: Diagram of the “fake P3 campaign” whereby model data is linearly interpolated in space and time to the location of an imaginary P3 flying through the moving storm.

2008, so no direct comparison to the vertical winds in Karl is possible. However, comparison to universal statistics in past storms can be done.

8.1.1 Vertical Wind PDF

The first analysis is of the vertical velocity one-point PDF. The P3 data for Karl has no vertical velocity because HRD stopped reporting that data after 2008. However, Chapter 3 found a similarities between the shape to the one point PDF of the vertical wind between several storms, so this section compares to other storms. This illustrates the reason why universality was sought in observational data: if a property holds for all storms, then one does not need data for the same storm to do diagnostics on a simulation of that storm.

The only data used from the model in the PDF was within 150 km of the storm center, to try to keep in line with typical P3 flight leg lengths. The wind observations have been boxcar filtered with a 3 km width filter to account for the effects of the finite difference 3x3 km model implicit averaging. Note that the 3 km linear boxcar filter is a linear radial average rather than a 2D average. At a 3 km resolution, much smaller than the scales of rainbands and eyewalls, the effect of cross-track averaging is assumed here to be minimal. Attempting to apply this same analysis with a larger averaging window would be questionable, however, since vertical wind varies rapidly between convective and non-convective regions and a large cross-track distance will bring in data from significantly different radii.

In Figure 8.2, wind from Karl after the bug fix is shown as black circles, while the wind before the bug fix is black crosses with observations shown in color. There is an increase after the bug fix in the frequency of vertical velocities around 1.5–4 m/s, making it somewhat more like the observations in that range. A clear difference

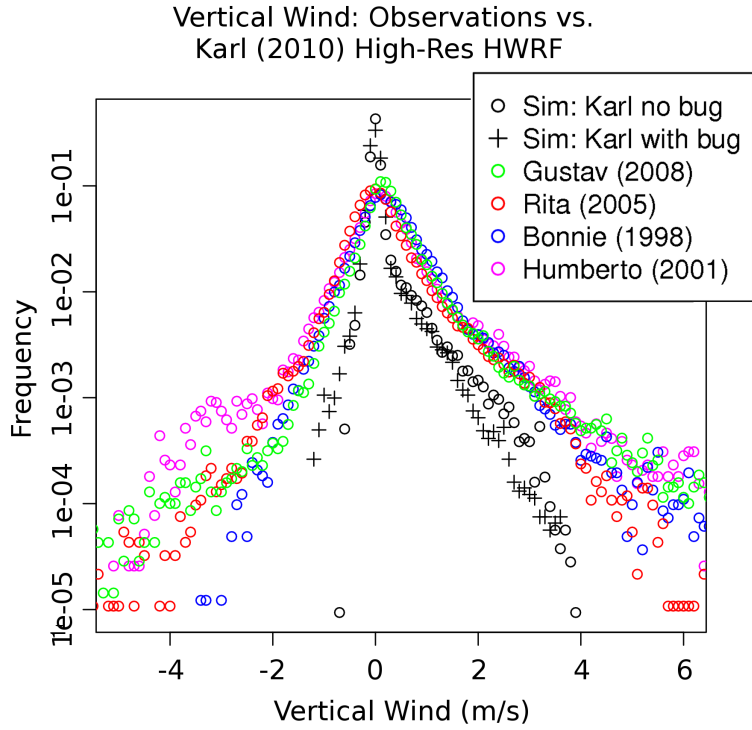


Figure 8.2: Distribution of vertical wind in four storms (colored) and two high-resolution HWRF simulations (black). Crosses are data from a Karl (2010) simulation with the microphysics bug discussed in Chapter 6, and circles are data from a Karl (2010) simulation with the bug corrected.

exists between the observations and the model. Values greater than 4 m/s are more frequently observed in the real atmosphere, but do not appear in the model.

Also missing from the model is downdrafts. This problem is worse with the bug fix added; the strongest downdraft seen is 0.5 m/s slower than in the buggy version of the simulation. This suggests that the main reason for downdrafts in the buggy simulation was the nest shocks caused by dumping of “voodoo energy” latent heat when the model forgot the ice/water phase distinction every half hour or so

during nest moves. Other downdraft mechanisms are apparently so weak as to be non-functional.

Note that the effect of removing the bug fix was to strengthen the updrafts and weaken the downdrafts, despite the removal of the “voodoo energy” latent heat. That is a somewhat counter-intuitive effect. Recall, however, that the energy is only inserted instantaneously in a “nest shock” event, and only in the mid levels where there is a significant amount of condensate that should be in ice form. Below that level, condensate is in liquid form and little or no latent heat is added during the nest movement shock. As one rises farther and farther above the freezing level, the amount of condensate decreases rapidly, and so does the added latent heat.

The effect of that is to make the areas below the freezing level more stable and the areas above the freezing level extremely stable, during the first microphysics timestep fifteen seconds after the nest move. However, that is not consistent with the wind field, which still had the structure of the convection cells that were present. One of the effects of this was actually to create giant storm-scale gravity waves every time the nest moves. The dumping of an enormous amount of latent heat at mid-levels also added to the overall stability of the atmosphere in cloudy regions, reducing the strength of upward motion and encouraging downward motions.

8.1.2 Structure Functions

8.1.2.1 Vertical Wind Structure Function

In model comparison, the vertical wind structure function has the ability to indicate whether the model has chosen some large scale as its scale of convection. It also has a value in determining what scales to use in the first place, when trying to resolve convection or parameterize it. In particular, the correlation length of 500 m for vertical wind indicates that 3 km may not be good enough to represent the horizontal structure of the vertical motion for smaller convection cells. However, the 1–6 km correlation lengths for radial wind suggests that this resolution *should* be able to represent the associated entrainment and detrainment for most cases.

With the bug (Figure 8.3), the structure function contains a power law rise and a level off at a scale break of about 7.5 km. That is larger than the typical scale break of 1–6 km seen in observations, and the model also has less variability than in observations. However, this is expected since the model cannot represent 1 km wide updrafts and downdrafts. The updrafts and downdrafts present represent an average over a 3x3 km region. What is curious is that the buggy version of the model captures the flat level-off after the scale break better than the buggy version does. The worsened lack of downdrafts in the bug-free version likely contributes to that.

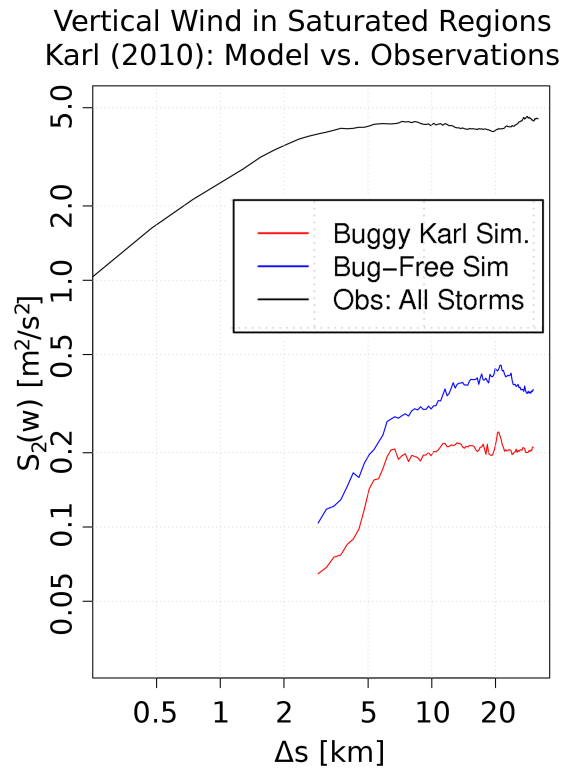


Figure 8.3: Structure functions of vertical wind in saturated regions in two Karl simulations and in all observed storms combined.

8.1.2.2 Tangential Wind Structure Function

Structure functions of tangential wind for the Karl simulations are shown in Figure 8.4b on linear axes and Figure 8.4a on logarithmic axes. Both the buggy and bug-free versions are able to capture the linear region after about 22 km, suggesting that the storm's large-scale vorticity structure is correct. For scales below about 12 km, both storms have noisy enough structure functions so that it is difficult to tell with certainty whether they agree with observations. This is simply a consequence of the resolution: with a 3 km resolution model (4.5 km diagonally), the spectral resolution is also low, so wavelengths close to the gridscale cannot have their power spectrum well represented.

That being said though, the bug-free version does display less of a oscillation in the structure function length with scale, largely due to the lack of large bogus gravity waves that were present in the buggy simulation.

The bug-free version has higher values at large scales (above about 17 km) indicating weaker gradients. It has lower slopes overall below about 12 km, indicating a less smooth variability. This suggests that the bug was causing spurious mixing, which may explain why the buggy version of Karl produced wider storms than the non-buggy version by about a factor of 1.5–2.

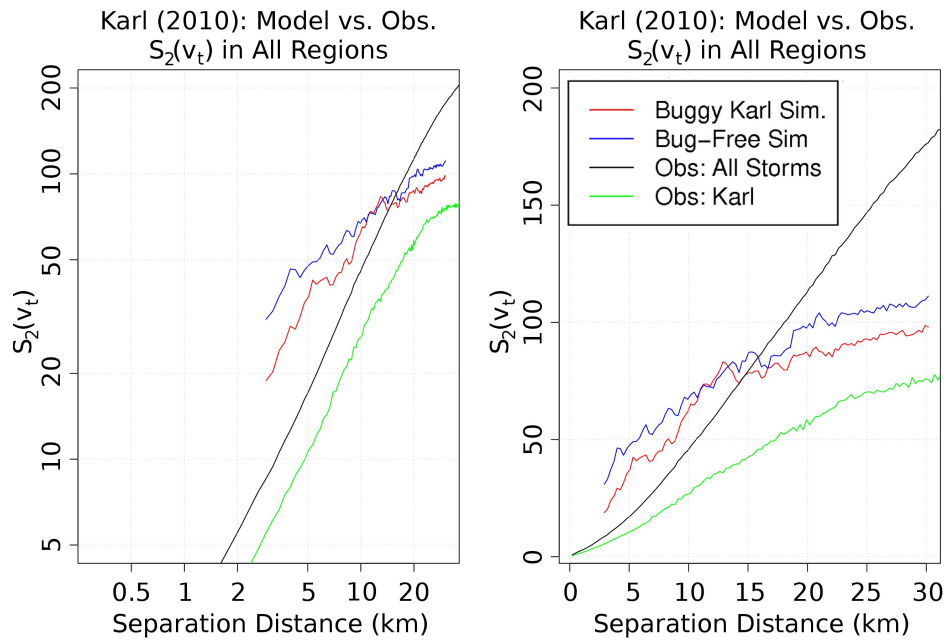


Figure 8.4: Structure functions of tangential wind in two Karl simulations, in observed Karl and in all observed storms combined. Left (8.4a): log-log plot, right (8.4b): linear plot.

8.1.2.3 Radial Wind Structure Function

Figure 8.5a shows the structure function of the radial wind in saturated regions on a log-log plot. The model does a reasonable job of capturing the power law region up to, nominally, 8 km, which is impressive given how close that is to the gridscale. Figure 8.5b shows all regions on a linear plot where a linear region can be seen in the combined structure function of all storms. The same slope is seen in the model structure function between about 10–17 km and 23–30 km, but with an odd behavior in between. That indicates that the storm-scale divergence field matches what is typical for storms, except in the 17–23 km region. The odd behavior in 17–23 km could be due to undersampling, but the sampling should be reasonable at that high a multiple of the grid scale. It can also indicate a storm-scale feature (such as the eye radius) exists around that scale (17–23 km). Eyewalls can have a strong impact on the structure function at scales similar to the radius.

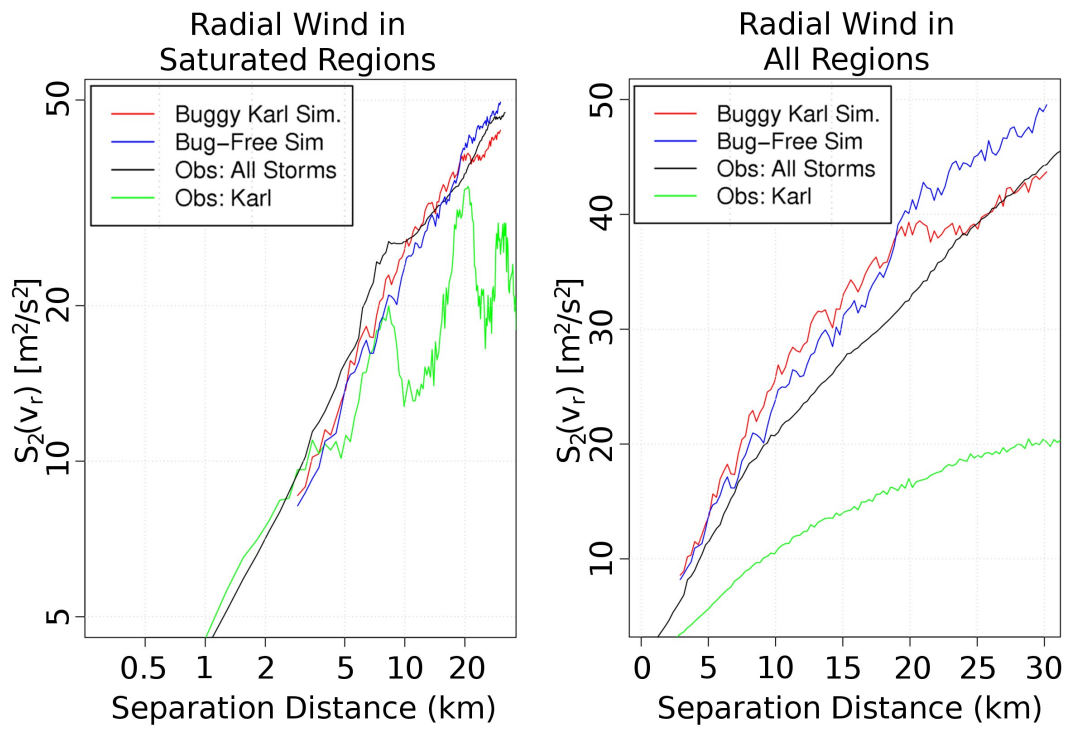


Figure 8.5: Structure functions of radial wind in two Karl simulations. Left (8.5a): saturated regions, on a log-log plot. Right (8.5b): all regions, on a linear plot.

8.2 Maximum Wind Dropoff with Resolution

In Chapter 4 the Utopian Model was introduced: a model that produces the perfect forecast 100% of the time, averaged and subsampled into a finite difference grid (or finite element grid, or spectral space). This was an estimate for the decrease in the maximum wind speed with the size of the averaging window. This section will compare those results to the model to estimate the impact resolution is having on resolving intensity, and also to evaluate behavior of the model in the first six hours of the forecast.

The model output fields for all simulations were run through three different hurricane tracker procedures to produce wind intensity and storm location for all forecast hours and the analysis time. For the 27 km and 9 km resolution tracks, the NCEP Tracker was used on the 27 km and combined 27+9 km domains, respectively. For the 3 km, the NCEP Tracker and HRD Diapost tracker were each run on the combined domain and were combined to a single track as explained in Sections C.2 and C.4.

For every one of the simulations, this produces three intensity estimates for each forecast hour: one 3 km resolution intensity, one 9 km resolution intensity and one 27 km resolution intensity. Hence, for each simulation \mathcal{S}_i , define the fractional dropoff \mathcal{F} of storm maximum wind \mathcal{I} at some resolution r relative to gridscale (3 km) intensity as:

$$\mathcal{F}(\mathcal{S}_i, r, h) = 1 - \frac{\mathcal{I}(\mathcal{S}_i, r, h) - \mathcal{I}(\mathcal{S}_i, 3, h)}{\mathcal{I}(\mathcal{S}_i, 3, h)} \quad (8.1)$$

where h is the forecast hour (or 0 for analysis time). When $\mathcal{F} = 1$, the resolution r

intensity is equal to the gridscale intensity, whereas when $\mathcal{F} = 0.5$, the resolution r intensity is half of the gridscale intensity.

Figure 8.6a shows a comparison of the model and observational dropoff of the 9 km maximum wind versus the 3 km resolution maximum wind at the analysis time. The dropoff of the observed winds is shown as red “x” marks, and the square of the observed dropoff is shown in black “x” marks. The model dropoff should be somewhere between the two in order to be physically consistent, and is shown as blue “+” marks. The model dropoff does generally stay similar to the observed dropoff. The only possible exception is in the 10–30 m/s range where some modeled storms are initialized with a 3 km maximum wind nearly the same as the 9 km maximum wind (the horizontal line of blue crosses, in the upper left portion of the plot).

This story gets more interesting when one analyzes the 6 hour forecast, whose comparison is shown in Figure 8.6b. The model dropoff for 3 km resolution intensity has spread by an enormous amount compared to at the analysis time in the previous figure (Figure 8.6a). This indicates that the wind maxima concentrate rapidly at the beginning of the simulation while the model rapidly “spins up” 3 km resolution structure. This is likely due to a limitation of the current initialization method: the HWRF initialization system is only able to put a vortex in the 27 km and 9 km domains. It allows the standard WRF initialization to simply interpolate the fields to the 3 km domain. The model reacts to this by immediately spinning up near-gridscale (3 km) local maxima that increase the 3 km intensity without significant increases to the other domains’ intensity.

The 27 km resolution maximum wind dropoff has a similar situation as the 9 km resolution. Figure 8.7a shows the analysis time dropoff and Figure 8.7b shows the 6 hr forecast. The maximum wind intensity fractional dropoff ($\mathcal{F}(\mathcal{S}, 27, h)$) again is much lower at the 6 hr forecast than at the analysis time. However, the agreement with observations is still quite good at forecast hour 6; the problem does not appear to be as severe as the 9 km resolution. This is consistent with the previous suggestion that the lack of a proper 3 km domain initialization is at fault; the 9 km domain is initialized with a balanced vortex. Hence, the portion of the 27 km to 3 km dropoff that comes from the drop from 27 km to 9 km resolution should already be physically consistent. That results in the erroneous portion of the 27 km to 3 km dropoff coming primarily from the problematic 9 km to 3 km dropoff.

A better way to see this is a scatter plot of the change in the maximum wind from 0–6 hr versus the change in the fractional dropoff \mathcal{F} from 0–6 hrs for 9 km resolution is shown in Figure 8.8. The dropoff in the observed maximum wind does not vary much as a function of 3 km wind speed, so the points, in a physically consistent model, should be close to the X-axis in that figure.

For significant decreases in the wind from 0–6 hrs (left half of plot), that is generally the case. However, sudden decreases of as much as -15 m/s of the storm intensity in only 6 hrs still indicates a problem. This sudden weakening of the initial vortex is a well-known problem in HWRF, not just in the high-resolution model, but in the operational model as well. Preliminary results in EMC and HRD have suggested that this is due to the vortex sometimes being far from gradient wind

balance. Improvements to the initialization system, provided by HRD in 2010, were able to reduce this problem. However, the initialization system is currently tuned for the 9 km resolution HWRF, which was not able to even represent smaller hurricanes, which can have eyewall radii less than 10 km. The system may need re-tuning for the more capable 3 km resolution model.

When the storm intensifies in 6 hrs (right half of plot), the maximum wind dropoff generally decreases, indicating that the maximum wind is getting more compact. This, again, is consistent with the hypothesis of 3 km features “spinning up” in the early parts of the simulation, producing strong localized winds. An example of such features is shown in Figure 8.9, which plots vorticity in the Karl (2010) simulation analyzed throughout this thesis. Vorticity dipoles are often seen in the low-level wind fields, associated with strong vertical motion in the center of the dipole. Sheets of alternating vorticity streets are sometimes seen (such as in the north-west corner of the figure). That is likely the model trying to produce boundary layer vorticity sheets often seen in hurricanes. Also present in the 3 km domain are spiral rainbands. None of these features can be represented in the 27 km domain. When they are averaged into the 9 km, they show up as blurred messes, with the fine scales lost, and decreased maxima.

Figure 8.10 a similar scatter plot as Figure 8.8, but for 27 km resolution. The results for 27 km are similar to the 9 km results, except that the increase or decrease in \mathcal{F} is larger for the 27 km domain by about 50%, suggesting that the concentration of wind maxima is happening over a larger area than just near the storm-wide maximum location.

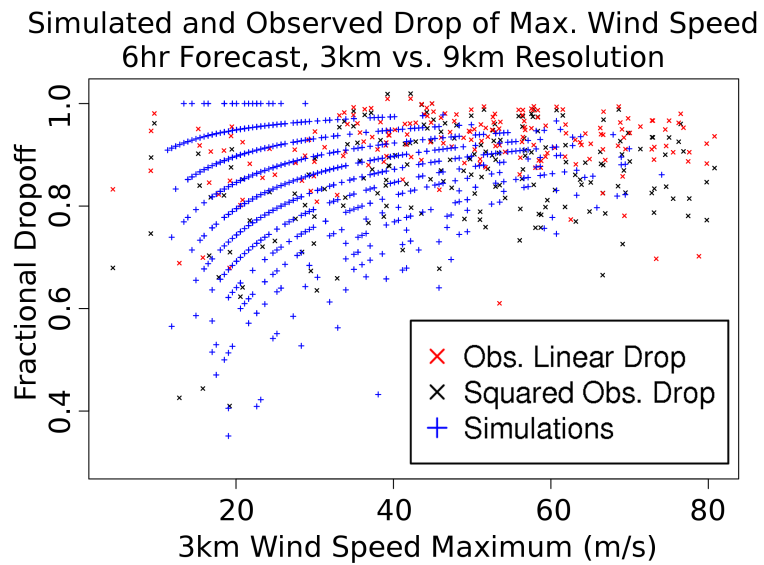
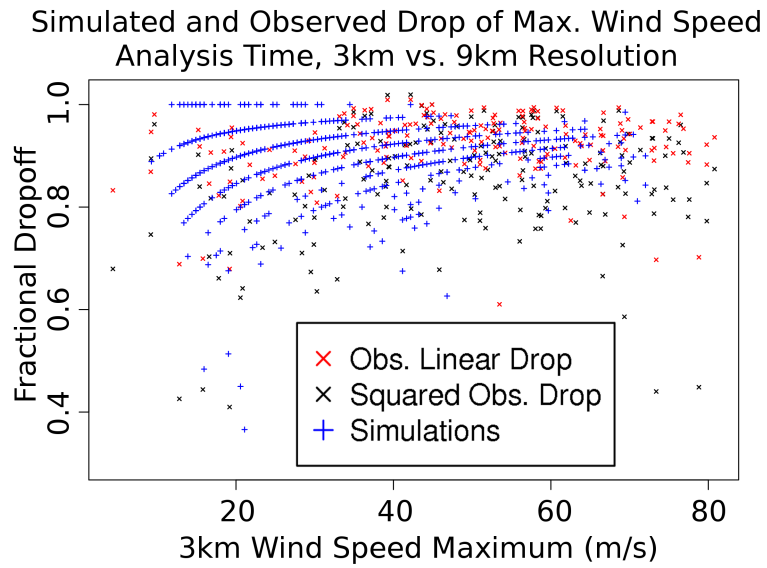


Figure 8.6: Top: fractional dropoff of the 9 km resolution wind maximum relative to the 3 km maximum, as a function of the 3 km maximum, at the analysis time. Bottom: same, but for the 6 hr forecast.

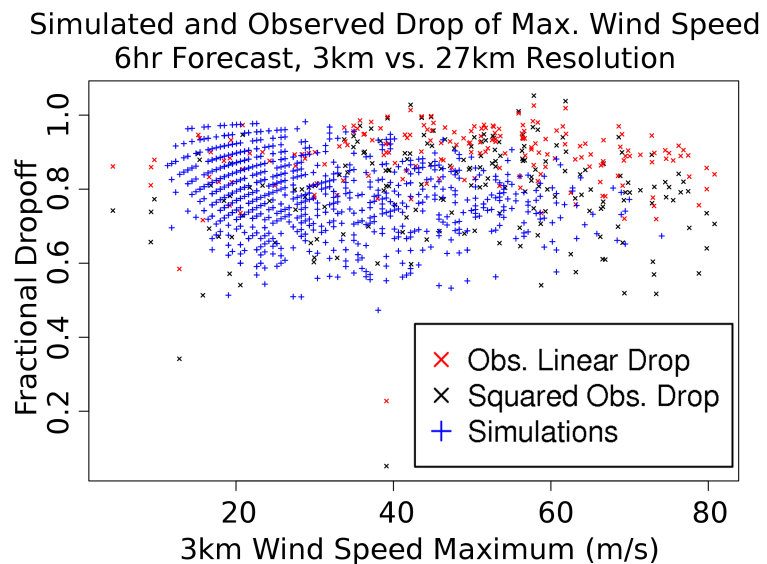
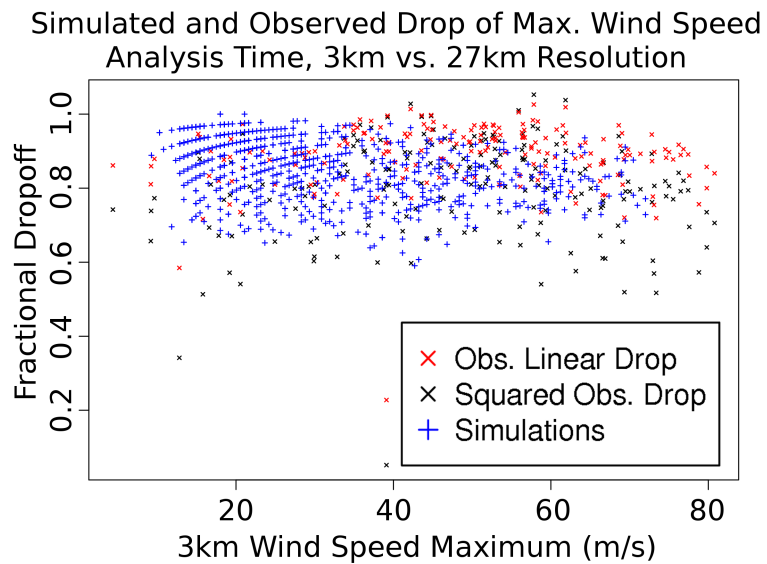


Figure 8.7: Top: fractional dropoff of the 27 km resolution wind maximum relative to the 3 km maximum, as a function of the 3 km maximum at the analysis time. Bottom: same, but for the 6 hr forecast.

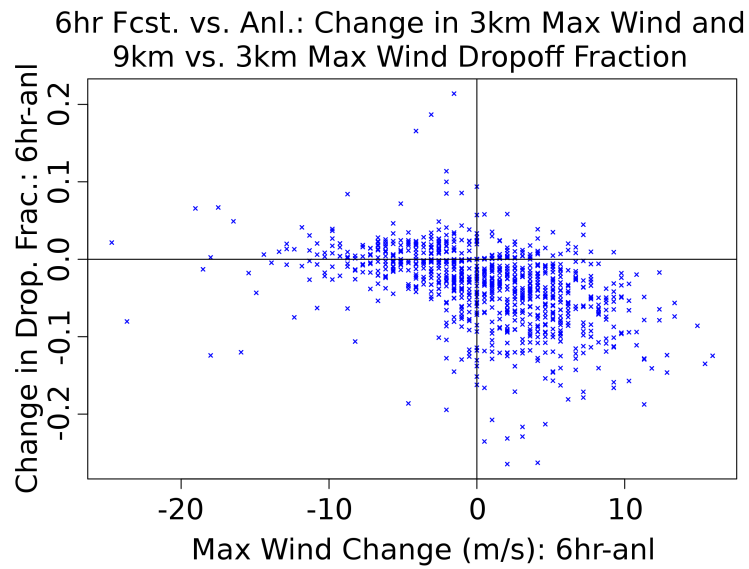


Figure 8.8: Change in the fractional dropoff \mathcal{F} and 3 km maximum wind between the analysis time and 6 hr forecast.

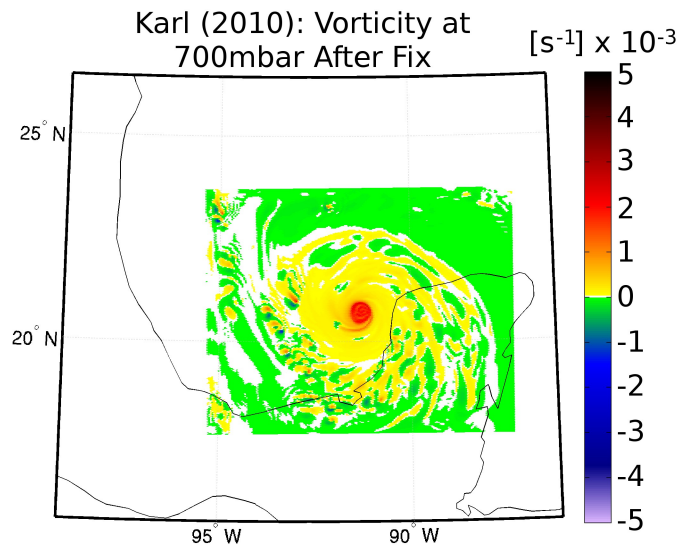


Figure 8.9: Vorticity field at 700 mbar from a Karl (2010) simulation, showing high-resolution features in the 3 km domain.

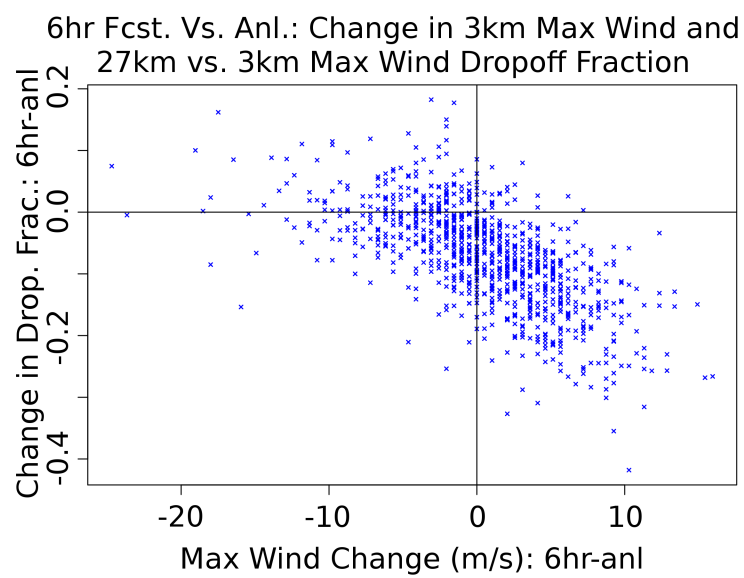


Figure 8.10: Change in the fractional dropoff \mathcal{F} and 3 km maximum wind between the analysis time and 6 hr forecast.

8.3 Possible Reasons for Missing Downdrafts

The model's downdrafts, which are weak and bordering on non-existent, have a few likely reasons that are worth investigating soon. The discarding of the non-hydrostatic state every time the nest moves may be contributing to these problems, and an insufficient representation of the non-hydrostatic state has been shown to reduce or eliminate downdrafts in explicitly resolved convection (Weisman et al., 1997; Kato and Saito, 1995).

Another possible factor is non-local mixing. The boundary layer scheme has a "should I trigger non-local mixing" feature (mixing between non-adjacent vertical levels). If that feature triggers, the entire boundary layer is rearranged within that atmospheric column, which may eliminate any features that could contribute to a downdraft.

In addition, the Ferrier scheme is a somewhat idealized scheme, designed for mid-latitude systems and computational efficiency. It does contain all of the critical physical processes, however, albeit in a more simplified form than the more advanced binned or multi-moment schemes. While it is reasonable to suspect that this scheme is incapable of being used for explicitly resolving convection, it is not a foregone conclusion. If it can be used for that without damaging the results, the Ferrier scheme should be used to avoid the expense of new 3D arrays required by the more advanced schemes.

However, there is another more fundamental problem with the design of the Ferrier scheme, similar to the bug discussed in Chapter 7. The WRF-NMM, when

run with the Ferrier scheme, advects total condensate, but not individual species. This is done under the assumption that, although hydrometeors may vary rapidly across short distances, the dynamics behind them does not (Ferrier, 2010). Where that breaks down is when one gridcell has a cloud (such as a rainband) and the next does not. The gridcell with no cloud will contain the default values for Ferrier microphysics fractions, which is small liquid cloud droplets. When a rainband's graupel and snow is advected to the next gridcell, the Ferrier scheme "forgets" the make-up of the hydrometeors, and assumes they were all cloud droplets. As with the similar bug during nest move, this produces extra "voodoo energy" due to the forgotten trapped latent heat in the ice phase. That extra "voodoo energy" then allows a boost to vertical development in the new gridcell.

More towards the direction of the simplicity of the scheme, microphysics is critical to downdrafts, through graupel and hail formation and raindrop collisions pulling down the surrounding air. Studies of the various more advanced schemes have been shown that changing the microphysics scheme, or even just tuning it, has a large impact on the representation of downdrafts and other tropical cyclone features (Franklin et al., 2005; Gilmore et al., 2004; Wang, 2002a). That suggests that trying a different microphysics scheme is worth an attempt for the HWRf model. Retaining the Ferrier scheme, but tuning it may also be an option.

8.4 Conclusions

This chapter compares in-situ observations to simulations of two versions of the HWRF model. The first included a bug in which, every time the nest moved, the model discarded all microphysics type information, changing all condensate to small cloud droplets without losing latent heat. That was followed immediately by rapid freezing in mid-levels, producing extra “voodoo energy” from the extra water to ice conversion. The other model version did not have that bug, and was otherwise identical. Both versions are analyzed here in the hopes that analyzing the effects of the “voodoo energy” bug will provide more insight into problems in the model.

It was found that the model has weak downdrafts, bordering on non-existent. This was worsened without the bug: rare -1.2 m/s downdrafts are seen with the bug and -0.6 m/s without with most downward motion being much weaker. Storms have downdrafts stronger than -5 m/s. Updrafts in the model were never stronger than 4 m/s, despite real storms having updrafts stronger than 5 m/s.

Convection cells were present, but with a larger size than in observations. A clear transition scale is seen in the vertical wind around 7.5 km in the buggy version of the model (real storms have 1–5.5 km transition scales), with no correlation between points separated by larger scales. That transition becomes much less clear after the bug is fixed, suggesting that these downdrafts were critical to the horizontal structure of vertical wind.

The radial wind structure function at large scales is similar to that of the “all storms” structure function, indicating that the large-scale divergence field has a

similar structure to that of typical storms, but the storm was too large by a factor of 2–3. Some aspect of the small-scale dynamics was unable to maintain Karl’s 17 km radius of maximum wind. The large convection cells may be contributing to that.

Section 8.2 analyzed the comparative intensity of the 3 km, 9 km and 27 km domains in the 0 hr and 6 hr forecasts. The dropoff from 9:3 km and 27:3 km was within the range expected from Chapter 4 results. However, the dropoff and the maximum wind itself change rapidly in the first six hours of the simulation, indicating that model “spin-up” issues are present. Some storms significantly intensify in 6 hrs. by gaining fine-scale 3 km resolution structure, with a much stronger 3 km resolution intensity than 9 km or 27 km. Other storms rapidly weaken, uniformly in all three domains.

Speculation was given for why the downdrafts are missing. Several simple reasons include the simple microphysics scheme used (Ferrier or ETAMP scheme), the effects of discarding the non-hydrostatic state every time the nest moves, or the presence of synoptic-scale dry air (a problem in all HWRF variants, including this one). However, there is one more complex problem that may contribute: not advecting condensate species. This has a result comparable to the nest movement bug described earlier, but is slower and likely will not result in the same giant gravity waves. Condensate advected from an icy region to a region with no condensate will be treated as small liquid cloud droplets after advection without any loss of latent heat. Extra freezing will occur, generating latent heat and vertical motion.

The next chapter will expand on this analysis by comparing model and observed cloud top temperature, using diagnostics developed in Chapter 6.

Chapter 9

Model Diagnostics: Cloud Tops

Chapter 7 introduced a high-resolution version of the HWRF model. Chapter 8 analyzed the high-resolution HWRF model by comparing its fields to in-situ results from Chapters 3 and 4. In this chapter, the model cloud tops will be analyzed using methods similar to those in Chapter 6. At the end of this chapter, the implications of the results of this chapter and Chapter 6 will be discussed.

The organization of this chapter is as follows. Section *Cloud Top Definition* explains how “cloud top temperature” was derived from model fields, to compare to TRMM 10.8 μm brightness temperature. Then, the analysis of this data begins in *Cloud Tops: Bulk Outflow and Intensity*, which compares median cloud top temperature (an analogue for the large-scale outflow) to intensity of the simulated storm. *Cloud Tops: Peak Convection and Intensity* compares 1st percentile cloud top temperature to intensity of the simulated storm. Finally, *Cloud Tops: Rapid Intensification* compares 1st percentile cloud top temperature to rapid intensification of the simulated storm. *Results and Discussion* summarizes results and discusses their implications.

9.1 Cloud Top Definition

This chapter will analyze a comparison of modeled and simulated cloud tops. To do this, first one needs a measure of modeled cloud top. The 18 dbZ echo top height is currently not available due to a bug in the post-processor, so that leaves only the possibility of comparing the cloud top temperature. A measure of the cloud top temperature could be created using a radiative transfer model designed to mimic the 10.8 μm VIRS channel. However, analyzing such simulated brightness temperatures would not be a model diagnostic, per se. Instead, it would be diagnosing the combination of the HWRF model and the radiative transfer model. The EMC version of the CRTM radiative transfer model is the only one tested with the HWRF model. Unfortunately, the CRTM was developed for EMC's 3DVAR data assimilation package, which is unable to assimilate cloudy radiances. That makes it extremely suspect for use in diagnosing simulated cloudy radiances.

Instead, this chapter directly compares the temperature of the cloud top. With the model, the full 3D cloud information and the full 3D temperature is available, so it is possible to determine the actual cloud top temperature. Since that is the quantity this chapter is actually trying to diagnose, it makes more sense to use it directly rather than simulating a radiance. Due to limitations discussed in Chapter 7, the Ferrier scheme was used as the microphysics scheme for this model. The Ferrier scheme's only prognostic variable is the total condensate mixing ratio (CWM). This is not ideal, since the hydrometeor types, mixing ratios, and size distributions are what is really required determine the top of the cloud. (Such information would be

needed for a radiative transfer model to produce accurate brightness temperatures as well.) One must make do with what one has, so the CWM was used for this diagnostic.

It is not clear what the exact mixing ratio is that one would call a cloud “top.” Mixing ratios of as little as 10^{-12} kg/kg were seen, and some very small amount of CWM was present in the lower stratosphere. Absent information about particle size and type, one must pick a threshold to call the cloud top, so multiple thresholds were tried. A value of $CWM = 10^{-5}$ has good agreement with measurements, and varying significantly from that value does not. Values from 10^{-7} through 3×10^{-3} were tried. The 10^{-5} cutoff is also used by EMC in its Unified Post-Processor for that reason (Chang, 2010). The highest level at which CWM was equal to the threshold was declared the cloud top for that atmospheric column, and the temperature was interpolated there and called the cloud top temperature.

The 1st percentile and median cloud tops within $2RMW$ were the statistics analyzed in Chapter 6 and will be used here. No compositing method is needed, since the only passes used are ones where the $2RMW$ region remains within the 3 km domain (which amounts to most of the simulations analyzed). Due to resource limitations, only around a third of the dataset is analyzed here.

9.2 Cloud Tops: Bulk Outflow and Intensity

The height of the bulk outflow in observed tropical cyclones was analyzed in Section 6.2, which used median brightness temperature within $2RMW$ and found a

strong relationship between intensity and bulk outflow height. Both the mode and width of the distributions of median cloud top temperature were strongly dependent on intensity, with stronger storms having a lower brightness temperature (higher height). Weaker storms have wider distributions that spread farther towards the near-300 K ocean temperatures.

Figure 9.1 examines a similar statistic for the modeled storms. Median cloud top temperature for various forecast hours are shown. The $CWM = 10^{-5}$ plots in the middle column bear a resemblance to the observed data in Figure 6.1a on Page 121. Weaker storms have a larger number of temperatures < 220 K, stretching farther and farther to the ocean temperature of about 300 K. A peak can be seen at around 270–300 K, which is not seen in observations, but that is a consequence of this analysis method. The CWM-based cloud top does not include the effects of water vapor absorption in the lower atmosphere for storms with little convective activity. If one were to include that effect, those temperatures would be lower.

What is missing from the results is the systematic increase in distribution mode for with decreasing storm intensity. That feature was very clear in the observations, but is seemingly absent in the model. This suggests that it is too easy for weak storms to attain high large-scale outflow. That is consistent with the findings of prior sections that the downdrafts appear to be missing from the model, as downdrafts are critical to arresting the vertical development of convection cells.

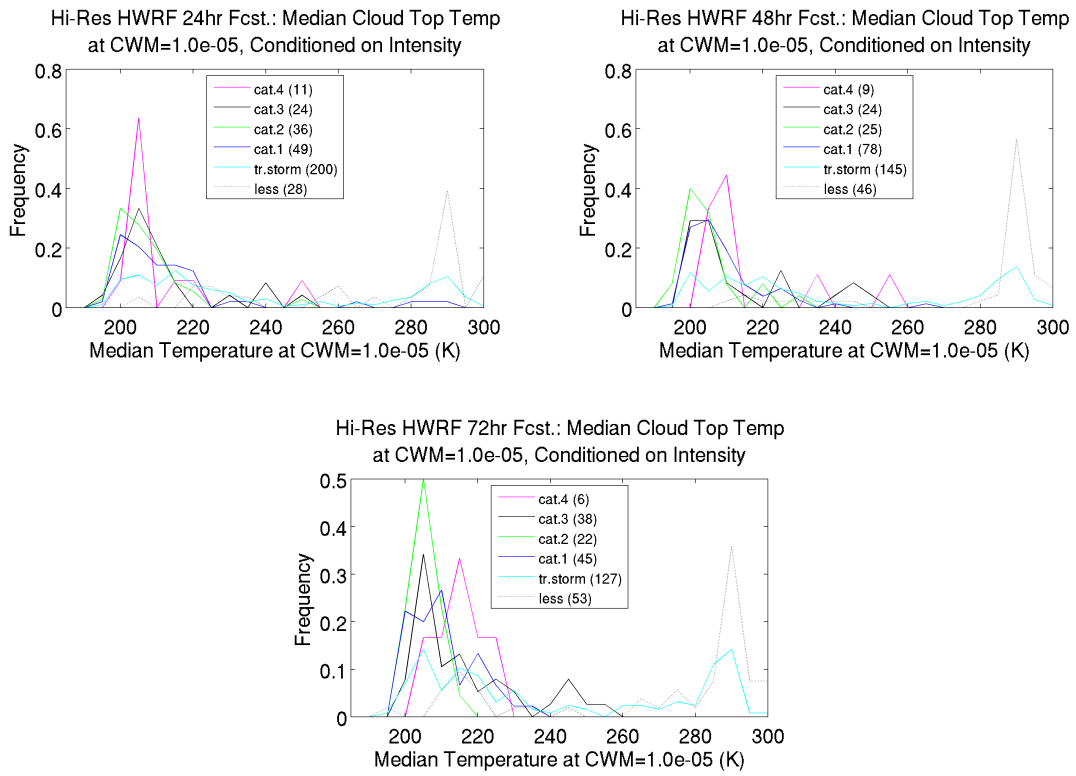


Figure 9.1: Median cloud top temperature from 2010 North Atlantic basin simulations of the high-resolution HWRf model, conditioned on Saffir-Simpson category. Top left (9.1a): 24 hr forecast, top right (9.1b): 48 hr, bottom (9.1c): 72 hr.

9.3 Cloud Tops: Peak Convection and Intensity

Recall that Section 6.2 analyzed the peak (1st percentile) cloud top temperature by conditioning on storm intensity. Results of that observational study are seen in Figure 6.2a on Page 122. The same analysis is now repeated with the model in a similar manner to the last section. Figure 9.2 shows the peak (1st percentile) cloud top temperature at the 24 hr forecast (48 and 72 hr forecasts have similar results).

It is expected from observations that the mode and width of the distribution will not significantly vary with intensity, except for storms below the tropical storm threshold. In these model results, the well-sampled tropical storm level of intensity has a wider distribution with a mode at a higher brightness temperature (lower altitude cloud top) than other intensities. That indicates that the weaker storms are having trouble producing the undilute updrafts seen frequently in observations of weak storms.

9.4 Cloud Tops: Rapid Intensification

A previous chapter, in Section 6.2, presented an analysis of TRMM observations that showed the dependence of peak (1st percentile) cloud tops on current or future rapid intensification (RI) (Figure 6.3a). RI was defined there as an increase in intensity of 30 knots or more sometime in the 36 hrs after the overpass. The same RI threshold was used for the model, but the forecast intensity is used rather than the Best Track intensity. Results are shown in Figure 9.3 for forecast hour 24. Forecast hour 48 has 21 cases, and similar results, but later hours have almost no

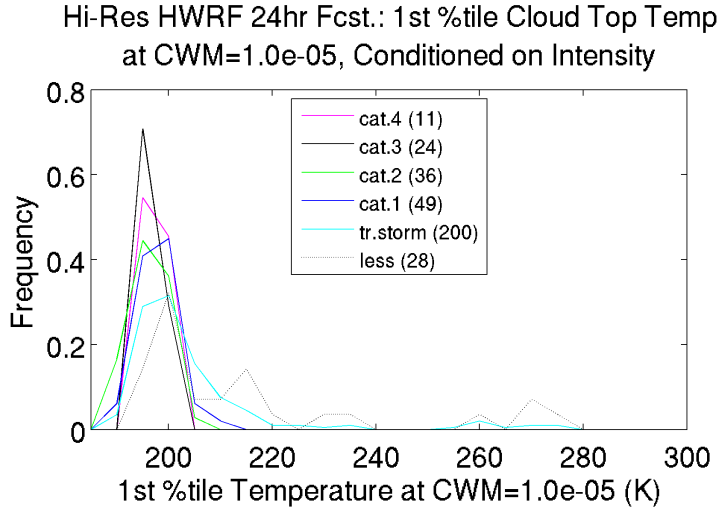


Figure 9.2: Peak (1st percentile) cloud top temperature from 2010 North Atlantic basin simulations of the high-resolution HWRF model, conditioned on Saffir-Simpson category at 24 hr forecast.

RI cases (72 hr forecast has 2 RI cases).

The expected result from observations is that the RI cases will have a strongly peaked distribution near tropopause temperatures, while non-RI cases will have a wider distribution with a peak just below tropopause temperatures, a skew toward higher brightness temperatures. Most critically, none of the observed RI cases had a peak (1st percentile) $10.8 \mu m$ brightness temperature < 205 K, while many of the non-RI cases did.

With the model, there aren't enough RI cases to establish the mode of the distribution with certainty, but other aspects of the distribution can be analyzed. All of the RI cases are near tropopause temperature, while non-RI has a wider distribution skewed far into higher brightness temperatures. Reassuringly, none of the RI cases had brightness temperatures < 205 K, while many of the non-RI cases

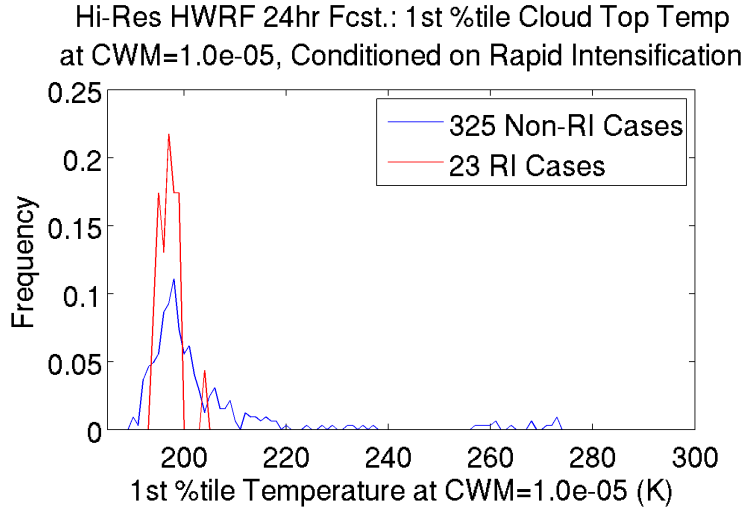


Figure 9.3: Peak (1st percentile) cloud top temperature from 2010 North Atlantic basin simulations of the high-resolution HWRF model, conditioned on RI versus non-RI at 24 hr forecast.

do. This agreement with observations suggests that hot towers involved in RI in the real world are also present in high-resolution HWRF.

9.5 Results and Discussion

This chapter analyzed model cloud top temperatures, conditioned on forecast intensity and forecast rapid intensification (gain of 30 knots or more in 36 hrs or less). This was compared to a similar analysis on TRMM VIRS $10.8 \mu m$ brightness temperatures from Chapter 6.

The $CWM = 10^{-5}$ cutoff cloud top temperatures seem to compare quite well to observations. The dependence of 1st percentile cloud top temperature on intensification agrees well with observations, though not enough RI cases exist to evaluate

the mode of the distribution. There is little dependence of peak (1st percentile) cloud top temperature on intensity except for weaker storms, indicating that a mechanism for generating strong localized convection exists in HWRF, as with the real world. However, there appears to be some dependence of the lowest cloud top temperature on intensity for tropical storm threshold cyclones, suggesting that weaker storms are having more trouble producing hot towers than observed storms do. The median brightness temperature, a measure of overall outflow height, compares well to observations with one problem. There is dependence of the mode of the distribution on intensity except for the very weakest of storms, suggesting that the overall outflow is higher than it should be.

The results of a comparison with model cloud tops corroborates the concerns about both updrafts and downdrafts. A lack of a dependence of the mode of the distribution of median cloud top temperatures for Hurricane strength storms indicates that the model is producing too much high-level outflow in stronger storms, suggesting downdrafts are not present to reduce the strength of upper outflow. Also, the mode of the peak (1st percentile) cloud top temperature does not have an expected dependence on intensity, as is seen in observations for the very weakest of storms. This indicates that updrafts are too strong in HWRF in weaker storms and downdrafts are too weak in stronger storms.

However, apart from that, the cloud tops in HWRF seem to match the real world fairly well. The median cloud top has a strong dependence on intensity, with hurricane strength storms having near-tropopause cloud tops and weaker storms having a wide distribution of median cloud tops. Storms of all strength are able to

generate upper tropospheric, and usually near-tropopause, peak convection. Also, the expected dependence of peak convection temperature on rapid intensification is present. This indicates that, while the model may have some problems, the top of convection is largely correct despite the low resolution.

Chapter 10

Conclusions and Future Work

The primary goal of this thesis was to develop methods for analyzing in-situ and satellite observations of tropical cyclones to provide guidance for diagnosing small scale variability in hurricane models. By applying the same or similar analysis methods to observational data and model output, one can determine whether models' near-convective scales match those seen in real tropical cyclones. This work also lays the groundwork for future investigations into the small scale dynamical processes that play a role in tropical cyclone intensity.

10.1 Summary and Conclusions

The work in this thesis was a blend of observational and computational work. The observational part of the research was aimed at finding statistical signatures of small-scale dynamical processes that were independent of storm. This was applied to the problem of creating model diagnostics for high resolution models. If there are any statistical properties that are found in all storms, then the simulated storm should have these same features even if the large scale structure of the simulated storm is very different from the real storm. Several statistical features of this type were found. The vertical wind was found to be scale invariant below a few km, and the correlation in the vertical wind between two points approaches zero beyond a

transition scale in the range 1–5 km, corresponding to correlation lengths around 500 m to 3 km. Increments in vertical velocity field, normalized by the structure function, have a Gaussian core, and were usually Weibull in the tails, but were sometimes Gaussian throughout. The radial increments in the radial wind were used to approximate the longitudinal structure function for which analytical results are available from turbulence theory. The radial wind displayed a power law spectrum of $S_2(\Delta s; v_r) \propto \Delta s^p$. The most probable value of p over many flight segments was 0.85 in saturated regions, and 0.95 in unsaturated regions. This rules out the standard models of isotropic 2D and 3D turbulence, which predict slopes of 2 and 2/3. The slope $p \propto 1$ is more consistent with other types of turbulence such as rotating, stratified turbulence or gravity waves. A linear structure function of radial wind ($S_2(\Delta s; v_r) \propto \Delta s$) was also found in the range 10–50 km when all storms' data were combined into one structure function. This is also consistent with rotating, stratified turbulence or gravity waves, but could also arise from steep, ledge-like structures in the data that lead to a spectral density of k^{-2} . This relationship is not always seen in any single storm's structure function, so this may be a measure of typical rainband and eyewall sizes and spacing, or the 10–50 km may simply not be well-sampled enough on a per-storm basis. Even extremely well-measured storms such as Hurricane Bonnie (1998) did not show this scaling, so that suggests the former. In any case, this research has generated some interesting questions that can be further explored.

A theoretical construct, the *Utopian Model*, was created in order to estimate how the storm intensity, which is defined in terms of a maximum wind, depends

on model resolution. To simulate model grid resolution, high resolution aircraft observations were averaged and subsampled in a finite difference grid. As one lowers the resolution of this Utopian Model, the gridpoint-scale maximum wind decreases. This effect is not related to unresolved dynamics, but is simply due to the resolution of the grid. This underestimation of the maximum wind is larger for stronger storms, for slower-moving storms, and for lower-resolution models. Large dropoffs in the maximum wind estimate are found for resolutions of around 10 km and lower, and little difference is seen for resolutions higher than 1 km.

Other observational work included the creation and analysis of a database of 2081 TRMM satellite overpasses of 827 tropical cyclones. This database has potential well beyond what it was used for in this thesis. A statistical analysis of data from the TRMM satellite revealed relationships between $10.8 \mu m$ brightness temperatures (T_b), storm intensity and rapid intensification. Storms with a higher intensity had a higher altitude (lower temperature) median brightness temperature, an analogue for storm-scale outflow. All storms, regardless of intensity or intensification rate, were able to produce near-tropopause 1st percentile T_b to some extent. However, 1st percentile T_b are lower for RI cases though, as those cases never had a higher 1st percentile T_b than 205 K, whereas about 50% of non-RI cases had higher T_b than that. These results suggest that the lowest observed brightness temperatures could be a useful predictor of storm intensification. This has been suggested before, but in more limited studies. In addition, this work was found to be useful in diagnosing the high resolution hurricane simulations that were also part of this research.

The research presented in this thesis also included the development of a high-resolution version of a hurricane forecast model (NCEP HWRF), that is now being considered for the 2012 version of operational HWRF. During this development work a major problem was identified with the implementation of the model microphysics that was leading to large amounts of spurious latent heating; this had to be addressed before the model was suitable for use in this research. The nature of the bug, and comparison to observations, led to the discovery of another problem, i.e. that the model downdrafts were not being represented correctly. The model diagnostics developed from the observations proved to be useful in diagnosing these problems.

Model cloud top temperature from over 300 simulations were analyzed and results compared to those from TRMM T_b . Simulated tropical storm strength cyclones were sometimes unable to generate high peak convection. Other than that, correct intensity vs. large scale outflow and intensity vs. peak outflow was seen. Also, the correct RI vs. peak cloud top relationship was found: peak cloud top temperatures for RI cases were never below 205 K, whereas non-RI cases frequently had cloud top temperatures below that.

Analyzing the 1035 simulations using methods similar to those of Chapter 4 found a rapid growth of 3 km structure in the first 6 hrs in some storms, pushing up the intensity by as much as 15 m/s. In other cases, all three domains weakened uniformly, and rapidly, by as much as -15 m/s. These issues are likely due to the lack of a proper 3 km resolution initialization.

Overall, the research presented in this thesis has demonstrated the value of statistical diagnostics for high-resolution models. In addition, this research presents

a framework for a deeper investigation of tropical cyclone small-scale dynamics.

10.2 Future Directions

The analysis methods and TRMM database developed in this thesis have potential well beyond the research shown. The in-situ scale analysis has a lot of potential for analyzing the relationships between turbulent scales and storm scales using ideas from other areas. In particular analytical, modeling and empirical studies of anisotropic, stratified turbulence in a rotating flow produce the same power law exponent of 1 seen in radial wind, as well as lower exponents for smaller scales (Mahalov and Zhou, 1996; Yeung and Zhou, 1998; Hattori et al., 2004), so they may reveal more about small-scale dynamics.

Extending the in-situ analysis method to other data sources will allow a better characterization of smaller scales (40Hz in-situ data, SFMR), azimuthal and vertical variation (EDOP Doppler radar, HRD quasi dual Doppler radar, dropsondes). With that, the effect of tangential averaging on the drop of the wind maximum (Utopian Model) can be estimated. In addition, if the shear and convective turbulent cascades are critical to the formation of towers and mesovortices and if that is important for intensity, then this future work should help to shed light on that.

The satellite overpass database can be extended, as can the analysis performed on it. A more sophisticated conditioning on RI, such as N hours before (for various N), or during intensification; and the strength of the rapid intensification, could give information about what happens over the course of a rapid intensification event.

Similar analyses could be done for other situations: landfall, shear-induced weakening, etc. This overpass database and extensions to it will be a useful tool to tropical cyclone researchers. The use of WMO best track will provide storm fixes more often, and hence allow more overpasses to be detected. More satellites can be added and this work is partially done. The Terra satellite, for example, has over twelve thousand overpasses of tropical cyclones, which will allow for more statistically robust investigations under different conditions. Other TRMM products can be added (microwave imager, level 2 derived products and more of the infrared and visible channels). Distributing this data in a publicly-accessible manner would assist tropical cyclone research.

From the analysis of the high-resolution HWRF model, it is clear that there is work to be done. A full 3km initialization scheme is needed to eliminate the initial sudden gains of intensity, and a correction to the sudden intensity drops will require initialization modifications as well. The cause of the lack of downdrafts in the model, such as the microphysics or the reversion to hydrostatic state after a nest move, need to be further explored.

Appendix A

Numerical Prediction of Hurricanes

This thesis uses observational data to test model assumptions, and hence a “test case” model is used for comparison. In particular, the high-resolution version of the HWRF model is used. The high-resolution version of HWRF is hoped to be the 2012 version of the NCEP Operational HWRF, but that is subject to resource availability. (The model currently takes three times the available resources, but much effort is going into speeding it up.)

This appendix describes the HWRF model, and gives a brief overview of its parent global model GFS. There are small differences between high-resolution HWRF and the current operational, which will be highlighted throughout this appendix. The HWRF model is run operationally in real-time by the National Centers for Environmental Prediction (NCEP) and is used by the National Hurricane Center (NHC) for model guidance. The parent global model that provides input and boundary conditions is the NCEP Global Forecasting System (GFS), a global spectral model used by NCEP for all of its global modeling needs. That model is also used as the initial and boundary conditions for most HWRF configurations (and most other NCEP regional models as well), including the operational HWRF.

Both the GFS and HWRF models, as well as several others, use the Gridpoint Statistical Interpolation (GSI) 3DVAR data assimilation system for initializing the

model with observational data. Unfortunately, the GSI as used at NCEP discards all radiance-based measurements in the presence of clouds, rendering it useless for initializing hurricanes, but still useful for initializing the environment.

To get around that problem, the HWRF also uses a vortex relocation and bogussing system that can move the GFS vortex, modify its intensity, or add in a simple axially-symmetric vortex (called *bogussing*) if no vortex is present. In addition, the HWRF initialization uses the previous six-hour forecast model fields to initialize the current forecast. The GFS makes use of some of the same vortex relocation features as well.

This appendix will provide an overview of the GFS and HWRF models as well as other relevant utilities.

A.1 The Global Forecasting System

The GFS model is a global spectral hydrostatic model that runs at approximately a 27km resolution and uses GSI 3DVAR data assimilation. The model is only spectral in the latitude-longitude direction, and is discrete in the temporal and vertical direction. The discretization of the vertical starts with pure sigma levels at the ground, fading linearly to pure pressure-levels in the upper troposphere and beyond. The model is initialized from the prior six-hour GFS forecast, which is run through the GSI data assimilation program. GFS runs a 168 hour (7 day) forecast at full resolution, and then a decreased resolution up to 384 hours (14 days). The dynamical core (thermodynamics and advection) is fully spectral, but the convec-

tion scheme, gravity wave drag scheme, and other parameterizations are all run on a linear Gaussian grid instead of spectral space. The GSI data assimilation is run at a slightly lower-resolution reduced Gaussian grid due to limited available computation time. The model is transformed back to the full (non-reduced) Gaussian grid for post-processing. Those files are processed by the NCEP Unified Post-Processor to produce various prognostic and diagnostic variables at model resolution in the so-called GFS “master GRIB files.” The NCEP copygb program is then used to interpolate to produce global gridded analysis and forecast files.

More explicitly, the model interface levels are defined as:

$$\eta(0, p_s) = 0 \tag{A.1}$$

$$\eta(p_s, p_s) = 0 \tag{A.2}$$

$$\eta_{k+1/2} = A_{k+1/2}/p_0 + B_{k+1/2} \tag{A.3}$$

where p_s is the surface pressure, p_0 is 101325 Pa and $A_{1/2} = B_{1/2} = 0$. The pressures are hydrostatic since GFS is a purely hydrostatic model. Mass levels consist of mass quantities (T , ρ , q , etc.) integrated between the two adjacent interface levels. The prognostic variables solved by the dynamical core are horizontal wind, virtual temperature, water vapor and liquid water mixing ratios, density, and $d\eta/dt$, while a variety of other variables are solved prognostically by the parameterizations.

A.2 Hurricane Weather Research and Forecasting System

The main focus of this thesis is using observational data to test assumptions made by hurricane models, for which HWRF will act as a case study. Hence, this section analyzes HWRF in somewhat more detail than GFS. The next section will discuss initialization of HWRF, and to some extent, initialization of GFS as well.

The HWRF takes GFS data as input and boundary conditions, and solves the equations of motion of the atmosphere and ocean to produce a more accurate track and intensity of one storm at a time. HWRF's simulation consists of an approximately 20 km resolution Princeton Ocean Model (POM) coupled to the Weather Research and Forecasting Model Nonhydrostatic Mesoscale Model (WRF-NMM) using the NCEP coupler. Sometime in the future, the POM component is expected to be replaced by the higher-resolution HyCOM ocean model. Additionally, a wave model Wavewatch 3 and a bay and estuary model will eventually be added.

The WRF-NMM dynamical core present in HWRF is modified to have support for an inner, moving domain (and the current developmental version has support for a second moving domain within that one). The moving domain has exactly three times the resolution of the parent in the horizontal and temporal directions, but the exact same vertical levels (and hence resolution) as the parent. This moving domain has 9 km resolution and follows the storm. The high-resolution HWRF has a second moving domain at 3 km resolution within the 9 km domain.

The horizontal grid for the atmospheric component of HWRF is a rotated latitude-longitude, semistaggered Arakawa E grid. The *rotated latitude-longitude*

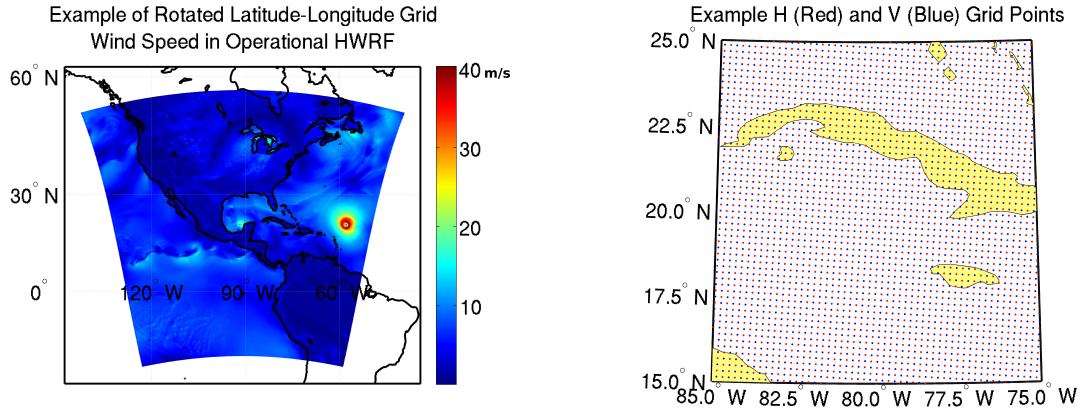


Figure A.1: Left: an example of the rotated latitude-longitude grid. Right: the same grid, zoomed in on the Carribean. H (mass) grid points are in red and V (velocity) grid points are in blue.

projection simply takes an equatorial point in the ordinary latitude-longitude system, and rotates the entire system to place that point a certain number of degrees north or south of the equator. The rotated latitude-longitude projection used in WRF-NMM rotates the equatorial point such that it is in the middle of the outer computational domain. That is done to reduce the warping of grid edges as little as possible, and also presents some computational benefits.

In that that rotated latitude-longitude projection, the WRF-NMM is placed on a semistaggered Arakawa E grid. An example grid is shown in Figure A.1.

The “H” points make up the *H grid* (sometimes called the mass grid). On non-interface layers, the mass gridpoints contain all values except for wind and pressure. On interface layers, the H grid points contain vertical wind values. The V gridpoints make up the *V grid* (or velocity grid), which contains horizontal wind on the non-interface levels, and is unused on the interface levels.

The WRF-NMM vertical coordinate is a mass-based, terrain-following coordinate that is very similar to that of GFS, but with one complication due to the non-hydrostatic nature of the model. The WRF-NMM vertical coordinate is based on the hydrostatic pressure, usually written as π , but will be written as \mathbf{p} in this appendix to avoid confusion. The full non-hydrostatic pressure is p , and is allowed to vary on the model grid (so $p = p(x, y, \mathbf{p}, t)$).

The model levels start with a terrain-following coordinate near the surface, fades linearly to a constant-pressure coordinate at a pressure \mathbf{p}_i , and then remains constant-pressure until the model top pressure \mathbf{p}_t . For that reason, we will define μ and $\mu_{\mathbf{p}}$:

$$\mu \equiv \mathbf{p}_s - \mathbf{p}_i \tag{A.4}$$

$$\mu_{\mathbf{p}} \equiv \mathbf{p}_t - \mathbf{p}_i \tag{A.5}$$

where both must be larger than zero. The equation for $\mathbf{p}(x, y, \eta, t)$ is then:

$$\mathbf{p} = \mathbf{p}_t + \eta_1(\eta)(\mathbf{p}_i - \mathbf{p}_t) + \eta_2(\eta)\mu \tag{A.6}$$

where η scales from 1 at the ground to 0 at \mathbf{p}_t . Note that \mathbf{p} is a monotonic function of η . As you can see above, WRF-NMM model has a terrain-following coordinate, unlike the Eta model. That results in the model levels being flat away from and far above mountains, but terrain-following and at higher vertical resolution in the vicinity of mountains. The $\eta_1(\eta)$ and $\eta_2(\eta)$ are weights used to control the

density of the levels in the terrain-following and constant-pressure regions, similarly to the $A_{k+1/2}$ and $B_{k+1/2}$ of GFS. The vertical coordinate will be explained further in the next section.

Simulation of the atmosphere on this grid is split into the software framework, which handles inter-process communication and disk I/O; the dynamical core which solves the system of equations of a dry atmosphere, and some of the simpler aspects of the thermodynamics; and the parameterizations which deal with aspects of the atmosphere that cannot be handled through the dynamical core (hydrometeor effects, radiation, convection, boundary layer, soil, etc.) The next subsection will explain the relevant aspects of the software framework, the second section will explain the dynamical core, and the final section will discuss the parameterizations.

A.2.1 HWRF Framework

The dynamical core and surrounding software framework loops through this sequence of events until the simulation is complete:

1. Handle boundary and initial conditions.
2. Call all dynamical solver and parameterization routines, and communicate with the ocean model. The dynamical solver has the power to decide when each parameterization is called and when the SST is updated.
3. Communicate with any nests.
4. Handle nest motion.

5. Recurse into nests. This entire loop is repeated for all nests three times (since nest timesteps are one third of parent domain timesteps).

Note that nested domains can contain further nested domains, in which case the solver will recurse into nests of nests in a depth-first-search ordering.

Nest motion is problematic in HWRF because the non-hydrostatic state of the nest is discarded upon nest motion, resulting in small amounts of non-conservation of mass and energy in the system in an otherwise mass- and energy-conserving model, and creation of powerful, temporary gravity waves. Fortunately, the simulation appears to normalize completely in less than nine minutes when run at up to three times operational resolution.

A.2.2 HWRF Dynamical Core

I will now describe the equations solved by the dynamical core. The atmosphere is split into two regions: an upper region with constant hydrostatic pressure surfaces and a lower region with constant σ surfaces. Here, σ has its typical definition:

$$\sigma \equiv \frac{\mathbf{p} - \mathbf{p}_i}{\mu} \tag{A.7}$$

For convenience, we will express the constant pressure region of the model as another sigma space. To do that, we use a “surface pressure” of the constant value \mathbf{p}_i and define:

$$\sigma_{\mathbf{p}} \equiv \frac{\mathbf{p} - \mathbf{p}_t}{\mu_{\mathbf{p}}} \quad (\text{A.8})$$

Note that in the $\sigma_{\mathbf{p}}$ space, the “surface pressure” of that space is simply the constant value \mathbf{p}_i . We can now relate these σ spaces to the $\eta_1(\eta)$ and $\eta_2(\eta)$ mentioned earlier:

$$\eta_1(\eta) = \begin{cases} 0 & \eta < 0.4 \\ \sigma((\eta - 0.4)/0.6) & \eta \geq 0.4 \end{cases} \quad (\text{A.9})$$

$$\eta_2(\eta) = \begin{cases} \sigma_p(\eta/0.4) & \eta < 0.4 \\ 0 & \eta \geq 0.4 \end{cases} \quad (\text{A.10})$$

As with HWRF, if WRF-NMM is run in non-hydrostatic mode, the ε variable is introduced, and $p \neq \mathbf{p}$. The ε is defined as:

$$\varepsilon \equiv \frac{dw}{dt} \frac{1}{g} \quad (\text{A.11})$$

The quantity ε is a prognostic variable, which allows vertical wind to be a diagnostic variable. Also, this allows the non-hydrostatic portions of WRF-NMM to be turned off simply by setting ε to 0.

The equations that are solved by the WRF-NMM dynamical core are described in the next two sections. The use of ε allows for the model to be divided into “general” equations and equations that solve for the non-hydrostatic terms.

A.2.2.1 WRF-NMM Solver

This section describes the equations solved by the WRF-NMM, except for the ones specific to the non-hydrostatic state. The σ or \mathbf{p} subscripts in these equations indicate the vector or gradient is on a constant sigma or constant hydrostatic pressure surface (in either case, a model level). The $f(x, y)$ is the local f-plane approximation to the Coriolis force within that grid square, and Φ is the geopotential. Note that WRF-NMM uses an f-plane approximation, but each grid point is given its own f value.

The equation of state:

$$\alpha \equiv 1/\rho = \frac{RT}{p}(0.608q - q_c + 1) \quad (\text{A.12})$$

where *alpha* is the specific volume, ρ is the total mass density (including condensates and vapor), T is temperature, R is the gas constant for dry air, q is the water vapor mixing ratio and q_c is the condensate mixing ratio.

Next, the momentum equation in sigma and pressure space:

$$\frac{\partial \vec{v}_\sigma(x, y, \sigma, t)}{\partial t} = -\vec{v}_\sigma \cdot \nabla_\sigma \vec{v}_\sigma - \frac{d\sigma}{dt} \frac{\partial \vec{v}}{\partial \sigma} - (1 + \varepsilon) \nabla_\sigma \Phi - \alpha \nabla_\sigma p + f(x, y) \hat{k} \times \vec{v} \quad (\text{A.13})$$

$$\frac{\partial \vec{v}_{hypr}(x, y, \mathbf{p}, t)}{\partial t} = -\vec{v}_\mathbf{p} \cdot \nabla_\mathbf{p} \vec{v}_\mathbf{p} - \mu_p \omega \frac{\partial \vec{v}}{\partial \mathbf{p}} - (1 + \varepsilon) \nabla_\mathbf{p} \Phi - \alpha \nabla_\mathbf{p} p + f(x, y) \hat{k} \times \vec{v} \quad (\text{A.14})$$

where ω is the pressure vertical velocity:

$$\omega \equiv \frac{dp}{dt} \quad (\text{A.15})$$

Note that the vertical velocities ω and $\frac{d\sigma}{dt}$ use the non-hydrostatic state.

The hydrostatic continuity equation in sigma and pressure space:

$$\frac{\partial \mathbf{p}}{\partial t} = -\nabla_{\sigma} \cdot \vec{v}_{\sigma} - \frac{\partial \mu \frac{d\sigma}{dt}}{\partial \sigma} \quad (\text{A.16})$$

$$0 = -\nabla_{\sigma} \cdot \vec{v}_{\sigma} - \frac{\partial}{\partial \mathbf{p}} \frac{\partial \mathbf{p}}{\partial t} \quad (\text{A.17})$$

and at the interface between pressure and sigma space:

$$\mu \frac{\partial \sigma}{\partial t} = \frac{\partial \mathbf{p}}{\partial t} \quad (\text{A.18})$$

Temperature tendency:

$$\frac{\partial T}{\partial t} = -\vec{v} \cdot \nabla_{\sigma} T - \frac{\partial \sigma}{\partial t} \frac{\partial T}{\partial \sigma} + \frac{\alpha}{c_P} \left(\frac{\partial p}{\partial t} + \vec{v} \cdot \nabla_{\sigma} p + \frac{d\sigma}{dt} \frac{\partial p}{\partial \sigma} \right) \quad (\text{A.19})$$

A.2.2.2 Non-Hydrostatic Solver

As discussed earlier, all variables are on a 3D grid whose vertical coordinate is defined based on the hydrostatic pressure. Included among those variables are the non-hydrostatic pressure $p(x, y, \mathbf{p}, t)$ (a prognostic variable), the non-hydrostatic vertical velocity (a diagnostic variable), and ε (a prognostic variable). Determining those variables is the job of the WRF-NMM non-hydrostatic module. In addition, the non-hydrostatic module add perturbations to Φ and $\frac{d\sigma}{dt}$.

The non-hydrostatic solver applies to the entire height of the model: both sigma-level and pressure-level regions. One can describe the resulting equations by re-expressing everything in the full η coordinate discussed earlier. However, the physics of the situation is the same in either case. (Recall that the pressure-level region is also sigma-level with a constant “surface” pressure of \mathbf{p}_i .) Hence, for brevity, the σ equations are shown here. For a similar reason, this derivation omits the density corrections for moisture and water vapor.

The non-hydrostatic solver relates the hydrostatic and non-hydrostatic states by assuming that the non-hydrostatic part of the geopotential is very small compared to the hydrostatic part. The other variables are allowed to be fully non-hydrostatic, and are defined on constant hydrostatic pressure or constant hydrostatic sigma model levels. An approximation is made in the momentum equation to relate the non-hydrostatic geopotential back to the approximate pseudo-hydrostatic one. The key variable in all of this is the prognostic ε variable which will be explored further in this section.

Given a box of mass M , density ρ , vertical cross-section S , and pressure p from above it,

$$Mg = pS \tag{A.20}$$

expanding p into its hydrostatic and non-hydrostatic perturbation parts:

$$g\rho S\Delta z = \mathbf{p}S + p'S \tag{A.21}$$

where p is the non-hydrostatic pressure. We then assume that, for the purposes of geopotential,

$$p' \ll \mathfrak{p} \tag{A.22}$$

giving us:

$$g\rho S\Delta z = \mu\Delta\sigma S \tag{A.23}$$

We can rearrange terms to produce:

$$-\frac{g\Delta z}{\mu\Delta\sigma} = -1/\rho \tag{A.24}$$

or,

$$-\frac{g\Delta z}{\mathfrak{p}} = -1/\rho = -\alpha \tag{A.25}$$

which, at the limit of infinitely small volume, becomes

$$\frac{\partial\Phi}{\partial\mathfrak{p}} = -\alpha \tag{A.26}$$

The non-hydrostatic solver determines Φ from integrating the non-hydrostatic p in a model column:

$$\begin{aligned} \Phi &= \Phi_s + \mu \int_0^1 \alpha d\sigma \\ &= \Phi_s + \mu \int_0^1 \frac{RT}{p} d\sigma \end{aligned} \tag{A.27}$$

where Φ_s is the surface geopotential, and is constant.

Note that Φ is not the actual geopotential due to the approximation $p' \ll \mathbf{p}$. It is also not the hydrostatic geopotential since the full, non-hydrostatic p is integrated to produce it. Instead, it is an approximate, pseudo-hydrostatic geopotential. The following approximation is used to replace the non-hydrostatic geopotential Φ_{nh} in the momentum equation:

$$\nabla_{\sigma} \Phi_{nh} \approx (1 + \varepsilon) \nabla_{\sigma} \Phi \tag{A.28}$$

Effectively, what we have done is recalculate an almost hydrostatic geopotential based on the non-hydrostatic pressure, and then substituted that back in to the non-hydrostatic equations of motion with the $1 + \varepsilon$ corrective factor to equate it to the non-hydrostatic geopotential. Hence, the non-hydrostatic state can exist, so long as it doesn't grow large enough to violate our "pseudo-hydrostatic" assumption that the non-hydrostatic contributions to the geopotential are small. This has been found to work well even at very non-hydrostatic situations with 100m resolution simulations.

Next, we need the non-hydrostatic pressure p , which is determined from the definition of our prognostic variable ε :

$$\frac{\partial p}{\partial \mathbf{p}} = 1 + \varepsilon \tag{A.29}$$

The non-hydrostatic pressure $p(x, y, \mathbf{p}, t)$ at a given hydrostatic pressure \mathbf{p} is then:

$$\begin{aligned}
p &= \int_{\mathbf{p}_s}^{\mathbf{p}} (1 + \varepsilon) d\mathbf{p} \\
&= \int_0^\sigma (1 + \varepsilon) \mu d\sigma
\end{aligned}
\tag{A.30}$$

Next we define our height and vertical velocity coordinate:

$$z_g \equiv \frac{\Phi_{nh}}{g} \tag{A.31}$$

and:

$$w_g \equiv \frac{1}{g} \frac{d\Phi_{nh}}{dt} \tag{A.32}$$

where g is constant in WRF-NMM. The third component of the momentum equation, without viscous friction terms or non-local mixing (which are handled by other model modules), is:

$$\frac{dw_g}{dt} = -g - \alpha \frac{\partial p}{\partial z} \tag{A.33}$$

rewriting the derivative in terms of \mathbf{p} ,

$$\frac{dw_g}{dt} = -g - \alpha \frac{\partial p}{\partial \mathbf{p}} \frac{\partial \mathbf{p}}{\partial z} \tag{A.34}$$

By the hydrostatic approximation and definition of α , we can simplify the term involving the hydrostatic pressure \mathbf{p} , resulting in:

$$\frac{1}{g} \frac{dw_g}{dt} + 1 = \frac{\partial p}{\partial \mathbf{p}} \tag{A.35}$$

from the definition of ε ,

$$\frac{\partial p}{\partial \mathbf{p}} = 1 + \varepsilon \quad (\text{A.36})$$

expanding the derivative into components,

$$\frac{\partial p'}{\partial \mathbf{p}} + \frac{\partial \mathbf{p}}{\partial \mathbf{p}} = 1 + \varepsilon \quad (\text{A.37})$$

or,

$$\frac{\partial p'}{\partial \mathbf{p}} = \varepsilon \quad (\text{A.38})$$

Hence, the ε provides the non-hydrostatic contribution to the full non-hydrostatic pressure. There is another way to rewrite the above equations to let us determine the non-hydrostatic pressure at any height:

$$\partial p = (1 + \varepsilon) \partial \mathbf{p} \quad (\text{A.39})$$

Next, we assume:

$$p(x, y, \mathbf{p}_t, t) = \mathbf{p}_t \quad (\text{A.40})$$

We can then integrate $1 + \varepsilon(x, y, \mathbf{p}, t)$ from the model top down to any model level to get $p(x, y, \mathbf{p}, t)$:

$$p(x, y, \mathbf{p}, t) = \int_{\mathbf{p}_t}^{\mathbf{p}} (1 + \varepsilon) \partial \mathbf{p} \quad (\text{A.41})$$

We must now determine the pressure vertical velocity ω and sigma vertical velocity $\frac{d\sigma}{dt}$, which are used for vertical advection in pressure and sigma space, respectively. We will define for convenience:

$$\dot{\sigma}(x, y, \sigma, t) \equiv \frac{d\sigma(x, y, \sigma, t)}{dt} \quad (\text{A.42})$$

Note that $\dot{\sigma}$ is dependent only on the hydrostatic pressures, due to the definition of the sigma coordinate system. Hence, $\dot{\sigma}$ can be determined from the time tendency of μ .

In deriving the three required quantities, we start with the non-hydrostatic continuity equation:

$$w_g = \frac{1}{g} \left(\frac{\partial \phi}{\partial t} + \vec{v}_\sigma \cdot \nabla_\sigma \Phi + \frac{\partial \sigma}{\partial t} \frac{\partial \Phi}{\partial \sigma} \right) \quad (\text{A.43})$$

and the hydrostatic continuity equation mentioned earlier, which we can rewrite as:

$$\frac{d\mu}{dt} + \mu \left(\nabla_\sigma \cdot \vec{v}_\sigma + \frac{\partial \dot{\sigma}}{\partial \sigma} \right) \quad (\text{A.44})$$

we will also specify these boundary conditions. For the upper, pressure-level regime:

$$\dot{\sigma}(x, y, 0, t) = 0 \quad (\text{A.45})$$

and for the lower, sigma-level regime:

$$\dot{\sigma}(x, y, 1, t) = 0 \quad (\text{A.46})$$

With those conditions, we can expand the $\frac{d\mu}{dt}$, simplify and integrate to produce the tendency for the hydrostatic pressure depth:

$$\frac{\partial \mu}{\partial t} = - \int_0^1 \nabla_{\sigma} \cdot (\mu \vec{v}') d\sigma' \quad (\text{A.47})$$

and the sigma vertical velocity:

$$\mu \dot{\sigma} = -\sigma \frac{\partial \mu}{\partial t} - \int_0^{\sigma} \nabla_{\sigma} \cdot (\mu \vec{v}') d\sigma' \quad (\text{A.48})$$

Determining the ω term requires the first law of thermodynamics

$$c_p \frac{dT}{dt} = \alpha \frac{dp}{dt} = \alpha \omega \quad (\text{A.49})$$

The complication in this is the Lagrangian derivative of the non-hydrostatic pressure on hydrostatic pressure coordinates. The way WRF-NMM deals with that is:

$$\begin{aligned} \frac{\partial p}{\partial t} &= \left(\frac{\partial p}{\partial \varepsilon} \right)_t \frac{\partial \varepsilon}{\partial t} \\ &= (1 + \varepsilon) \frac{\partial \varepsilon}{\partial t} + \left(\frac{\partial p}{\partial t} \right)_{\varepsilon} \end{aligned} \quad (\text{A.50})$$

Based on that, we will expand ω into:

$$\omega \equiv \frac{dp}{dt} = \omega_1 + \omega_2 \quad (\text{A.51})$$

where:

$$\omega_1 = (1 + \varepsilon) \frac{\partial \varepsilon}{\partial t} + \vec{v}_\sigma \cdot p + (1 + \varepsilon) \dot{\sigma} \frac{\partial p}{\partial \sigma} \quad (\text{A.52})$$

and:

$$\omega_2 = \frac{\partial p}{\partial t} - (1 + \varepsilon) \frac{\partial \varepsilon}{\partial t} \quad (\text{A.53})$$

We can use the hydrostatic continuity equation, and the fact that $\frac{\partial \sigma}{\partial p} = \mu$ to produce:

$$\omega_1 = \vec{v}_\sigma \cdot p - (1 + \varepsilon) \int_0^\sigma \nabla_\sigma \cdot (\mu \vec{v}) d\sigma' \quad (\text{A.54})$$

while, ω_2 can be shown to equal:

$$\omega_2 = \int_0^\sigma \left(\frac{\partial \varepsilon}{\partial t} \frac{\partial(\sigma' \mu)}{\partial \sigma'} - \frac{\partial(\sigma' \mu)}{\partial t} \frac{\partial \varepsilon}{\partial \sigma'} \right) \partial \sigma' \quad (\text{A.55})$$

Through a similar process, one can derive the time tendency of T , which has been expressed in the previous section.

The last quantity that must be updated in order to complete the non-hydrostatic solver is the critical quantity ε . That quantity is updated through its definition:

$$\varepsilon \equiv \frac{1}{g} \frac{dw_g}{dt} = \frac{1}{g} \left(\frac{\partial w_g}{\partial t} + \vec{v} \cdot \nabla_\sigma w_g + \dot{\sigma} \frac{\partial w_g}{\partial \sigma} \right) \quad (\text{A.56})$$

The resulting ε is then sent back to the general solver for use in solving the rest of the equations.

A.2.3 HWRF Parameterizations

A.2.3.1 Microphysics: Ferrier Scheme

The Ferrier microphysics scheme in HWRF (Developmental Testbed Center, 2010; Rogers et al., 2001) serves to model gridscale resolved microphysics. The only prognostic quantity that is advected by the model is the total condensate. The Ferrier scheme is designed with the philosophy that model gridscale advection and gridscale differences are not relevant to microphysical processes.

Three other fields, that are not advected, act as “first guess” values for determining the particular microphysics species. The ice fraction specifies the fraction of condensate in ice form. The rain fraction contains the fraction of condensate that is rain. Condensate that is not rain nor ice is assumed to be small cloud particles. A riming factor is used to determine the amount of riming present on ice particles (and hence ice particle size).

The Ferrier scheme uses the total condensate, the three “first guess” fractions and thermodynamic fields to determine the microphysics species present in each grid-box. Having that information, the scheme then models condensation, precipitation and other processes. Upon completion of the time step’s microphysics calculations, the “first guess” fields, total condensate mixing ratio and thermodynamic fields are updated and the microphysics species information is discarded.

Precipitation, condensation, sublimation are modeled internally within the Ferrier scheme, when microphysics species information is known. This allows modeling of riming, precipitation type, mixed phase conditions and also freezing and

melting processes. Condensation happens at a threshold of 97.5% relative humidity at low levels and 100% at high levels.

A.2.3.2 Convection: Simplified Arakawa Schubert

It is the job of the convection parameterization to model the effects of updrafts and downdrafts that the dynamical core cannot resolve. The Simplified Arakawa Schubert (SAS) scheme is used in the HWRF and GFS models. The high-resolution version of HWRF (discussed in Chapter 7) does not use this (or any) convection scheme in its 3 km domain, but still uses it in the 9 km and 27 km domain.

This scheme is based on the original Arakawa and Schubert (1974) scheme which considered an ensemble of clouds with many tops in each grid column. Simplifications from Grell (1993) are used to consider only one cloud top level. The GFS uses a slightly more advanced scheme than HWRF, with the capability of two cloud top levels: one for “shallow convection” and one for “deep convection,” performed by applying the single cloud top scheme twice.

The SAS scheme in HWRF triggers when the cloud work function exceeds a certain threshold. The scheme assumes the atmosphere should be in a quasi-equilibrium state, and from that assumption a cloud mass flux M_c is derived for the cloud. The cloud top level is determined by the parcel method to be the level at which the parcel becomes stable relative to the environment.

Tendencies for moist static energy and liquid water and then derived from:

$$\frac{\partial h}{\partial t} = E(h - h^\sim) + D(h^\sim - h) + M_c \frac{\partial h}{\partial z} \quad (\text{A.57})$$

and

$$\frac{\partial q}{\partial t} = E(q - q^{\sim}) + D(q^{\sim} + l - q) + M_c \frac{\partial q}{\partial z} \quad (\text{A.58})$$

where h , q and l are the moist static energy, specific humidity and liquid water, respectively, and tildes in the $E(\dots)$ refers to the entrainment layer and $D(\dots)$ to the detrainment layer. Momentum transport is also modeled, transporting momentum in the vertical similarly to heat and moisture (Pan, 2003; Han and Pan, 2006).

The cloud model includes a downdraft mechanism (whose strength is dependent on vertical shear of wind) and evaporation of precipitation. Detrainment of the downdraft and entrainment of the updraft are also included.

A.2.3.3 Surface Layer: Modified GFDL Surface Layer

A modified version of the GFDL surface layer scheme is used in HWRF. In this, the downward momentum flux τ , sensible heat flux H and water vapor flux E are evaluated from formulae:

$$\tau = \rho V_*^2 \frac{V(h)}{|V(h)|} \quad (\text{A.59})$$

$$H = \rho c_p |V_*| \theta_* \quad (\text{A.60})$$

$$E = \rho |V_*| r_* \quad (\text{A.61})$$

where V_* is the friction velocity, θ_* is the friction potential temperature and r_* is the friction mixing ratio, computed from:

$$|V(h)| = |V_*| \kappa^2 \left(\ln \frac{z_m}{z_0} \right)^{-2} \quad (\text{A.62})$$

$$\theta(z_m) - \theta(z_T) = \theta_* \kappa^2 \left(\ln \frac{z_m}{z_0} \right)^{-1} \left(\ln \frac{z_m}{z_T} \right)^{-1} \quad (\text{A.63})$$

$$r(z_m) - r(z_T) = r_* \kappa^2 \left(\ln \frac{z_m}{z_0}\right)^{-1} \left(\ln \frac{z_m}{z_T}\right)^{-1} \quad (\text{A.64})$$

where z_m is the lowest model level height (35 meters) and z_0 and z_T are the momentum and thermodynamic roughness lengths, respectively. Over land, $z_0 = z_T$. Over water, the two roughness lengths are functions of velocity. In high-resolution HWRF, these are calculated based in empirical formulae backed by observational data from CBLAST (Zhang et al., 2008a). The operational HWRF uses CBLAST data up to 30 m/s wind speed, beyond which non-physical values are used for reasons related to model tuning.

A.2.3.4 Turbulent Mixing: GFS Planetary Boundary Layer Scheme

The planetary boundary layer (PBL) scheme is responsible for sub-gridscale mixing throughout the vertical column of the atmosphere. The scheme used in the HWRF is a slightly older version of the GFS PBL scheme. This scheme originates in the GFDL model (Hong and Pan, 1996), and is based on the Troen and Mahrt (1986) scheme, implemented in GFS in 1995. The GFS PBL scheme used in the current GFS model has undergone revisions, and plans are in place to test those revisions in both high-resolution and low-resolution HWRF in the near future.

This first-order vertical diffusion scheme iteratively estimates a PBL height from the ground upward using a bulk-Richardson approach. The coefficients of diffusivity K_c are a cubic function of PBL height and are matched to the surface layer fluxes, discussed in Section A.2.3.3. The scheme includes a counter-gradient flux parameterization (Hong and Pan, 1996). Mixing is divided into local and non-local

where local mixing is diagnosed based on the PBL height and non-local includes effects of large-scale eddies driven by surface layer fluxes. The tendency of a parameter C is then $\frac{\partial C}{\partial t} = \frac{\partial}{\partial z}(K_c(\frac{\partial C}{\partial z} - \gamma_c))$ where $\frac{\partial C}{\partial z}$ is the local mixing and γ_c is non-local.

A.2.3.5 Radiation Schemes

In HWRF, radiation is divided up into longwave and shortwave and is calculated one dimensionally (regardless of solar zenith angle, neighboring grid columns are never considered). Longwave radiation is handled by the simplified exchange method of Fels and Schwarzkopf (1975); Schwarzkopf and Fels (1991) which performs calculations over broad spectral bands, including the effects of carbon dioxide, water vapor and ozone. Transmission coefficients for carbon dioxide come from Schwarzkopf and Fels (1985), water vapor from Roberts et al. (1976) and ozone from Rodgers (1968). Carbon dioxide and ozone concentrations come from climatology, and cloud overlap effects are determined randomly. Shortwave radiation is handled by the GFDL version of the Lacis and Hansen (1974) scheme with carbon dioxide effects from Sasamori et al. (1972),

A.2.3.6 Land Surface Model: GFDL Slab Model

The land surface in HWRF is handled via the one-level GFDL slab model, which predicts only the surface temperature T_* via:

$$\frac{\partial T_*}{\partial t} = \frac{-\sigma T_*^4 - S_{HFX} - L_{EVP} + (S + F)}{\rho_s c_s d} \quad (\text{A.65})$$

where S_{HFX} is the sensible heat flux and L_{EVP} is the evaporative flux, both from the surface layer scheme in Section A.2.3.3. $S+F$ is the net downward radiative flux calculated from the radiation schemes in Section A.2.3.5. Soil density ρ_s , specific heat c_s and damping depth d are based on constant surface wetness from the GFS analysis.

A.3 Initialization: GSI, Vortex Relocation and Bogussing

The HWRF initialization is very complex and a full explanation could fill a novel. Only a brief summary of the critical components will be given here. The main purpose of this initialization suite is to move the tropical cyclone vortex to the location specified by forecasters, and give it the correct initial intensity. 3DVAR data assimilation is also applied using the GSI system, but is not as critical since the initial fields, from the parent GFS model, have already had data assimilated via the same 3DVAR program.

The initialization begins with the prep hybrid program, which takes the native output files from GFS, containing spectrally-decomposed values for virtual temperature, specific humidity and other fields on hybrid levels. The prep hybrid transforms these to a global 0.5° grid and then interpolates to the WRF-NMM atmospheric grid to produce initial “first guess” input conditions and also boundary conditions.

After that, the atmosphere-only forecast model is run twice for one minute each to interpolate near analysis time fields to the 9 km domain. The first simulation creates a 9 km domain initialization file known as the *analysis domain* to be used

for initialization of the actual forecast at the end of this initialization system. The second simulation creates a much larger 9 km domain known as the *ghost domain*, around 36x36° in size, for use by the vortex relocation system.

The “first guess” input conditions are then fed to the vortex relocation suite. This suite first subtracts the vortex from the prep hybrid output and ghost domain. For a “cold start” (the first simulation of the storm) a simple axially symmetric vortex is inserted back into the prep hybrid output and ghost domain with the location, size and intensity specified by the forecasters. For a “warm start” (a simulation for a storm that follows a successful simulation 6 hours prior), the previous cycle’s vortex is taken. It is then resized and has its intensity is modified. The final vortex is inserted back into the prep hybrid output and the ghost domain.

Next, the GSI data assimilation is run separately for the prep hybrid domain and ghost domain. The final ghost domain is then merged back into the smaller 9 km analysis domain file. Then, the model forecast can be run.

Appendix B

Observation of Tropical Cyclones

This appendix explains some of the observational systems used by this thesis. The NOAA P3 has already been presented in chapter 2, so this appendix explains radar and infrared remote sensing.

B.1 TRMM VIRS Imager

The only infrared remote sensing done in this thesis is a simple analysis of 10.8 μm brightness temperatures. Due to the simplicity, this will be presented first.

The brightness temperature is a tool of convenience. The brightness temperature T_b is the temperature that is required to match the measured intensity (at characteristic wavenumber $\bar{\nu}$) to the Planck blackbody function. It is equal to:

$$T_b = \frac{hc\bar{\nu}}{k_B} \left(\ln \left(\frac{2hc^2\bar{\nu}^3}{I_m} + 1 \right) \right)^{-1} \quad (\text{B.1})$$

where I_m is the measured intensity and others are universal constants.

The VIRS channel used is the 10.8 μm channel which is chosen because of several large advantages of that spectral band. Solar radiation in that wavelength is small, so it is a reasonable approximation to say that the source of radiation is the atmosphere. Clouds are optically thick at 10.8 μm so the lowest radiator in a cloudy column is the highest cloud. Above high hurricane convection, there is very little absorption from water vapor or other trace gasses so the brightness temperature

can be viewed, nominally, as the temperature of the highest optically thick cloud. These are only approximations, and are not perfect, but seem to hold quite well. Hence the $10.8 \mu m$ band is used extensively for analyzing cloud tops, not just for this thesis, but throughout the tropical cyclone forecasting community.

B.2 Radar Reflectivity Factor and dbZ

Active radar is an invaluable tool for examining the structure of convection, and has been used throughout this thesis. This section contains a brief explanation of how radar remote sensing works, and provides a description of the three radars that were used.

The weather radars used in this thesis work by sending out a radar pulse of power P_t at wavelength λ with gain G in some direction, and then measuring the returned power P_r after gain G at the same radar whose radius is R . These assumptions made are:

1. All absorption, reflection and scattering is done by spherical solid or liquid particles.
2. The spherical particles have a constant index of refraction throughout their volume (though the index of refraction is allowed to be complex).
3. The particle size is much smaller than the wavelength of the radar. Specifically:

$$\alpha_R \equiv 2\pi r/\lambda \tag{B.2}$$

where r is the particle radius, λ is the radar wavelength, and α_R is the *size parameter*. Specifically,

$$\alpha_R \ll 1 \Rightarrow 2\pi r \ll \lambda \quad (\text{B.3})$$

Under those assumptions, one can derive that:

$$\frac{P_r}{P_t} = \frac{G^2 \lambda^2}{(4\pi)^3 R^4} dV \int_0^\infty n(r) C_b(r) dr \quad (\text{B.4})$$

where r is particle radius, $n(r)$ is the number of particles of a given size per cubic meter, and $C_b(r)$ is the backscattering cross-section for a particle of radius r .

The standard product reported by radars is the *radar reflectivity factor* Z , which is defined as:

$$Z \equiv \int_0^\infty n_l(D_l) D_l^6 dD_l \quad (\text{B.5})$$

Here, D_l is the diameter of liquid particles in a given volume, or the equivalent melted diameter of ice particles. The $n_l(D_l)$ is the number of particles of the given size per cubic meter. (Note that Z and all other variables are in *SI units* rather than their usual units.) Under the assumption of Rayleigh scattering by liquid spheres with a constant (possibly complex) index of refraction throughout their entire volume,

$$Z = \frac{\lambda^2}{|K_l|^2 \pi^5} \int_0^\infty n(r) C_b(r) dr \quad (\text{B.6})$$

where:

$$K_l = \frac{m_l^2 - 1}{m_l^2 + 2} \quad (\text{B.7})$$

and m_l is the complex index of refraction of water, and is assumed to be a constant (not a function of λ , T or any other variables). If we further assume that all scattering particles are liquid, then:

$$\frac{P_{r,l}}{P_t} = \frac{G^2 \pi^2 |K|^2}{64 R^4} dV Z \quad (\text{B.8})$$

Note the lack of any λ in that equation. That is the value of Z : it removes any wavelength dependence (if m is constant with wavelength). To simplify matters, one defines the *radar constant* as:

$$C \equiv \frac{P_t G^2 \pi^2 dV}{64} \quad (\text{B.9})$$

reducing the prior equation to:

$$P_{r,l} = \frac{|K|^2}{R^2} C Z \quad (\text{B.10})$$

Hence, under idealized conditions (that hold pretty well in liquid precipitation with land-based 10cm radars), the radar reflectivity P_r/P_t is proportional to Z . For that reason, the radar reflectivity factor Z is usually treated as the measured value. Due to the wide range of orders of magnitude encountered, it is convenient to use decibels of Z , or dbZ , defined as:

$$dbZ \equiv 10 \log_{10} Z \quad (\text{B.11})$$

The last matter to attend to is dV used in the above equations. The dV refers to the volume over which the radar return is integrated. Recall that the radar sends out a pulse in a given direction, and that pulse is reflected by various hydrometeors along its path. The pulse travels at finite speeds, meaning that radar returns from more distant hydrometeors will be received later than the closer ones. This allows the radar return to be separated into equally-spaced distance bins referred to as *gates*. Data from all gates along the path of a single pulse is referred to as a *dwelt*. The standard notation used is as follows:

$$dV = \Delta\theta\Delta\phi h/2 \tag{B.12}$$

where $\Delta\theta$ is the angular width at half maximum of the outgoing radar pulse in the horizontal direction, and $\Delta\phi$ is the width at half maximum in the vertical direction. (Recall that the original radars were land-based, side-scanning radars.) Then, $h/2$ is the pulse length at one half maximum for the transmitted signal.

B.3 Breakdown of Z Assumptions

Over most of the atmosphere, the various assumptions made in deriving the relation between Z and the returned power break down due to the presence of ice or other factors. Hence, a different quantity is used in place of Z : the *effective radar reflectivity factor* Z_e :

$$Z_e \equiv \frac{P_r}{P_t} \frac{\lambda^4}{|K_l|^2 \pi^5} \tag{B.13}$$

In the absence of gaseous absorption and multiple scattering, the effective radar reflectivity factor can be thought of as the radar reflectivity factor that would be experienced if a given volume of air was filled with liquid water spheres that produced the same amount of returned power.

In addition to those problems, multiple scattering and gaseous absorption in the microwave regions can cause the above assumptions to break down. For more precise data, those two problems are dealt with by determining the actual $P_t(V)$ for a given volume V , and then calculating Z_e based on that.

Note the power of six in the equation for Z . That makes Z extremely sensitive to particle size, meaning that a few hail particles among numerous small ice crystals will have a gigantic Z . Meanwhile, a nearby area of air with the same density of ice crystals flakes but no hail will have a much smaller Z . Hence Z is primarily a measure of the largest particle size present in a given volume, with particle number density just being a secondary effect.

One location where this is most strongly visible is the *melting layer*, also known as the *freezing layer*. In the melting layer, falling ice crystals break up, coalesce to form large particles with large Z values, then fall and melt, producing smaller particles with smaller Z values below the melting layer. The freezing layer works similarly. Rising water freezes into ice crystals, riming processes produce larger and larger graupel and hail with larger and larger Z values. In either case, there is a strong Z signature at the freezing or melting level, and that is known as the *radar bright line* or *bright line* for short.

The largest sphere present in most radar data is the Earth itself, which backscat-

ters nearly all of the incident radiation. The Earth surface typically has a dbZ value of 80 or higher in the data that is analyzed in this thesis. X-band satellites take advantage of that to map the Earth surface heights – you don't need a very sensitive receiver to see the reflection of radar off of the Earth surface.

B.4 Specific Radars Used

This thesis made use of three radars: the lower-fuselage radar on the P3 discussed earlier, the nadir-pointing EDOP radar onboard the NASA ER-2 aircraft, and the TRMM satellite radar. This section will discuss the specifics of each radar system.

The P3 lower-fuselage radar is a side-scanning radar mounted on the same two P3 aircraft that provide the in-situ measurements for this study. The lower-fuselage radar scans 360 degrees in approximately six seconds, and has a 150m gate spacing. It suffers from severe attenuation issues at longer ranges, and consequentially, it is only used for subjective work. Its primary uses are determining where the aircraft is in the storm, and what events are occurring nearby (ie.: a hot tower or formation of a rainband).

The ER-2 EDOP 9.6GHz Doppler radar is mounted on the bottom of the NASA ER-2, a modified U2 spy-plane designed to fly above storms and take meteorological measurements. The nadir-pointing Doppler radar is used, and points directly downward, without scanning at all. The ER-2 flies at around 20km when performing these measurements, providing a sheet of data. The beam width is 3.3

degrees, resulting in an approximately 1.2 km footprint at the ground. Bidwell et al. (1996); Heymsfield et al. (1996, 1999)

The TRMM satellite-based radar is a nadir-pointing radar at approximately 250km altitude, with a 224 km swath, 5km ground footprint and 250m vertical resolution. It does not have Doppler measurement capabilities, and this thesis uses it mainly for its ability to measure the upper portions of convective clouds. Weiler (2007)

Appendix C

Adventures in High-Resolution Modeling

Designing a reliable high-resolution HWRF that got usable forecasting skill required thousands of hours of work over the past few years, and many problems had to be overcome. Chapter 7 explains a major bug relating to the model forgetting condensate type fractions and how it was fixed. This appendix discusses some of the other problems. However, this appendix can safely be skipped by the reader without inhibiting understanding of the remainder of this thesis. This appendix is included out of a fear that the past few chapters, to some, may have indicated that configuring this model was a simple matter of turning some switches on and off and fixing a few lines of buggy code. Unfortunately, that was not so. An explanation of all issues encountered and how they were solved would fill a ten inch thick tome, but a few more notable problems will be discussed here.

C.1 HHS: A Test Suite

The largest problem encountered was not in HWRF itself, but the lack of a test suite. Getting good forecasting skill with a large sample set requires running a large number of simulations to ensure that model developments do not hurt forecasting skill. Every simulation in that large set has to be run correctly, with even the smallest failures detected (missing input file, failed ocean initialization, output

tracker file missing, etc.) Before 2009, this was done manually, a highly error-prone process, and very time-consuming as well. It took manual intervention by the entire HWRF team for several weeks to rerun a full hurricane season reanalysis for a single model configuration.

To fix that problem, an automation system called the HWRF History Sequence (HHS) system was created. HHS is designed to exactly reproduce the actions of a perfect human operator running HWRF, including the necessary checks for successful completion of various stages of the simulation. Upon detecting a failed simulation, HHS emails the actual human operator and stops submitting simulations for that storm until after needed human intervention. While this may sound like a simple system, there is an incredible level of complexity of monitoring every aspect of HWRF, in a cross-platform manner, and working around deficiencies of various supercomputers. (Or, to put it in a number, HHS is around 13,000 lines of code.) Initially, this system was designed just to run retrospective simulations of HWRF (hence “history” sequence), but now works in real-time mode and is being used to run the high-resolution HWRF for the 2011 seasons.

Another feature of the HHS, that is actually just as critical as its careful testing abilities, is its ability to delete files when they are no longer required. Each high-resolution HWRF simulation takes about 400 GB of disk space, and typically only about 9 TB are available during retrospective and real-time runs. Waiting for manual deletion after a weekend of simulations would not work, since the 9 TB space limit would be overrun by a factor of 5 or more. The HHS knows when a simulation has finished, and when its output is no longer needed for post-processing

or for initializing the next forecast cycle, so it can delete the data automatically once it is safe to do so.

This all allows an enormous throughput. On the Jet supercomputer, under the HWRFV3 account, over 400 simulations per day can be run with the low-resolution HWRF. The high-resolution HWRF, with its higher resource requirements has reached about 100 simulations per day on that account. With HHS, we have reached a point where simulation throughput is limited only by available resources. This places us at the ideal point where computational resource availability and the ability of humans to do model diagnostics and model development is the main bottleneck in advancing HWRF.

C.2 New Built-In Model Vortex Tracker

Next among the major issues was the HWRF vortex tracker code. Inside the HWRF model, is a few Fortran subroutines that look for a vortex in the model fields every few timesteps, to decide when and if to move the domain. The HRD had produced an improved vortex tracker code that tracks the centroid of several pressure minima, an improvement that is necessary for the 3 km resolution which often produces mesovortices with associated local pressure deepening. Unfortunately, with this new vortex tracker, the model often crashed. That was a problem never encountered by HRD.

Investigation turned up a few interesting discoveries about the model. The HRD had been initializing their model with an older version of the GFS (2005

version, primarily) as input and boundary conditions. That GFS did a poor job of representing hurricane vortices, while the new 2011 GFS, used by the new high-resolution HWRF, is able to represent the storm-scale structure due to its higher 30 km resolution, newer parameterizations and other improvements. What was happening was that the better GFS input and boundary conditions allowed the HWRF outer domain to have strong vortices in the initial state, despite the low 27 km resolution. HWRF happily continued simulating those vortices in its outer domain, and many achieved realistic intensity. HWRF-X used the older GFS, so no strong storms were present in its outer domain in the initial state.

Meanwhile, the vortex tracker was being run on both the 9 km and 3 km domain, and the two domains independently followed their idea of where the vortex was. Typically, both domains are able to keep the vortex in the center of the domain, both in HRD's older simulations and in the newer ones being run now. However, sometimes, the larger 9 km domain would move into an area where the 27 km domain was resolving a much more powerful storm. That 27 km domain storm would then be present, in part, in the corner of the 9 km domain, but not in the small 3 km resolution domain. The 3 km domain would follow the storm of interest, while the 9 km domain followed the centroid of the two storms. After a while, the edge of the 3 km domain would leave the 9 km domain, and the model would attempt to interpolate data from outside the 9 km domain — uninitialized memory — onto the 3 km domain. The resulting garbage values for P , T , u , v , etc. would quickly cause a crash (9.310³⁸ m/s winds don't combine well with -3899.7 K temperatures, do they?)

The fix for this was to modify the 9 km domain so that it would stay centered on the 3 km domain, instead of tracking the vortex separately. Also, an added safeguard was placed in the nest movement code, which prevented a parent domain from moving if it would cause any of its children to lie outside of a 5 gridpoint coral distance inside the domain edge (a limitation that is required due to some assumptions throughout the model). The 3 km domain still occasionally “jumps” to the wrong storm or follows the centroid of two storms, on the rare occasions when two storms are so close that both lie within the 3 km resolution, $6 \times 6^\circ$ inner domain. However, now that the much larger 9 km domain is no longer tracking vortices, this problem is comparatively rare, and does not result in a crash of the model.

C.3 Initialization: Vortex Relocation with Three Domains

The HWRF initialization, discussed in Section A.3, had to be modified for the 27:9:3 triple-domain, high-resolution configuration. Unfortunately, it has never been run with a three domain model, only with two domains. Xuejin Zhang at HRD was working on modifications to allow this, but the system was not ready by the HFIP Stream 1.5 deadlines, risking the model losing resources required for development and real-time applications. Hence, an alternative was developed.

A two domain initialization was run, initializing just the 27 km and 9 km domains with a vortex using the operational HWRF initialization system, which has no knowledge of the 3 km domain. The 3 km domain was initialized simply by bilinear interpolation, using standard routines built in to the WRF system. Unfortunately,

this leads to blurred, 3x3 gridpoint areas which spawn weak, but non-physical features in the early parts of the simulation. It also means that the smaller storms are not correctly represented in the vortex relocation process, since a 9 km resolution vortex is used for the relocation system.

In the first attempt at producing this two domain initialization, the three domain track file was used as input to the relocation system, giving it the 3 km resolution track and intensity when it was relocating the 9 km resolution vortex. This contributed to a positive intensity bias in the model. Hence, a new track file was added, that used only the 9 km and 27 km domain data to produce track and intensity information, correcting that issue.

C.4 Track and Intensity Information

A hurricane forecasting model that produces no forecast, has no use. Earlier in its development, this model produced no forecast. When attempting to run the NCEP Tracker on HWRF input at full model resolution, an unexpected problem was encountered. The GRIB1 file format does not support a 3 km resolution, 75x75° domain, because that goes beyond the maximum number of gridpoints that can be represented by the GRIB1 file format. There is a GRIB2 format, but neither GRIB2 manipulation programs (`copygb2` and `wgrib2`) have had their GRIB2 merge capabilities tested. That capability is critical since the 27 km, 9 km and 3 km domains must be merged to allow the tracker to search for a storm and its intensity. There are two solutions to this problem, one that has been implemented

as a temporary measure, and another that is under development.

The HRD has a high-resolution diagnostics system called Diapost that produces, among other things, 3 km resolution track and intensity information. It assumes that the HWRF nest is always perfectly centered on the storm, and reports the nest center location as the storm location, and the gridpoint maximum wind as the maximum one minute sustained ten meter wind. Meanwhile, the NCEP tracker was run at 0.1° resolution, producing a much more reliable track, but an intensity that was sometimes much lower than the gridpoint maximum. These track files were then merged. The track from the NCEP tracker was used and the intensity from Diapost's tracker was used. This was done up to the last forecast hour at which the 3 km resolution nest center (Diapost storm center location) is within 100 km of the NCEP tracker storm center location.

That approach has the limitation of only being able to predict the intensity of the storm when it is being simulated by the 3 km resolution domain. A better solution is under development. The NCEP tracker is being modified to read three GRIB files for each forecast hour: one from the 27 km domain, one from the 9 km domain and one from the 3 km domain. It will then do the interpolation internally, producing a grid that is roughly $20 \times 20^\circ$ in size, at the resolution of the finest grid (3 km resolution).

That improved tracker has one possibly larger impact if it is applied to a global model. The modified tracker could be run on the GFS model at full model resolution. Recalling Chapter 4, the difference between the intensity at the 0.5° resolution of the GFS output GRIB2 files, and the intensity at the native 30 km resolution can

be fairly large. That is especially true if one considers the f_v^2 case of a vortex that is not axially symmetric. This may result in a significant improvement of the GFS intensity forecast.

Bibliography

- Aberson, S. D., M. T. Montgomery, M. Bell, and M. Black, 2006: Hurricane Isabel (2003): New insights into the physics of intense storms. Part II: Extreme localized wind. *Bulletin of the American Meteorological Society*, **87** (10), 1349–1365.
- Anselin, L., 2001: Spatial effects in econometric practice in environmental and resource economics. *American Journal of Agricultural Economics*, **83** (3), 705–710.
- Arakawa, A. and W. H. Schubert, 1974: Interaction of a cumulus cloud ensemble with the large-scale environment, Part I. *Journal of the Atmospheric Sciences*, **31**, 674–701.
- Bender, M. A. and I. Ginis, 2000: Real-case simulations of hurricane ocean interaction using a high-resolution coupled model: Effects on hurricane intensity. *Monthly Weather Review*, **128**, 917–946.
- Bevin, J., 2006: Dennis 2005. *Tropical Storm Report*, National Hurricane Center.
- Bidwell, S. W., G. M. Heymsfield, and I. J. Caylor, 1996: Capabilities and recent results from the ER-2 Doppler radar (EDOP). *Geoscience and Remote Sensing Symposium 1996: Remote Sensing for a Sustainable Future*.
- Black, M. L. and H. E. Willoughby, 1992: A concentric eyewall cycle of hurricane gilbert. *Monthly Weather Review*, **120**, 947–957.
- Braun, S. A., 2006: High-resolution simulation of Hurricane Bonnie (1998). Part II: Water budget. *Journal of Atmospheric Sciences*, **63**, 43–64.
- Braun, S. A., M. T. Montgomery, and Z. Pu, 2006: High-resolution simulation of Hurricane Bonnie (1998). Part I: The organization of eyewall vertical motion. *Journal of Atmospheric Sciences*, **63**, 19–42.
- Bryan, G. H., J. C. Wyngaard, and J. M. Fritsch, 2003: Resolution requirements for the simulation of deep moist convection. *Monthly Weather Review*, **131**, 2394–2416.
- Cayón, L., 2010: Variograms of the cosmic microwave background temperature fluctuations: confirmation of deviations from statistical isotropy. *Monthly Notices of the Royal Astronomical Society*, **405**, 1084–1088.
- Center, N. H., 1974: Hurricane Fifi. *Preliminary Report*.
- Chang, H.-Y., 2010: Personal communication.
- Charney, J. G. and A. Ellassen, 1964: On the growth of the hurricane depression. *Journal of the Atmospheric Sciences*, **21**, 68–75.

- Chen, Y. and M. K. Yau, 2001: Spiral bands in a simulated hurricane. Part I: Vortex Rossby wave verification. *Journal of the Atmospheric Sciences*, **58**, 2128–2145.
- Chu, J.-H., C. R. Sampson, A. S. Levine, and E. Fukada, 2002: The joint typhoon warning center tropical cyclone best-tracks, 1945-2000. Tech. Rep. NRL/MR/7540-02-16, Naval Research Laboratory.
- Corbosiero, K. L., 2008: Inner core structures and intensity change simulated with the advanced hurricane WRF model. *28th Conference on Hurricanes and Tropical Meteorology*, American Meteorological Society.
- Cram, T. A., J. Persing, M. T. Montgomery, and S. A. Braun, 2007: A lagrangian trajectory view on transport and mixing processes between the eye, eyewall and environment using a high resolution simulation of Hurricane Bonnie (1998). *Journal of Atmospheric Sciences*, **64**, 1835–1856.
- Davis, A., A. Marshak, W. Wiscombe, and R. Calahan, 1994: Multifractal characterizations of nonstationarity and intermittancy in geophysical fields: Observed, retrieved or simulated. *Journal of Geophysical Research*, **99 (D4)**, 8055–8072.
- Davis, C. and L. F. Bosart, 2002: Numerical simulations of the genesis of Hurricane Diana (1984). Part II: Sensitivity of track and intensity prediction. *Monthly Weather Review*, **130**, 1100–1124.
- Davis, C., W. Wang, J. Dudhia, and R. Torn, 2010: Does increased horizontal resolution improve hurricane wind forecasts? *Weather and Forecasting*, **25**, 1826–1841.
- Davis, C., et al., 2008: Prediction of landfalling hurricanes with the advanced hurricane WRF model. *Monthly Weather Review*, **136**, 1990–2005.
- DeMaria, M. and J. Kaplan, 1994: Sea surface temperature and the maximum intensity of atlantic tropical cyclones. *Journal of Climate*, **7**, 1324–1334.
- Developmental Testbed Center, 2010: February 2010 HWRF scientific documentation. Tech. rep., National Oceanic and Atmospheric Administration.
- Dimri, V. P., (Ed.) , 2005: *Fractal Behaviour of the Earth System*. Springer-Verling Berlin, Heidelberg, The Netherlands.
- Dvorak, V. F., 1984: Tropical cyclone intensity analysis using satellite data. Tech. rep., National Environmental Satellite, Data, and Information Service.
- Eastin, M. D., W. H. Gray, and P. G. Black, 2005: Buoyancy of convective vertical motions in the inner core of intense hurricanes. part I: General statistics. *Monthly Weather Review*, **133**, 188–208.
- Eliassen, A., 1951: Slow thermally or frictionally controlled meridional circulation in a circular vortex. *Astrophisica Norvegica*, **5 (2)**, 19.

- Emanuel, K., 1999: Thermodynamic control of hurricane intensity. *Nature*, **401**, 665–669.
- Emanuel, K., 2007: Environmental factors affecting tropical cyclone power dissipation. *Journal of Climate*, **20**.
- Emanuel, K. A., 1988: The maximum intensity of hurricanes. *Journal of Atmospheric Science*, **45**, 1143–1155.
- Emanuel, K. A., 1991: The theory of hurricanes. *Annual Review of Fluid Mechanics*, **23**, 179–196.
- Emanuel, K. A., 1997: Some aspects of hurricane inner-core dynamics and energetics. *Journal of the Atmospheric Sciences*, **54**, 1014–1026.
- Falkovich, G. and K. R. Sreenivasen, 2006: Lessons from hydrodynamic turbulence. *Physics Today*, 43–49.
- Fels, S. B. and M. D. Schwarzkopf, 1975: The simplified exchange approximation: A new method for radiative transfer calculations. *Journal of the Atmospheric Sciences*, **32**, 1475–1488.
- Ferrier, B., 2010: Personal communication.
- Foster, R. C., 2005: Why rolls are prevalent in the hurricane boundary layer. *Journal of the Atmospheric Sciences*, **62**, 2647–2661.
- Foster, R. C., 2008: Boundary-layer similarity under an axisymmetric, gradient wind vortex. *Boundary Layer Meteorology*, **131**, 321–344.
- Frank, W. M. and E. A. Ritchie, 1998: Effects of environmental flow upon tropical cyclone structure. *Monthly Weather Review*, **127**, 2044–2061.
- Franklin, C. N., G. J. Holland, and P. T. May, 2005: Sensitivity of tropical cyclone rainbands to ice-phase microphysics. *Monthly Weather Review*, **133**, 2473–2493.
- Franklin, J. L., 2009: 2008 National Hurricane Center forecast verification report. Tech. rep., Tropical Prediction Center.
- French, J. R., W. M. Drennan, J. A. Zhang, and P. G. Black, 2007: Turbulent fluxes in the hurricane boundary layer. Part I: Momentum flux. *Journal of the Atmospheric Sciences*, **64**, 1089–1102.
- French, J. R., W. M. Drennan, J. A. Zhang, and P. G. Black, 2009: Turbulent fluxes in the hurricane boundary layer. part I: Momentum flux. *Journal of the Atmospheric Sciences*, **64**, 1089–1102.
- Frisch, U., 1995: *Turbulence: the legacy of AN Kolmogorov*. Cambridge University Press, Cambridge, UK.

- Gentry, M. S., 2007: Sensitivity of WRF simulations of Hurricane Ivan to horizontal resolution. M.S. thesis, Marine, Earth and Atmospheric Sciences, North Carolina State University.
- Gilmore, M. S., J. M. Straka, and E. N. Rasmussen, 2004: Precipitation uncertainty due to variations in precipitation particle parameters within a simple microphysics scheme. *Monthly Weather Review*, **132**, 2610–2627.
- Grell, G. A., 1993: Prognostic evaluation of assumptions used by cumulus parameterizations. *Monthly Weather Review*, **121**, 764–787.
- Guimond, S. R., G. M. Heymsfield, and F. J. Turk, 2010: Multiscale observations of Hurricane Dennis (2005): The effects of hot towers on rapid intensification. *Journal of the Atmospheric Sciences*, **67**, 633–654.
- Guiney, J. L. and M. B. Lawrence, 1999: Hurricane Mitch 22 october – 05 november 1998. *Preliminary Report*, National Hurricane Center.
- Halverson, J., 2011: Personal communication.
- Han, J. and H.-L. Pan, 2006: Sensitivity of hurricane intensity forecasts to convective momentum transport parameterization. *Monthly Weather Review*, **134**, 664–674.
- Hattori, Y., R. Rubenstein, and A. Ishizawa, 2004: Shell model for rotating turbulence. *Physics Review E*, **70**.
- Heymsfield, G. M., J. B. Halverson, and I. J. Caylor, 1999: A wintertime gulf coast squall line observed by EDOP airborne Doppler radar. *Monthly Weather Review*, **127**, 2928–2950.
- Heymsfield, G. M., J. B. Halverson, J. Simpson, L. Tiand, and T. P. Buie, 2001: Er-2 doppler radar investigations of the eyewall of hurricane bonnie during the convection and moisture experiment. *Journal of Applied Meteorology*, **40**, 1310–1330.
- Heymsfield, G. M., et al., 1996: The edop radar system on the high-altitude nasa er-2 aircraft. *Journal of Atmospheric and Oceanic Technology*, **13**, 795–809.
- Hong, S.-Y. and H.-L. Pan, 1996: Nonlocal boundary layer vertical diffusion in a medium-range forecast model. *Monthly Weather Review*, **124**, 2322–2339.
- Irish, J. L., D. T. Resio, and J. J. Ratcliff, 2008: The influence of storm size on hurricane surge. *Journal of Physical Oceanography*, **38**, 2003–2013.
- Jiang, J. H., B. Wang, K. Goya, K. Hocke, S. D. Eckermann, J. Ma, D. L. Wu, and W. G. Read, 2004: Geographical distribution and interseasonal variability of tropical deep convection: UARS MLS observations and analyses. *Journal of Geophysical Research*, **109**.

- Jorgensen, D. P., E. J. Zipser, and M. A. LeMone, 1985: Vertical motions in intense hurricanes. *Journal of the Atmospheric Sciences*, **42**, 839–856.
- Jr., R. A. H., et al., 2006: The hurricane rainband and intensity change experiment. *Bulletin of the American Meteorological Society*, 1503–1521.
- Kaplan, J. and M. DeMaria, 2003: Large-scale characteristics of rapidly intensifying tropical cyclones in the north atlantic basin. *Weather and Forecasting*, **18**, 1093–1108.
- Kasahara, A. and G. W. Platzman, 1963: Interaction of a hurricane with the steering flow and its effect upon the hurricane trajectory. *Tellus*, **15** (4), 321–335.
- Kato, T. and K. Saito, 1995: Hydrostatic and non-hydrostatic simulations of moist convection: Applicability of the hydrostatic approximation to a high-resolution model. *Journal of the Meteorological Society of Japan*, **73**, 59–77.
- Kelley, O. A., J. Stout, and J. B. Halverson, 2005: Hurricane intensification detected by continuously monitoring tall precipitation in the eyewall. *Geophysical Research Letters*, **32**.
- Kerr, R. M., 2002: Is there a 2D cascade in 3D motion? *contemporary mathematics: advances in wave interaction and turbulence*, Vol. 283, 41–49.
- Khelif, D., S. P. Burns, and C. A. Friehe, 1999: Improved wind measurements on research aircraft. *Journal of Atmospheric and Oceanic Technology*, **16**, 860–875.
- Kolmogorov, A. N., 1941: The local structure of turbulence in incompressible viscous fluid for very large Reynolds numbers. *Proceedings of the USSR Academy of Sciences*, **30**, 299–303.
- Kolmogorov, A. N., 1962: A refinement of previous hypotheses concerning the local structure of turbulence in a viscous incompressible fluid at high reynolds number. *Journal of Fluid Mechanics*, **13**.
- Kolmogorov, A. N., 1991: The local structure of turbulence in incompressible viscous fluid for very large Reynolds numbers. *Proceedings of the Royal Society of London, Series A: Mathematical and Physical Sciences*, **434**, 9–13.
- Kossin, J. P. and M. D. Eastin, 2001: Two distinct regimes in the kinematic and thermodynamic structure of the hurricane eye and eyewall. *Journal of the Atmospheric Sciences*, **58**, 1079–1090.
- Kossin, J. P. and W. H. Schubert, 2001: Mesovortices, polygonal flow patterns, and rapid pressure falls in hurricane-like vortices. *Journal of the Atmospheric Sciences*, **58**.
- Kossin, J. P. and W. H. Schubert, 2004: Mesovortices in Hurricane Isabel. *Bulletin of the American Meteorological Society*, 151–153.

- Koteswaram, P., 1967: On the structure of hurricanes in the upper troposphere and lower stratosphere. *Monthly Weather Review*, **95**, 541–564.
- Kraichnan, R. H., 1968: Small-scale structure of a scalar field convected by turbulence. *Physics of Fluids*, **11**, 945.
- Kuo, H.-C., R. T. Williams, and J.-H. Chen, 1999: A possible mechanism for the eye rotation of Typhoon Herb. *Journal of the Atmospheric Sciences*, **56**, 1659–1673.
- Kuo, H. L., 1959: Dynamics of convective vortices and eye formation. *The Atmosphere and Sea in Motion*, B. Bolin, Ed., Rockefeller Institute Press, 413–424.
- Kwon, Y. C. and W. M. Frank, 2005: Dynamic instabilities of simulated hurricane-like vortices and their impacts on the core structure of hurricanes. Part I: Dry experiments. *Journal of the Atmospheric Sciences*, **63**, 3955–3973.
- Kwon, Y. C. and W. M. Frank, 2008: Dynamic instabilities of simulated hurricane-like vortices and their impacts on the core structure of hurricanes. Part I: Moist experiments. *Journal of the Atmospheric Sciences*, **65**, 106–122.
- Lacis, A. A. and J. E. Hansen, 1974: A parameterization for the absorption of solar radiation in the earth’s atmosphere. *Journal of the Atmospheric Sciences*, **31**, 118–133.
- Landsea, C. W., G. D. Bell, W. M. Gray, and S. B. Goldenberg, 1998: The extremely active 1995 Atlantic hurricane season: Environmental conditions and verification of seasonal forecasts. *Monthly Weather Review*, **126**.
- Leslie, L. M. and G. S. Dietachmayer, 1992: Real-time limited area numerical weather prediction in Australia: a historical perspective. *Australian Meteorological Magazine*, **41**, 61–77.
- Lewis, B. M. and H. F. Hawkins, 1982: Polygonal eye walls and rainbands in hurricanes. *Bulletin of the American Meteorological Society*, **63**, 1294–1300.
- Liu, Y., D.-L. Zhang, and M. K. Yau, 1997: A multiscale numerical study of Hurricane Andrew (1992). Part I: Explicit simulation and verification. *Monthly Weather Review*, **125**, 3073–3093.
- Lord, S. J., 1982: Interaction of a cumulus cloud ensemble with the large-scale environment. Part III: Semi-prognostic test of the Arakawa-Schubert cumulus parameterization. *Journal of Atmospheric Sciences*, **39**, 88–103.
- Lynch, P., 2008: The origins of computer weather prediction and climate modeling. *Journal of Computational Physics*, **227**, 3431–3444.
- Mahalov, A. and Y. Zhou, 1996: Analytical and phenomenological studies of rotating turbulence. *Physics of Fluids*, **8**, 2138–2152.

- Mainelli, M., M. DeMaria, L. K. Shay, and G. Goni, 2008: Application of oceanic heat content estimation to operational forecasting of recent Atlantic category 5 hurricanes. *Weather and Forecasting*, **23**, 3–16.
- Malkus, J. S., 1958: On the structure and maintenance of the mature hurricane eye. *Journal of the Atmospheric Sciences*, **15**, 337–349.
- Malkus, J. S. and H. Riehl, 1960: On the dynamics and energy transformations in steady-state hurricanes. *Tellus*, **12**, 1–20.
- Marshak, A., A. Davis, W. Wiscombe, and R. Cahalan, 1997: Scale invariance in liquid water distributions in marine stratocumulus. part II: Multifractal properties and intermittency issues. *Journal of the Atmospheric Sciences*, **54**.
- Masters, J. M. and J. A. Leise, 1993: Correction of inertial navigation with Loran C on NOAA’s P-3 aircraft. *Journal of Atmospheric and Oceanic Technology*, **10** (2), 145–154.
- Merrill, R. T., 1988: Environmental influences on hurricane intensification. *Journal of the Atmospheric Sciences*, **45** (11).
- Möller, J. D. and M. T. Montgomery, 1999: Vortex Rossby waves and hurricane intensification in a barotropic model. *Journal of the Atmospheric Sciences*, **56**, 1674–1687.
- Montgomery, M. T., M. M. Bell, S. D. Aberson, and M. L. Black, 2006: Hurricane Isabel (2003): New insights into the physics of intense storms. Part I: Mean vortex structure and maximum intensity estimation. *Bulletin of the American Meteorological Society*, 1335–1347.
- Montgomery, M. T. and R. J. Kallenbach, 1997: A theory for vortex Rossby-waves and its application to spiral bands and intensity changes in hurricanes. *Quarterly Journal of the Royal Meteorological Society*, **123**, 435–465.
- Montgomery, M. T., N. V. Sang, R. K. Smith, and J. Persing, 2009: Do tropical cyclones intensify by WISHE? *Quarterly Journal of the Royal Meteorological Society*, **135**, 1697–1714.
- Moorthi, S. and M. J. Suarez, 1992: Relaxed Arakawa-Schubert: A parameterization of moist convection for general circulation models. *Monthly Weather Review*, **120**, 978–1002.
- Morrison, I., S. Businger, F. Marks, P. Dodge, and J. A. Businger, 2005: An observational case for the prevalence of roll vortices in the hurricane boundary layer. *Journal of the Atmospheric Sciences*, 2662–2673.
- Muramatsu, T., 1986: The structure of polygonal eye of a typhoon. *Journal of the Meteorological Society of Japan*, **64**, 913–921.

- Narita, M. and S. Ohmori, 2007: Improving precipitation forecasts by the operational nonhydrostatic mesoscale model with the Kain-Fritsch convective parameterization and cloud microphysics. *The 12th Conference on Mesoscale Processes*, American Meteorological Society.
- Nyugen, S. V., R. K. Smith, and M. T. Montgomery, 2008: Tropical-cyclone intensification and predictability in three dimensions. *Quarterly Journal of the Royal Meteorological Society*, **134**, 563–582.
- Ooyama, K., 1964: A dynamical model for the study of tropical cyclone development. *Geofisica Internacional*, **4**, 187–198.
- Pan, H.-L., 2003: The GFS atmospheric model. Tech. Rep. 442, National Centers for Environmental Prediction.
- Pasch, R. J., E. S. Blake, H. D. C. III, and D. P. Roberts, 2006: Wilma 2005. *Tropical Storm Report*, National Hurricane Center.
- Paterson, L. A., B. N. Hanstrum, N. E. Davidson, and H. C. Weber, 2005: Influence of environmental vertical wind shear on the intensity of hurricane-strength tropical cyclones in the australian region. *Monthly Weather Review*, **133**, 3644–3660.
- Persing, J. and M. T. Montgomery, 2005: Is environmental CAPE important in the determination of maximum possible hurricane intensity? *Journal of the Atmospheric Sciences*, **62**, 542–550.
- Price, J., T. Sanford, and G. Forristall, 1996: Forced stage response to a moving hurricane. *Journal of Physical Oceanography*, **24**, 233–260.
- Prince, J., 1981: Upper ocean response to a hurricane. *Journal of Physical Oceanography*, **11**, 153–175.
- Reasor, P. D., M. T. Montgomery, F. D. M. Jr., and J. F. Gamache, 2000: Low-wavenumber structure and evolution of the hurricane inner core observed by airborne dual-Doppler radar. *Monthly Weather Review*, **128**, 1653–1680.
- Roberts, R. E., J. E. A. Selby, and L. M. Biberman, 1976: Infrared continuum absorption by atmospheric water-vapor in 8–12 um range. *Applied Optics*, **15**, 2085–2090.
- Rodgers, C. D., 1968: Some extensions and applications of the new random model for molecular band transmission. *Quarterly Journal of the Royal Meteorological Society*, **94**, 99–102.
- Rogers, E., T. Black, B. Ferrier, Y. Lin, D. Parrish, and G. DiMego, 2001: Changes to the NCEP meso eta analysis and forecast system: Increase in resolution, new cloud microphysics, modified precipitation assimilation, modified 3DVAR analysis. Tech. rep., Environmental Modeling Center.

- Samsury, C. E. and E. J. Zipser, 1995: Secondary wind maxima in hurricanes: Airflow and relationship to rainbands. *Monthly Weather Review*, **123**, 3502–3517.
- Sasamori, T., J. London, and D. V. Hoyt, 1972: Radiation budget of the southern hemisphere. *Meteorological Monographs*, **35**, 9–23.
- Schroeder, J. L., 1999: Hurricane bonnie wind flow characteristics. Ph.D. thesis, Texas Tech University.
- Schubert, W. H., C. M. Rozoff, J. L. Vigh, B. D. McNoldy, and J. P. Kossin, 2007: On the distribution of subsidence in the hurricane eye. *Quarterly Journal of the Royal Meteorological Society*, **133**, 595–605.
- Schwarzkopf, M. D. and S. Fels, 1985: Improvements to the algorithm for computing co2 transmissivities and cooling rates. *Journal of Geophysical Research*, **90 (C10)**, 10 541–10 550.
- Schwarzkopf, M. D. and S. Fels, 1991: The simplified exchange method revisited: An accurate, rapid method for computation of infrared cooling rates and fluxes. *Journal of Geophysical Research*, **96 (D5)**, 9075–9096.
- Shapiro, L. J. and H. E. Willoughby, 1982: The response of balanced hurricanes to local sources of heat and momentum. *Journal of the Atmospheric Sciences*, **39**, 378–394.
- Simpson, R., R. Anthes, M. Garstang, and J. Simpson, (Eds.) , 2002: *Hurricane!: Coping with Disaster: Progress and Challenges since Galveston, 1900*. American Geophysical Union.
- Smith, R. A. and M. N. Rosenbluth, 1990: Algebraic instability of hollow electron columns and cylindrical vortices. *Physics Review Letters*, **64**, 649–652.
- Smith, R. K., 1997: On the theory of CISK. *Quarterly Journal of the Royal Meteorological Society*, **123**, 407–418.
- Sparling, L. C. and J. T. Bacmeister, 2001: Scale dependence of tracer microstructure: PDFs, intermittency and the dissipation scale. *Geophysical Research Letters*, **28 (14)**, 2823–2826.
- Stanley, H. E., L. A. N. Amaral, P. Gopikrishnan, P. C. Ivanov, T. H. Keitt, and V. Plerou, 2000: Scale invariance and universality: organizing principles in complex systems. *Physica A*, **281**, 60–68.
- Trahan, S. and L. Sparling, 2011: An analysis of NCEP tropical cyclone vitals and potential effects on forecasting models, in review, *Weather and Forecasting*.
- Trahan, S., L. Sparling, and J. Halverson, 2008: Scale analysis of spatial variability in observations of tropical cyclones. *28th Conference on Hurricanes and Tropical Meteorology*.

- Trahan, S., V. Tallapragada, X. Zhang, and S. Gopalakrishnan, 2010: Progress towards a high-resolution HWRF. *64th Departmental Hurricane Conference*, National Oceanic and Atmospheric Administration.
- Troen, I. and L. Mahrt, 1986: A simple model of the atmospheric boundary layer: Sensitivity to surface evaporation. *Boundary Layer Meteorology*, **37**, 129–148.
- Vallado, D. A., P. Crawford, R. Hujsak, and T. S. Kelso, 2006: Revisiting spacetrack report 3. *Astrodynamics Specialist Conference*, AIAA/AAS.
- Velden, C., et al., 2006: The dvorak tropical cyclone intensity estimation technique: A satellite-based method that has endured for over 30 years. *Bulletin of the American Meteorological Society*, 1195–1210.
- Wang, Y., 2002a: An explicit simulation of tropical cyclones with a triply nested movable mesh primitive equation model: TCM3. Part II: Model refinements and sensitivity to cloud microphysics parameterization. *Monthly Weather Review*, **130**, 3022–3036.
- Wang, Y., 2002b: Vortex rossby waves in a numerically simulated tropical cyclone. Part I: Overall structure, potential vorticity, and kinetic energy budgets. *Journal of the Atmospheric Sciences*, **59**, 1213–1237.
- Wang, Y. and G. J. Holland, 1996: Tropical cyclone motion and evolution in vertical shear. *Journal of the Atmospheric Sciences*, **53** (22), 3313–3332.
- Wang, Y. and C. C. Wu, 2004: Current understanding of tropical cyclone structure and intensity changes — a review. *Meteorology and Atmospheric Physics*, **87**, 257–278.
- Weckerly, F., K. McFarland, M. Ricca, and K. Meyer, 2004: Roosevelt Elk density and social segregation: Foraging behavior and females avoiding larger groups of males. *American Midland Naturalist*, **152** (2), 386–389.
- Weckwerth, T. M., T. W. Horst, and J. W. Wilson, 1997a: An observational study of the evolution of horizontal convective rolls. *Monthly Weather Review*, **127**, 2160–2179.
- Weckwerth, T. M., J. W. Wilson, R. M. Wakimoto, and N. A. Crook, 1997b: Horizontal convective rolls: Determining the environmental conditions supporting their existence and characteristics. *Monthly Weather Review*, **125**, 505–526.
- Weightman, R. H., 1919: The West India Hurricane of September, 1919, in light of sounding observations. *Monthly Weather Review*, **47**, 717–720.
- Weiler, E. J., 2007: Tropical rainfall measuring mission senior review proposal 2007. Tech. rep., NASA Goddard Space Flight Center.

- Weisman, M. L., W. C. Skamarock, and J. B. Klep, 1997: The resolution dependence of explicitly modeled convective systems. *Monthly Weather Review*, **125**, 527–548.
- Willoughby, H. E., 1988: The dynamics of the tropical hurricane core. *Australian Meteorological Magazine*, **36**, 183–191.
- Willoughby, H. E., 1990: Temporal changes of the primary circulation in tropical cyclones. *Journal of the Atmospheric Sciences*, **47** (2), 242–264.
- Willoughby, H. E., 1998: Tropical cyclone eye thermodynamics. *Monthly Weather Review*, **126**, 3053–3067.
- Willoughby, H. E., J. A. Clos, and M. G. Shoreibah, 1982: Concentric eyewalls, secondary wind maxima, and the evolution of the hurricane vortex. *Journal of Atmospheric Sciences*, **39**, 395–411.
- Willoughby, H. E., F. D. Marks, and R. J. Feinberg, 1984: Stationary and moving convective bands in hurricanes. *Journal of Atmospheric Sciences*, **41**, 3189–3211.
- Wilson, K. G., 1979: Problems in physics with many scales of length. *Scientific American*, **241**, 158–179.
- Wurman, J. and J. Winslow, 1998: Intense sub-kilometer-scale boundary layer rolls observed in Hurricane Fran. *Science*, **280** (5363), 555–557.
- Yeung, P. K. and Y. Zhou, 1998: Numerical study of rotating turbulence with external forcing. *Physics of Fluids*, **10**, 2895–2909.
- Zhang, J. A., P. G. Black, J. R. French, and W. M. Drennan, 2008a: First direct measurements of enthalpy flux in the hurricane boundary layer: The CBLAST results. *Geophysical Research Letters*, **35**.
- Zhang, J. A., K. B. Katsaros, P. G. Black, S. Lehner, J. R. French, and W. M. Drennan, 2008b: Effects of roll vortices on turbulent fluxes in the hurricane boundary layer. *Boundary Layer Meteorology*, **128**, 173–189.
- Zhang, X., K.-S. Yeh, T. S. Quirino., S. G. Gopalakrishnan, F. D. Marks, S. B. Goldenberg, and S. Aberson, 2010: HWRFx: Improving hurricane forecasts with high-resolution modeling. *Computing in Science and Engineering*, **13**, 13–21.
- Zipser, E. J., 2003: Some views on “hot towers” after 50 years of tropical field programs and two years of TRMM data. *Meteorological Monographs*, **29** (51), 50–58.

